Western Australian School of Mines:

Minerals, Energy and Chemical Engineering

Pore-scale, Computational Fluid Dynamics-based Simulation of Supercritical CO_2-brine Flow through Porous Media

Farjana Jahan

This thesis is presented for the degree of
Doctor of Philosophy
at
Curtin University

December 2018

Author's Declaration

To the best of my knowledge and belief, this thesis contains no material previously published by any other person except where due acknowledgment has been made.
This thesis contains no material which has been accepted for the award of any other degree or diploma in any university.

Signature: Tanjana

Date: 12.12.2018

Abstract

Carbon capture and storage (CCS) is one of the best modern technologies for reducing atmospheric carbon dioxide (CO_2) concentrations. It works by capturing CO_2 emitted from power plants and various heavy industries and injecting it into deep saline geological reservoirs. Several trapping mechanisms (structural, residual, dissolution and mineral trapping) are applied to trap CO_2 in deep underground formations in order to maintain the effectiveness of long-term storage. Improved fundamental understanding of these processes leads to the optimisation of an efficient and effective CCS system. Generally, CO_2 is injected in a supercritical state (above the critical temperature of about 31.10 °C and critical pressure of about 7.39 MPa) into saline (brine) aquifers (IPCC Special Report, 2005). It is reported in the literature that capillary pressure plays an important role in the distribution of two-phase (brine and supercritical CO_2) fluid distributions within reservoirs used for CCS.

The full-scale characterization of capillary pressure on different heterogeneous sedimentary formations and, moreover, observations of the migration, distribution and trapping of supercritical CO_2 ($scCO_2$) in porous geological formations, appears to be impractical, especially in the context of cost and manpower at all scales. To date, there is hardly any numerical modelling available in the literature that focuses on the prediction of $scCO_2$ capillary pressure within pore spaces. This thesis investigates two-phase (brine and $scCO_2$) flow behaviour, residual saturation, relative permeability, capillary trapping capacity and fluid fractional flow under various drainage and imbibition conditions using pore-scale numerical simulations based on computational fluid dynamics (CFD). These investigations are conducted at the micrometre scale in Ottawa F42 Sand Pack (U.S silica) and Berea sandstone (Ohio, U.S.A.). Also, $scCO_2$ capillary pressure and other petro-physical properties are predicted for Berea sandstone. Some of these parameters (particularly fluid relative permeability and capillary pressure) are investigated for a brine-oil system within the micropores of Ottawa F42 Sand Pack and Berea sandstone as a benchmarking process.

AVIZO image processing software is used to process micro-CT scanned images of the micro-pores of Ottawa F42 Sand Pack and Berea sandstone to compute porosity and surface mesh parameters. ANSYS ICEM CFD, a mesh generation module of ANSYS (commercial CFD software), is used to build a volume mesh from the surface mesh.

ANSYS CFX, another module of ANSYS software, is used to perform numerical simulation on the volume meshes of these samples. Each numerical simulation stage consists of a drainage event simulating the injection of supercritical CO_2 into a completely brine-wetted sample, followed by an imbibition process by injecting brine into brine-scCO$_2$ saturated samples. For the brine-oil system benchmarking process, scCO$_2$ is replaced by oil (n-octane) for the above steps. Analysis of the numerical experiments provides quantitative information about two-phase flow phenomena at the micrometre (pore) scale. Numerically-estimated results are compared with data from existing experimental and numerical studies. The results show a quantitative match to experimental saturation measurements than those obtained by other numerical studies. Moreover, sensitivity studies of other multi-phase flow parameters are conducted to determine the effects of these parameters on CO_2 saturation in the presence of heterogeneity. The estimation of scCO$_2$ capillary pressure within the micropores of rock samples has the potential to greatly advance the study of capillary pressure phenomena in scCO$_2$-brine systems. This work can be extended to investigate brine capillary pressure in supercritical brine systems at micro-pore levels.

Acknowledgements

Table of Contents

List of Figures

Figure 4.4(a-c) showed the distribution of brine and scCO$_2$ in the Ottawa F42 Sand Pack at various simulation times during the drainage process. In these figures, red

List of Tables

List of Variables

u = Fluid velocity, m/s

K = Absolute permeability, Darcy

$\emptyset$ = Porosity

Θ = Contact angle, degree

β = Weibull shape parameter

α = Weibull characteristic life

μ = Viscosity, cP

σ = Surface tension, N/m

ρ = Fluid density, kg/m^3

N_c = Capillary number

P_c = Capillary pressure, Pa

S_w* = Normalized wetting phase (brine) residual saturation

S_w = Wetting phase (brine) saturation at various times

S_{wi}^* = Normalized initial brine saturation

S_{wc} = Connate wetting phase (brine) saturation

K_{rw} = Wetting phase (brine) relative permeability

K_{nrw} K_r^o = Non-wetting phase (supercritical CO_2 or oil) relative permeability at connate brine saturation

$S_{o,F}$* = Normalized free non-wetting phase (supercritical CO_2 or oil) saturation at various times

$S_{o,F}$* = Normalized free saturation at various simulation times

S_{ot}* = Normalized trapped non-wetting phase (supercritical CO_2 or oil) saturation at various simulation times

S_{or}^* = Normalized non-wetting phase (supercritical CO_2 or oil) residual saturation

S_{or}^* = Normalized non-wetting phase (supercritical CO_2 or oil) initial saturation

S_o* = Normalized non-wetting phase (supercritical CO_2 or oil) saturation at various simulation times

$S_{or,max}^*$ = Normalized maximum residual non-wetting phase (supercritical CO_2 or oil) saturation

C = Land trapping coefficient

λ = pore-size distribution factor

K_{nrw} = Non-wetting phase (supercritical CO_2 or oil) relative permeability

1. Chapter 1: Introduction

This chapter describes the motivations for conducting this thesis. First, a brief discussion of global warming and the prevention of environmental pollution (through CCS) is provided in Section 1.1. Then, the properties of supercritical CO_2 ($scCO_2$) and various CO_2 trapping mechanisms are described in Section 1.2. Research gaps and the scope of this thesis are presented in Section 1.3. A literature review of sand pack studies (Ottawa F42 Sand Pack in oil-water/brine and $scCO_2$-water/brine system) is provided in Section 1.4. In Section 1.5, the significance of this research work is provided, while Section 1.6 presents its objectives. Then, a statement of the thesis' workflow and an outline are described in Sections 1.7 and 1.8, respectively.

1.1. Global warming and prevention of environmental pollution

1.1.1. Global warming and greenhouse effect

Global warming is a rise in the average surface temperature of the earth and is causing many environmental challenges. It is one of the most alarming environmental issues that humans are currently facing. This unwanted increase in temperature will result in various undesirable effects, such as increases in ocean acidity and sea level, reductions in agricultural yields and increases in catastrophic incidents (floods, droughts, hurricanes, heatwaves etc.) Moreover, extreme weather conditions will take place along with a hotter and drier atmosphere.

The main cause of the rise in global temperature is believed to be the combustion of fossil fuels for energy production (Voormeij & Simandl, 2004). Burning fossil fuels (coal, oil and gas) releases water vapour, carbon dioxide (CO_2), methane (CH_4) and nitrous oxide (N_2O). Among them, CO_2 is considered to be the most common. Combustion of these gases heats up the temperature of the earth. Moreover, the temperature of our earth rises due to 'the greenhouse effect. This effect can be explained by the radiation delivered by the sun. Solar radiation hits Earth's surface and then is rebounded back toward the atmosphere as heat. Too much consumption of greenhouse gases (such as CO_2) prevents solar radiation from escaping into the open atmosphere by creating a barrier. Thus, the heat is trapped close to the Earth's surface

and troposphere (the lowest layer of the atmosphere) and becomes the principal reason for increases in global temperature.

According to the Paris Agreement (which was approved by 159 nations in summer 2017), the countries responsible for more than 80% of global greenhouse gas emissions showed a greater level of ambition and commitment than ever before to mitigate greenhouse gas emissions. Global warming due to greenhouse gas emissions is recommended to be limited to 1.5 °C according to a recent IPCC report (IPCC, 2018). Meeting such a target becomes the most critical challenging task for scientists, researchers, engineers, environmentalists and policymakers.

1.2. *Prevention of environmental pollution through capturing and storing CO_2*

Today's major environmental pollution is believed to be due to the discharge of CO_2 from different sources. In this regard, CO_2 capture and storage (CCS) can play an important role in reducing the amount of CO_2 gas emitted. CCS is one of the most efficient processes for limiting the emission of harmful CO_2 from different sources (mostly combustion of fossil fuels in factories and industry) and, thus, prevent CO_2 from entering into the atmosphere. This process consists of several steps: CO_2 capture by various configurations of technology, separation of CO_2 out of the air or flue gas, transportation to the storage area and, finally, sequestration in different places (deep saline aquifers, coal beds, and oil and gas reservoirs in the form of mineral carbonates). Among all sources for CCS, deep saline aquifers are the most reliable because they have the largest storage capacity and acceptable levels of environmental risk. Also, these deep saline aquifer projects are widespread in the world (Bennion & Bachu, 2008). Although CCS is beneficial for human life as it reduces CO_2 concentrations in our atmosphere, there are some challenges regarding CCS. These are discussed in the next section. Also, a brief description of Australia's current CCS situation is provided afterwards.

1.2.1. Benefits and challenges in CCS

CCS can create the greatest impact on reducing greenhouse gas emissions due to fuel-driven vehicles and industries. Any efficient CCS resource has the capacity to store CO_2 for many hundreds of years. Thus, CCS can improve the quality of human life and the environment. In addition to this paramount environmental benefit, there are

many remarkable challenges and/or concerns that need to be addressed to successfully and safely deploy CCS projects. One of the main technical challenges is associated with the volume of trapped CO_2 in geological formations, which poses many concerns (Kheshgi, 2012):

1. CCS currently needs up to 30% more coal compared with conventional plants to cover the energy needs of CCS. This extra cost has great environmental effects. For example, emissions of acid rain-causing gases (like nitrogen oxides and sulphur dioxides) can be increased.

2. Possible leakage from underground or undersea reservoirs can make the whole process not only unstable and economically unfeasible but can also make the whole process unsafe and cause potential environmental damage.

3. Scarcity of potential sites is quite common. Furthermore, the cost of building necessary infrastructure may be more time-consuming than expected.

4. The targeted capacity of various CCS sources for storing CO_2 is not enough compared to the volumes of CO_2 being generated.

5. Existing power stations will require updating with new equipment/infrastructure, resulting in increased costs of electricity generation and detrimental effects on the economy.

1.2.2. CCS situation in Australia

There are no large-scale CCS projects operating currently in Australia. However, there are multiple CCS demonstration projects at Australian coal-fired power stations (Global CCS Institute, 2011). The Gorgon gas project in Western Australia will qualify when it is fully operational. It is projected to store 3.4 to 4.0 MTPA (metric tonnes per annum) CO_2. The Latrobe Valley, which is one of the major prospective emission sites, has a considerable CO_2 storage capacity within a few hundred kilometres in Bass Strait. It is expected to start storing CO_2 at a 1.0 to 5.0 MTPA rate by 2020. The CO2CRC Otway Project in southwestern Victoria has injected and stored over 65,000 tonnes of $scCO_2$-rich gas 2 km below the earth's surface in a depleted natural gas reservoir from 2004 to 2009. During the period 2009 to 2018, it has stored about 15,000 tons of CO_2-rich gas. It has the world's largest geo-sequestration research project laboratories (Global CCS Institute).

1.3. Properties of supercritical CO_2 and CO_2 trapping mechanisms

CO_2 at a supercritical state is more useful to store in various underground storages compared to gaseous CO_2. In the next sections, the properties of supercritical CO_2 are discussed in this regard. Moreover, different CO_2 trapping mechanisms are presented in order to have an idea of CO_2 trapping processes.

1.3.1. Properties of supercritical CO_2 ($scCO_2$)

CO_2 acts as a supercritical liquid, termed *supercritical CO_2* ($scCO_2$) when it is in saline aquifers at around 1000-2000 metre depths with pressure and temperature ranges of 10–20 MPa and 40–75 °C, respectively (Nordbotten et al., 2005). Under such conditions, CO_2 acquires less storage volume compared to gaseous CO_2 for a given mass of fluid (Balashov et al., 2013). Also, $scCO_2$ is weakly soluble in brine solution and better option for underground storage (Macminn et al., 2011). The solubility of $scCO_2$ depends on the pressure, temperature and brine composition (Duan et al., 2006; Yang et al., 2008).

1.3.2. CO_2 trapping mechanisms

CCS in deep saline aquifers can be achieved through four trapping mechanisms: structural trapping, dissolution trapping, mineral trapping and capillary trapping. Among these, capillary trapping of CO_2 is believed to be the most effective and efficient because it can trap the highest amount of CO_2 and large-scale, safe, long-term CO_2 storage can be achieved through this process. In the capillary trapping method, capillary forces are involved and CO_2 is displaced by the injection of chase brine or natural groundwater flow. The relative amounts of dissolved and free CO_2 determine the amount of trapped CO_2. Also, the amount of trapped CO_2 is dependent on the characteristics of the formation's geological storage or reservoir rocks (e.g. pore geometry or structure of the pore network), rock and fluid properties (e.g. porosity, and permeability, wettability, contact angle, relative permeability, saturation, initial CO_2 saturation, etc.), as well as injection rate.

To understand the capillary trapping mechanism, it is important to understand the drainage and imbibition processes. The imbibition process is a process through which the CO_2 (non-wetting phase in a water/brine-wet system) is replaced by water/brine

solution (usually wetting phase in a water/brine-wet system). The drainage process is the opposite of the imbibition process. These processes may be natural or forced.

How CO_2 (during drainage processes) first flows through one pore to another through its pore network, and/or passes through the first pore and its throat and then enters a second pore, is a complicated process (Raeini et al., 2014). According to the experimental and analytical study carried out by Roof (1970), the wetting layer thickness changes with increases in the leading interface capillary pressure to achieve a capillary equilibrium in the first pore. At some time, when the leading interface is passing through the second pore, the wetting layer radius of curvature reaches its maximum point. At this maximum point, this curvature radius cannot increase its volume to maintain capillary equilibrium with the frontal meniscus. At the same time, the wetting layer in the throat becomes unstable and eventually makes a bridge between the first and second pore for CO_2. This is called 'snap-off' during the drainage process. The threshold capillary pressure (the difference between the capillary pressure of water/brine and CO_2 in the throat just before the first droplet starts to disengage) for snap-off acts as the minimum capillary pressure that the wetting layer can have in the throat. This threshold pressure depends on the mineralogy of the geological rock sample and the curvature of the pore wall (Blunt, 1998). When CO_2 reaches this threshold pressure, it can start its movement through the water/brine-wet geological sample during the drainage process. Drainage continues until a maximum and stable capillary pressure is reached. At this stage, some water/brine may present in crevices in the pore spaces and also in smaller pores and throats (Blunt, 1998). After the completion of the drainage process, the imbibition process starts. Water/brine invasion during the imbibition process can be explained through three different mechanisms. The first is a piston-like advance mechanism (Blunt, 1998). Practically, it is a complex mechanism (Lenormand et al., 1983; Lenormand & Zarcone, 1984). In this mechanism, water/brine remains in the crevices of the pores with a layer of CO_2 sandwiched in between (when the contact angle is greater than 135°). At the same time, the centre of the pore or throat is filled with water/brine. Snap-off is the second type of mechanisms in the imbibition process. Along with snap-off during imbibition, there is another pore-filling mechanism which is very rare and less favoured than piston-like advancement. This mechanism can be observed when a negative capillary pressure (at contact angles greater than $45°$) has occurred.

As CO_2 dissolves into water/brine (during drainage and imbibition processes), the porous media becomes mutually saturated with CO_2 and water/brine. Moreover, trapped CO_2 (by capillary trapping) remains as disconnected blobs and, over time, it dissolves into nearby water/brine. This situation influenced the contact among water/brine, CO_2 and minerals present in the geological formations. This situation, in turn, increases the chance of mineral trapping, which is the second type of trapping mechanism. In mineral trapping, CO_2 becomes immobilized as carbonate minerals, thus, entrapment of CO_2 increases compared with other CO_2 trapping mechanisms if it continues for a long time, for example, 1000 years (Zhang et al., 2009), warranting that mineral trapping may dominate at the later stages of a long-term CO_2 sequestration project.

The third type of trapping mechanism, structural trapping, dominates at the beginning of the CO_2 injection process. In this trapping mechanism, injected CO_2 moves upward through the porous media until it reaches impermeable cap rock. This cap rock protects trapped CO_2 from leakage. Nevertheless, cap rock has much potential for leakage and can be compromised easily (Wildenschild et al., 2001).

The fourth and last type of trapping mechanism, dissolution trapping, immobilizes the volume of CO_2 in the reservoir through a dissolution process in the formation brine. Thus, this dissolution process ends up in a heavier CO_2-enriched brine phase.

1.4. *Research gaps and scope of the work*

Although four different trapping mechanisms can explain CCS within geological locations, it is a challenging task to quantify the contributions of different mechanisms regarding effective and efficient CO_2 immobilization over a certain time period. Due to the lack of well-characterized laboratory data, CO_2 retention mechanisms are poorly understood and explained. Furthermore, it is expensive and hardly possible to set up and conduct laboratory experiments under reservoir conditions. Traditional laboratory-based experiments are costly and require much time. In this regard, it will be less costly and time-consuming if reservoir conditions can be replicated through pore-scale numerical experiments. So, researchers can upscale modelling data to reservoir-level data. Due to advancements in high-performance computing (HPC), nowadays, it is quite easy and technically possible to perform pore-scale numerical simulations to understand the pore-scale physics behind CO_2 trapping.

Pore-scale numerical modelling and simulation is an emerging numerical technique for studying the multiphase flow through porous geological systems. This modern technique gives researchers an advanced understanding of multiphase fluid flow behaviour, the various macroscopic properties which are governing factors for multiphase flow, and pore-scale fluid displacement processes through complex pore geometry. In this regard, this thesis has developed a numerical model to understand the various factors involved in CO_2 sequestration. Before going further, some discussion about previous work will be helpful for understanding the scope of this research. In the next section, a detailed literature review is provided.

1.5. Literature review

In order to investigate CO_2 mitigation and immobilization processes within pore spaces in geological samples, a number of studies have been performed regarding multi-phase relative permeability (Spiteri et al., 2008; Bennion & Bachu, 2008; Akbarabadi & Piri, 2013), capillary pressure (Plug & Bruining, 2007; Akbarabadi & Piri, 2013). However, there are limited experimental and numerical studies regarding oil-brine or oil-water flows through various sand packs. In Section 1.5.1, some information on these studies (oil-brine or oil-water flow through sand packs) is presented. If the availability of studies regarding $scCO_2$-brine systems for sand packs is compared with that of oil-brine systems, then it appears that there are very few studies on $scCO_2$-brine systems for sand packs. Section 1.4.2 covers previous literature regarding $scCO_2$-brine systems for sand packs.

1.5.1. Literature review for oil-water/brine systems in sand packs

Abeci et al. (1992) measured two-phase (tap water-air, de-aired water and nitrogen) relative permeability for unconsolidated sands (fine sand, heterogeneous sands and coarse sands) by using steady-state techniques. This work provided data for modelling studies. Bartley and Ruth (2001) studied the effects of media permeability, oil viscosity and pressure drop on oil and water relative permeability. All of these factors were estimated by the Johnson, Bossler and Naumann (JBN) method for vertically-oriented sand packs. Estimated results showed that the permeability of the porous sand packs dominated oil and relative permeability. The effect of the other two factors was found to be significant over specific saturation values, especially for water relative permeability. Bravo et al. (2007) analysed the unconventional behaviour of oil relative

permeability during depletion tests of gas-saturated heavy oils for the Ottawa sand pack. They discussed the effect of the capillary number on the transport parameters responsible for generalized flow equations. Gittins et al. (2010) measured the residual oil saturation in six unconsolidated sands (HST 95, F110, OMR, F-42, F-35, LV-60) through numerical simulation using the maximum ball algorithm method. The residual saturation ranged from 10.8–13.1%. Al Mansoori et al. (2009) quantified the impact of the initial non-wetting phase and porosity on the residual non-wetting phase saturation for sand packs and consolidated rocks and proposed models to correlate trapping capacity and residual saturation with porosity and initial saturation. The principal application of their work was for CCS. Iglauer et al. (2012) examined the time dependence of the gravity drainage process of brine through water for the Ottawa F42 Sand Pack, and observed that the water saturation at any particular location is dependent on time. Also, Iglauer et al. (2013) performed a combination of laboratory experiments and numerical simulations to investigate the influence of a tidally-induced, semi-diurnal change in water table depth on the distribution of water saturation in the capillary transition zone for the Ottawa F42 Sand Pack. Pentland et al. (2010) performed laboratory-based experiments to investigate the influence of petro-physical properties in oil-brine systems for five sandstone and six unconsolidated sand samples. Mainly, they conducted core flood experiments to measure trapping in unconsolidated sands for oil-brine and gas-brine systems. Raeini et al. (2014) reported a numerical investigation of the F42C Sand Pack and Berea sandstone for a brine-oil system with different capillary numbers to study the mechanisms controlling pore-scale two-phase flow. In their work, a new concept—to upscale the sub-pore-scale forces—was developed and the relation between the flow and pore-scale pressure drops was studied. Ruspini et al. (2017) presented a pore-network model of the LV60A sand pack to estimate capillary trapping in the water-wet media. The effects of average aspect ratio on the sand pack trapping curve were examined in their work.

1.5.2. Literature review on scCO$_2$-water/brine systems in sand packs

Talabi et al. (2008) performed pore-scale simulations of two sand packs (F42 A and LV60A) to predict absolute permeability, resistivity and Nuclear Magnetic Resonance (NMR) response. They obtained results that overestimated the magnetization decay in NMR experiments. Tokunaga et al. (2013) developed a high-pressure controller to

perform capillary pressure and saturation laboratory experiments on moderately well-rounded quartz sand for a scCO$_2$-brine system. Results showed that wettability alternation by scCO$_2$ made hydraulic behaviour more challenging. Das and Mizaei (2013) conducted experiments and numerical simulations to investigate dynamic effects in capillary pressure relationships for two-phase flow in sands. The dynamic coefficient was found to be a nonlinear function of saturation, which was dependent on sand permeability. Moreover, Mizaei and Das (2013) completed experiments to study hysteretic dynamic effects in a capillary pressure-saturation relationship for two-phase flow in different types of sands (homogeneous and layered). The results revealed that this unique relationship is hysteretic in nature and the magnitude of the dynamic coefficient is commonly higher for the imbibition process (for a particular water saturation). Das et al. (2014) conducted numerical simulations to study the dynamic capillary pressure effect on scCO$_2$-water flow and the dynamic coefficient of scCO$_2$ flow in sands (coarse sand, fine sand, and a mixture of the two). They extended their previous works to scCO$_2$ conditions. After analysis of results, they established an inverse relationship between saturation and the dynamic coefficient and concluded that, as saturation decreases, the time taken to attain capillary equilibrium for a CO$_2$-water system increases. Khudaida and Das (2014) determined CO$_2$ gas saturation at various timescales, pressures and temperatures. Various numerical simulations were performed to illustrate the changes in saturation, capillary pressure and the amount of dissolved CO$_2$ due to changes in the injection process, geothermal gradient and hydrostatic pressure. It was clear from the numerical results that there is a proportional relationship between injection pressure and capillary forces. Jung and Hu (2016) conducted experiments for Otway 40/60 sand to quantify the impacts of pressure and brine salinity on capillary pressure-water saturation in a CO$_2$-brine CCS system. Their results showed that variations in contact angle and interfacial tension dominated the influence of CO$_2$ pressure and brine salinity on capillary pressure-water saturation in CCSs.

1.6. *Significance of the proposed research*

Generally, hydrocarbons within the pore-spaces of geological media are displaced with water/brine in order to produce gas and oil. During the process of CCS, the target is to trap more gas within the reservoir or saline aquifer. This process requires an adequate understanding of the governing factors in the fields of energy and the environment.

Also, such understanding is essentially very critical to accurately determine the petro-physical and other key flow and displacement properties which are essential to evaluating the performance of CCS projects.

The injection of $scCO_2$ into a brine aquifer develops two-phase flow behaviour, which can be further influenced by various factors such as pore space geometry and the flow characteristics of porous media (e.g. permeability, relative permeability, capillary pressure, etc.). Although conventional core-scale experiments are used to measure constitutive relations such as relative permeability, wettability and other properties, they are very time-consuming and expensive. The accuracy and quality of these experiment-driven properties are dependent on the types of set-up, conditions and assumptions considered in a particular laboratory's conditions and, consequently, can create huge uncertainties in the measurements. Also, the quantification of these uncertainties is often very difficult. Considering all these challenges, pore-scale numerical simulation approaches have become very attractive tools, not only to determine capillary pressure and other petro-physical factors within pore spaces of reservoir samples but also to improve the fundamental understanding of fluid flow through porous geological media which have very complex architectures. No real-world apparatus is required in numerical modelling, and it is faster than laboratory experiments. In addition, it can perform numerical experiments that are difficult to repeat under different boundary conditions in the laboratory. Consequently, this technique can supplement the need for conventional and special core analyses (CCA and SCAL), which are used for the measurement of petro-physical properties by providing single- and two-phase flow functions for a range of rock and pore types (Kalam, 2012).

1.7. *Objectives of this study*

According to the Intergovernmental Panel on Climate Change (IPCC), CCS is the most reliable and mature remission strategy for the geological storage of CO_2. Different countries in the world are utilizing CCS to reduce global warming and corresponding adverse climatic changes. For instance, the Otway Project in Victoria, Australia (commenced in April 2008), has been administering about 4500 tonnes of CO_2 per month into a depleted gas reservoir about two kilometres below the surface (Parliament of Australia, 2018). If CCS is executed at large scales (for instance, a 100-fold increase over the amount currently sequestered annually in the Otway project), then a sound

scientific knowledge of the long-term fate of CO_2 trapped underground is required. This knowledge consists of various consecutive steps for the characterization, selection and monitoring of technologies, engineering applications, expenses and performance optimization, appropriate process safety operations (including health and environmental issues) and corresponding research approaches in order to manage long-term liability, both at the industry and institutional levels.

As different sources, such as saline aquifers, oil reservoirs, gas reservoirs are used for CO_2 trapping, fundamental knowledge of multi-phase flow and, especially, entrapment of CO_2 in $scCO_2$-brine systems is essential to utilize the advantages of CCS. In this regard, some questions may be raised, such as: What fraction of pore space of geological samples will be filled up with CO_2? What will be the spatial distribution of trapped CO_2 within pore spaces? What will be the amount of trapped and free CO_2 within pore spaces? What petro-physical and other properties are influencing the fluid flow rate and distribution within pore zones? To what extent is capillary trapping reliable and permanent? What will be the most accurate assessment of CO_2 storage in terms of economic evaluation? Numerical modelling and simulations can be very helpful means of improving our ability to answer these questions since numerical modelling simulations require less time and money than traditional laboratory based experiments. In the process of the advancement of numerical research, different approaches can be applied in view of reliable performance assessment, even at the pore-scale level.

In this thesis, a numerical approach was used for the investigation and analysis of two-phase fluid flow at the pore-scale by use of X-ray micro-computed tomography (micro-CT)-generated images of the micro-pores of reservoir rock samples (Ottawa F42 Sand Pack, Berea sandstone and Benthemer sandstone). This numerical analysis is expected to establish a valid basis for answering some of the questions posed earlier in the previous paragraph. The current study primarily focuses on the issues and challenges related to $scCO_2$ capillary pressure in three deep porous geological formations (Ottawa F42 Sand Pack, Berea sandstone, and Bentheimer sandstone) which may be considered for CCS projects. Research regarding the factors determining the amount of trapped CO_2 in $scCO_2$-brine systems is still limited for these rocks. The key objectives of this thesis are summarized below:

1. Pore-scale numerical simulation to aid the understanding of two-phase ($scCO_2$-brine) flow behaviour through geological porous media using computational fluid dynamics (CFD)-based numerical simulation.

2. Numerical simulation of the $scCO_2$-brine distribution within pore spaces of the sand pack for a better understanding of $scCO_2$-brine flow behaviour with an emphasis on investigation of the trapping efficiency of $scCO_2$ in porous geological systems.

3. Prediction of rock and fluid properties such as relative permeability, capillary pressure, and wettability using numerical simulation, and identification of factors influencing the performance of CO_2 sequestration.

These aspects are investigated in the Ottawa F42 Sand Pack and in Berea and Bentheimer sandstones.

1.8. Statement of workflow

In order to achieve the above objectives, a numerical model is built up from X-ray computed tomography (micro-CT) images of the micro-pores of the Ottawa F42 Sand Pack. In this regard, a numerical methodology is comprehensively discussed to describe the details of multiphase flow through the pore network of a few millimetres of the Ottawa F42 Sand Pack. This microscopic sand pack sample typically consists of several thousand pores and pore-throats. A commercial image processing tool (AVIZO) is used for the visualizing and processing of images and the construction of a 3-dimensional numerical model (surface mesh). In this work, ANSYS, a widely used and reliable CFD software, is used to create volume meshes. ANSYS ICEM-CFD, a special module of ANSYS, is utilized to create the volume mesh of the Ottawa F42 Sand Pack from the surface mesh. ANSYS CFX is used for the simulation of $scCO_2$-brine flow within the pore-spaces of the Ottawa F42 Sand Pack rock. For this thesis, ANSYS CFX solves the momentum, pressure-based continuity and volume fraction equations following the Eulerian-Eulerian multiphase model. It is a popular and widely used technique for tackling simulation problems where two or more fluid phases are separated by a distinct interface, which is of great interest (ANSYS CFX-Solver Modelling Guide, 2009). To calculate the pressure gradient at the interface between brine and $scCO_2$ and for interphase momentum transfer, the Free Surface Flow model is used in ANSYS CFX. The numerical model is described and discussed in Chapter 3. In this model, the surface tension force is considered as a volume force concentrated

at the interface. To describe the surface tension force, the continuum surface force model proposed by Brackbill et al. (1992) is introduced in the Free Surface Flow model. After the completion of the simulation process, the results files generated are used to visualize and process the results using the ANSYS CFD-post-processing module.

After the creation of the numerical model for the Ottawa F42 Sand Pack, it is tested for validation (benchmarking). In this process, an oil-brine system is considered and the necessary boundary conditions are applied for a set of simulations (for drainage and imbibition cycles). After completion of the simulations of the drainage and imbibition cycles, fluid (oil and brine) saturation are estimated. The estimated saturation data are then used to estimate relative fluid permeability and oil capillary pressure at various conditions. Various empirical correlations are used to predict these parameters. After the completion of these analysis steps, the predicted numerical results are validated with other numerical and experimental works. Upon validation, different cases are simulated to achieve the thesis objectives as stated above. In addition to Ottawa F42 Sand Pack, Berea and Bernheimer sandstone samples are modelled and analysed.

This research work also attempted to create a method of acquiring, estimating and analysing numerically-generated data to predict rock and fluid properties, with the objective of complementing traditional laboratory-based experiments. Furthermore, variations in different properties, due to wettability trends and different pore structures, are expected to be predicted reliably using such numerical techniques.

1.9. Organization of the thesis

The organization of this thesis is described below.

In Chapter 2, a literature review of the current state of network modelling, with special emphasis on various parameters such as capillary pressure, relative permeability, residual saturation $scCO_2$-brine fluid distribution, capillary trapping capacity and fractional flow are presented. Moreover, a review on the volume of fluid (VOF) method, and other previous experimental and numerical works on the Berea sandstone, are briefly explained.

In Chapter 3, the detailed mathematical model and assumptions, which are the foundations of the simulation process, are comprehensively described.

In Chapter 4, a comprehensive description of the numerical simulation of $scCO_2$-brine fluid distribution within pore spaces of the Ottawa F42 Sand Pack, along with model validation, prediction of fluid residual saturation, $scCO_2$ capillary pressure, and fluid relative permeability, is made.

In Chapter 5, a detailed description of the numerical simulation of $scCO_2$-brine fluid distribution within the pore spaces of Berea sandstone is made, along with a comprehensive discussion of model validation, prediction of fluid residual saturation, $scCO_2$ capillary pressure, and fluid relative permeability.

In Chapter 6, the numerical simulation of $scCO_2$-brine fluid distribution within pore spaces of Bernheimer sandstone, including prediction and analyses of capillary trapping capacity and other sensitivity studies of Ottawa F42 Sand Pack and Berea sandstone, is discussed.

The summary, conclusions and recommendations for further research/consideration are discussed in Chapter 7.

The following articles were presented at Society of Petroleum Engineers (SPE) conferences and published in SPE and were based on the material presented in this thesis.

•Jahan, F., Ahmed, S., Hossain, M., & Iglauer, S. (2016, October). Numerical Modelling for the Prediction of Residual CO_2 Trapping in Water-Wet Geological Porous Media. In SPE Asia Pacific Oil & Gas Conference and Exhibition. Society of Petroleum Engineers. (SPE-182240-MS).

• Jahan, F., Hossain, M. M., Ahmed, S., & Iglauer, S. (2017, April). Investigating Impact of Various Properties on Relative Permeability and Non-Wetting Phase Fractional Flow in Brine/Oil System in Water-Wet Reservoir Rock by Numerical Simulation. In SPE Western Regional Meeting. Society of Petroleum Engineers. (SPE-185744-MS).

• Jahan, F., Hossain, M., Ahmed, S., Iglauer, S. (2017, December). Review of the Influence of Digital Rock Physics on Enhanced Oil Recovery (EOR) For Berea

Sandstone in Brine/Oil System by Numerical Simulation. One Curtin International Postgraduate Conference, Miri, Sarawak, Malaysia.

• Jahan, F., Ahmed, S., & Hossain, M. (2018, October). Investigating the Influence of Wettability and Direction on Supercritical CO_2 Trapping for Supercritical CO_2-Brine Imbibition Process at Pore Scale for Bentheimer Sandstone. In SPE Asia Pacific Oil and Gas Conference and Exhibition. Society of Petroleum Engineers. (SPE-192105-MS).

2. Chapter 2: Literature review

In this chapter, fundamental and concise descriptions of previous work on two-phase flow through porous media are provided. The intention of this discussion is to provide the background necessary to follow the relevant explanations in this thesis. Previous laboratory-based experimental works, especially for Berea sandstone, are discussed in Section 2.1. Section 2.2 elaborates the discussion on previous numerical simulation works associated with $scCO_2$-brine within the pore spaces of the Berea sandstone. Some important parameters relevant to this thesis also discussed in Sections 2.3-2.4.

2.1. *Literature review on laboratory-based works*

This section reviews previous laboratory-based experimental works associated with $scCO_2$-brine flow, relative permeability and capillary pressure, and capillary trapping in CO_2 storage.

2.1.1. Laboratory-based experimental works for the prediction of relative permeability and capillary pressure

Saeedi et al. (2011) conducted experimental studies to investigate the effects of cyclic core-flooding patterns under in situ reservoir conditions of pressure and temperature on multiphase flow characteristics for various sandstones with different porosities and permeabilities. Their results showed that cyclic CO_2-brine had minimal influence on fluid saturation profiles but a maximum effect on differential pressure within the pore spaces. Moreover, their study pointed out that interfacial tension has a strong influence on the process of brine displacement by CO_2. Perrin et al. (2009) performed steady-state relative permeability experiments for different injection flow rates on a sample from the CO2CRC-Otway project and Berea sandstone for a CO_2-brine system. They observed that different flow rates gave different fluid saturation and relative permeability values. The fluid saturation values from numerical simulation were consistent with laboratory-based results. Al-Menhali et al. (2015) conducted core flooding experiments to investigate the impacts of pressure, temperature and brine salinity on drainage capillary pressure for CO_2-brine systems in Berea sandstone. They also observed steady-state drainage and imbibition-relative permeability results and found no difference between drainage steady-state and unsteady-state relative permeability curves. However, imbibition-relative permeability curves showed hysteresis effects. Pini et al. (2013) measured capillary pressure and relative

permeability curves from core flooding experiments on Berea sandstone for three different fluid pairs (gaseous CO_2/water, gaseous N_2/water and supercritical CO_2/brine). The three different fluid pairs showed the same trends in drainage-relative permeability curves. Anderson (1986) observed that the drainage capillary pressure is insensitive to wettability when the contact angle is less than 50° for a uniformly wetted porous medium. Moreover, he demonstrated that the rate and amount of spontaneous imbibition are dependent on wettability, viscosity, pore structure and surface tension. He also stated that the shape of the capillary pressure curve will not represent the reservoir if the reservoir is oil-wet or intermediate-wet. Andrew et al. (2014) presented a new method to investigate and analyse the formation, displacement and remobilization of a residual phase at the pore scale, and at reservoir pressures and temperatures. Also, they proposed a new formulation of the Bond number. They found that capillary pressure is a strong function of local pore topography, and most ganglia fulfil the remobilization process at a capillary number of around 1. Krause et al. (2011) conducted core flood experiments and numerical simulations (using TOUGH2-MP) to study $scCO_2$-brine flow distribution and behaviour under different conditions and flow regimes. Moreover, they extended the work of previous authors to develop a new method to predict permeability at the sub-core scale from saturation and capillary pressure data. Müller (2011) reviewed two steady-state and unsteady-state relative permeability studies for sandstones and carbonates at various temperatures, pressures and salinities. In most cases, CO_2 behaved as a non-wetting phase. Busch et al. (2011) provided a comparative study regarding relative permeability and capillary pressure to show the importance of accurate laboratory-based techniques for commercial application of CO_2 capture and storage systems (CCSs). Soroush et al. (2013) conducted laboratory-based experiments and numerical simulations to investigate the effects of flooding flow rates in CO_2-brine systems. They observed that residual CO_2 trapping is sensitive to the imbibition rate. They also developed correlations and utilized them to predict CO_2 residual values in different aquifer influxes. Niu et al. (2015) conducted laboratory experiments and numerical simulations (using the CMG simulator) on various andstones (including Berea sandstone) to obtain residual trapping values for CO_2-brine systems. They observed that the residual trapping characteristic curve is unalterable across a wide range of pressures, temperatures and brine salinities. Their system was strongly water-wet and they concluded that exact reservoir conditions could not be replicated in the laboratory. Krause et al. (2013)

presented a new method (based on their previous work in 2011) to calculate sub-core-scale relative permeability. By using this procedure, they conducted highly refined numerical simulations of core-flooding experiments without using the typical assumptions. They observed that the two independently-predicted relative permeability values were within the limits of experimental measurement errors. They revealed that their work on CO_2-brine/water systems could be extended to any multiphase system where the fine-scale fluid distribution is capillary-dominated. Levine et al. (2013) conducted core-flood experiments to predict relative permeability in the Berea sandstone. Their results showed that the values of endpoint drainage CO_2 relative permeability (for liquid CO_2 and $scCO_2$) are clustered around 0.40. Perrin et al. (2011) described the formation of dissolved CO_2 in the Berea sandstone as the pressure was reduced from reservoir conditions (1800 psi) through laboratory experiments. They observed a leakage at one end of the core holder during the experiment, which resulted in complex multiphase flow behaviour. Also, a sharp vertical front developed between the CO_2-rich and CO_2-poor regions of the core. They proposed further numerical simulation to explain these observations properly.

2.1.2. Laboratory-based experimental works on capillary trapping

The capillary trapping capacity of reservoir rocks is dependent on various factors, such as porosity, geometry of pore structure, pore throat aspect ratio, pore size distribution, imbibition process and non-wetting phase displacement extent (Tokunaga et al. 2013).

Niu et al. (2015) observed CO_2 residual trapping in the Berea sandstone through core flooding experiments under reservoir conditions. They found that the trapping efficiencies are similar at different pressures, temperatures and salinities. Pentland et al. (2011) performed core-flood experiments at reservoir conditions to determine the capillary trapping curve (by the porous plate method) and contact angles for the CO_2-brine system in the Berea sandstone. The measured residual saturation (37%) to be lower than that of an oil-brine system in a similar core (48%). Pentland et al. (2011) measured primary drainage capillary pressure for a $scCO_2$-brine system in Berea sandstone (by the porous plate method). A decrease in the quantity of capillary trapping was observed when compared with an oil-brine system. However, the dimensionless capillary pressure was the same for $scCO_2$-brine, n-decane-brine and Hg-air systems. Ruspini et al. (2017) stated that capillary trapping of $scCO_2$ is very important as it is used to determine the efficiency of long-term CCS and hydrocarbon

recovery processes. Moreover, capillary trapping influences the hysteresis of capillary pressure and relative permeability. Krevor et al. (2015) studied capillary trapping at laboratory-scale and field-scale for the Berea sandstone. They observed that the impact of heterogeneity on capillary immobilization and capillary trapping in mixed-wet systems are two acute sources of uncertainty. Suekane et al. (2008) performed a pore-scale experimental study of capillary trapping in the Berea sandstone. They estimated the statistical distribution of trapped gas volumes and the effect of capillary number on the stability of trapped gas bubbles. They found that the residual gas saturation fluctuated with porosity along the flow direction.

2.2. Literature review on numerical modelling

In Section 2.2.1, a brief history of developments in numerical modelling is presented. Then, Section 2.2.2 provides a literature review on relative permeability, focusing on numerical simulation-based works. Some previous numerical works associated with the estimation of relative permeability and capillary pressure are also discussed in this section. Section 2.2.3 provides a brief description of capillary pressure and capillary trapping capacity.

2.2.1. History of numerical modelling associated with pore-scale simulation

Numerical modelling of the pore spaces of the geological samples was founded by Fatt (1956) in the middle of the 1950s. Fatt (1956) predicted capillary pressure curves from network models which were actually based on bundles of tubes, thus representing real porous media. Pore size distributions were derived from these curves. Moreover, he computed relative permeability and used different types of lattices of numerical networks (honeycomb, triangular, square and double-hexagonal) to investigate the variability of results due to different networks. He found that his results were close to experimental results. He computed flow properties by using equivalent electrical resistors because, during his time, numerical solutions to flow equations were impossible.

During the 1970s, when computational resources became more available to researchers, further development in the field of computational networking was observed. Chatzis and Dullien (1977) advanced the work of Fatt. They investigated some properties (the breakthrough conditions which will occur in the step-by-step

invasion of a non-wetting phase into an empty 2D or 3D network to test the accessibility of pores and the pseudo-dead-end pore fractions) on 2D and 3D network models which consisted of capillary tubes. These tubes were generalized for any pore size distribution. They established generalized saturation plots for pore accessibility and pseudo-dead-end pore fractions. The accessibility of pores was investigated by using the experimentally-known mercury porosimetry capillary pressure curves of two sandstone samples of known "complete" pore size distribution. The accessibility of pores predicted through 2D and 3D network models of randomly distributed capillary tubes did not match quantitatively with the corresponding experiments. However, quite good simulations of the experimental capillary pressure curve and the accessibility of pores were obtained in the case of 3D networks. In this regard, an assumption was made—that the volume of a capillary segment is proportional to its entry diameter.

Among all numerical methods, pore-network models (PNMs) were the pioneer methods developed to solve challenges in multiphase flow modelling at the pore scale. In these methods, the empty spaces of a geological sample are represented by a lattice of pores and throats, then flows are simplified by assuming certain distinctive flow patterns which are flow regime-dependent. In PNM, for example, Darcy's law emerges from averaging the relevant pore-scale physics and the relevant transport equations are not solved directly in the pore space. So, the approaches related to understanding the flow and transport in porous media became quite different from other methods (Blunt et al., 2002). For pore-network numerical models, three different experimental techniques are outlined: pore space-direct imaging, gas adsorption, and mercury intrusion porosimetry (Blunt, 2001; Blunt et al., 2002, 2013). These models can deliver cost-effective and accurate numerical predictions (Meakin et al., 2009). However, a lot of detail is lost in these methods due to the simplification of geometry.

With the advent of high-performance computing, direct numerical simulation methods were introduced with lower levels of uncertainty than that those of pore network models. In these methods, Navier-Stokes equations are numerically solved. With the help of these methods, numerical experiments can be easily performed that provide data that is quite impossible to obtain through traditional laboratory studies. Moreover, the physics of fluid dynamics can be understood in a more suitable way. Several direct numerical simulation approaches are used to solve pore-scale multiphase flow

problems. Among them, the Lattice-Boltzmann method (LBM), smooth particle hydrodynamics (SPH) and Eulerian methods, as described by Meakin et al. (2009), are prominent. Succi et al. (1989) described LBM as a particle-based technique, which is easily applied to multiphase flow simulations and parallel computing techniques. In this method, the motion of fluids is described in terms of the movement and collision of particles, and an implicit pressure equation is not solved. SPH is a mesh-free LaGrangian method where resolution can be easily adjusted with respect to any variable. It works by dividing the fluid into a set of discrete elements (particles). Holmes et al. (2016) described a numerical scheme for oil reservoirs using the SPH method. Also, Violeau et al. (2016) predicted free surface flows in terms of SPH. Arrufat et al. (2014) predicted relative permeability through traditional Eulerian grid-based methods, which solved the Navier-Stokes equations with good numerical efficiency. In these methods, larger viscosity ratios of the two fluids are handled along with surface tension and interphase tracking.

Blunt (1997) presented a 3D pore-network model to compute relative permeability and capillary pressure for drainage and imbibition processes. They also studied different types of cooperative filling and the effects of flow in wetting layers. Blunt et al. (2001) predicted the possibility of pore-scale modelling to describe impacts on the characterization of various multiphase flow properties. According to his study, in the early 1990s, interest in pore-scale modelling rocketed due to interest from oil and gas companies. After that, pore-scale modelling was used in various fields of engineering and science, including medical applications and other environment-related operations. Riepe et al. (2011) explained the role of micro-CT images on fluid flow visualization, numerous estimation approaches and fluid recovery. Blunt et al. (2002) provided various approaches to describe the pore space, such as examples, pore-network modelling of different physical processes, description of their significance on reservoir characterization, and ways to extend the model to three-phase flow (water, oil, and gas or air). Blunt et al. (2013) explained different numerical techniques for single- and multi-phase pore-scale flows in different rock formations in order to maximise fluid (oil or gas) recovery and optimize carbon dioxide storage. Raeini et al. (2012) discussed the challenges related to the modelling of multiphase flows in porous rocks (for example, modelling multiphase flow at low capillary numbers or explanation of contact line motion). Moreover, they added a dynamic pressure term in the mass and

momentum balance equation (dynamic pressure = total fluid pressure - microscopic capillary pressure) and solved it by using a volume-of-fluid-based finite-volume framework to simulate primary drainage followed by water injection. Also, the problem of spurious currents was solved by developing a new sharp interface formulation. Raeini et al. (2014) investigated the effect of capillary number on fluid relative permeability curves and up-scaled the results to the Darcy scale. Furthermore, Raeini et al. (2014) used a new volume of fluid (VOF)-based finite volume method to model two-phase flow at the pore scale. They used the numerical model to study the mechanisms controlling two-phase flow, layer flow and snap-off. They investigated the effects of geometry and flow rate on trapping and immobilization of disconnected ganglia. Moreover, they presented a force-balance concept to connect flow rates to pore-scale forces and introduced a new variable (capillary field) to characterize the capillary forces under dynamic conditions. Andrew et al. (2014) showed that residual trapping can be used to entrap CO_2 for different rock types though pore-scale experiments. Their work can be extended to multiphase phase flows at subsurface conditions in different geological systems for CCS. Raeini et al. (2015) studied the effects of initial non-wetting-phase saturation, capillary number and flow direction on residual saturation via micro-CT images of Berea sandstone and a sand pack, using pore-scale simulation.

2.2.2. Literature review on numerical simulation of relative permeability

A literature review of numerical simulation works focusing on fluid relative permeability is presented in this section. A brief discussion of the current research motivation associated with fluid relative permeability is provided in Section 2.2.2.1.

2.2.2.1. Relative permeability and research motivation

Relative permeability represents the fraction of the permeability of a porous medium corresponding to each phase in a two-phase ($scCO_2$-brine) flow system. The assessment of fluid relative permeability is one of the continuing major engineering challenges for CCS projects within subsurface storage formations. Carroll et al. (2014) analysed the stability and security of porous geological sources for effective capture of CO_2. They observed that relative permeability is essential, because it not only affects the $scCO_2$ injection rate but also may affect the $scCO_2$ flow and displacement mechanism in the porous medium This, in turn, can cause containment issues.

Similarly, capillary pressure influences CO_2 migration, residual CO_2 trapping and CO_2 dissolution in reservoir brines. Thus, capillary pressure needs to be estimated accurately to determine brine displacement in reservoir rocks and, hence, the onset of viscous flow or leakage to the surface. However, there was not much relative permeability experimental data available in the literature until the early 2000s despite the importance of relative permeability. During this time period, CO_2 emissions and the prevention of CO_2 emissions through CCS became an important worldwide climate issue and researchers started experimental and numerical works to predict the relative permeability of $scCO_2$-brine systems. Accurate data is required by industry to obtain estimates of relative permeability. It is economic for industry to run numerical simulation at the site screening and selection stage before the commencement of a costly and time-consuming site characterization program. A brief discussion about pore-scale numerical works related to these two parameters is made in the next sections.

2.2.2.2. Literature review on numerical simulation of relative permeability

According to Bachu (2013), three experimental programs were conducted to determine relative permeability (from 0.1 mD to 500 mD) of various sandstone and carbonate storage aquifers under in situ conditions in western Canada from 2008 to 2011. Analysis of this study revealed that there is no difference between steady-state and unsteady-state measurement methods and no link between rock porosity and relative permeability characteristics. Moreover, the relative permeability characteristics of CO_2/brine systems are highly area-specific, depending mostly on rock structure and wettability, and cannot be forecasted based on any other rock characteristics (for example porosity, absolute permeability) for numerical modelling, upscaling and history matching of observed CO_2 plume behaviour. Shi et al. (2011) determined CO_2 residual saturation and showed a better understanding of CO_2 trapping mechanism in aquifers. Core flooding tests (for $scCO_2$ systems) on Tako and Berea sandstones were carried out by them. Ramstad et al. (2012) studied relative permeability through the LB method on Berea and Bentheimer sandstones. They found that unsteady-state non-wetting phase drainage relative permeability is over-estimated compared to steady-state data. Juanes et al. (2006) used the Eclipse 100 reservoir simulator to predict the impact of relative permeability and CO_2 trapping in a saline aquifer. They observed the effects of injection rate, alternating water injection, bottom-hole pressure and grid

refinement on the overall performance of the CCS project. Jackson et al. (2005) used a pore-scale network model of Berea sandstone with conventional reservoir-scale simulations to predict wettability variations in the oil-water transition zone. They predicted that an abnormal amount of dry oil may be produced from the transition zone if the initial water saturation is modified by the movement of the free water level (FWL). Furthermore, wettability alternation within the transition zone can affect the long-term water-flood production behaviour of a reservoir. Spiteri et al. (2008) investigated the hysteresis of hydrocarbon phase relative permeability in a two-phase system. They proposed a new model for trapping and water-flood relative permeability to study the dependence of these two parameters on wettability and initial water saturation. This model was validated by pore-network simulation of drainage and imbibition processes. They observed that the convex nature of the water-flood relative permeability curve for oil-wet media is caused by the layer flow of oil. Zaretskiy et al. (2010) presented a direct pore-scale finite element (FE)-based numerical model for single-phase flow. They found that the FE model yielded the same permeability results as the LB method. Blunt et al. (1992) used a 3D network model to estimate relative permeability and capillary pressure in drainage and imbibition cycles. They described two realistic trapping mechanisms and verified percolation theory results for the effect of buoyancy forces on trapped saturation through simulation. Also, they derived an expression for correlation length for displacements which are unsettled by viscous forces. Blunt et al. (2002) presented a conceptual workflow to model two-phase and three-phase flow in geological rock samples. They predicted relative permeability through the framework. They indicated that pore-scale numerical models can be used as powerful reservoir characterization tools in future. Krause et al. (2013) conducted numerical experiments through the finite difference simulator TOUGH2-MP to study multiphase flow behaviour. Their objective was to validate the numerical method on highly heterogeneous cores. However, their work resulted in some limitations. For instance, they ignored the effect of imposing residual liquid saturation in the simulations, which may be a subject for future work.

2.2.3. Literature review on the numerical simulation of capillary pressure and capillary trapping capacity

A comprehensive literature review on capillary pressure and capillary trapping capacity, including the motivation of current studies, is provided in this section.

2.2.3.1. Capillary pressure, capillary trapping capacity and current research motivation

When pores/pore throats in a porous medium are occupied by two immiscible fluids, a pressure difference exists at the fluid-fluid interface due to surface tension. This difference in the phase pressures is termed the *capillary pressure*. In other words, the capillary pressure is the difference between the non-wetting fluid pressure (P_{nw}) and the wetting fluid pressure (P_w) across the interface. It is the function of the wetting phase saturation (S_w). The relationship between capillary pressure and saturation is called the *capillary pressure curve* and can be mathematically expressed by Equation 2.1.

$$P_c(S_w) = P_{nw} - P_w \qquad\qquad 2.1$$

The capillary trapping capacity is the product of reservoir rock porosity and non-wetting phase residual saturation (Zhou et al. 2011) and can be mathematically expressed as per Equation 2.2.

$$C_{trap} = \emptyset S_{nr} \qquad\qquad 2.2$$

Where C_{trap} is the capillary trapping capacity, ϕ is the rock porosity and S_{nr} is the non-wetting phase saturation. The capillary pressure-saturation relationship of a $scCO_2$-brine system within reservoir rock is of major practical importance in a CCS project. With the help of this unique relationship, the movement and safe storage of injected and trapped CO_2 in subsurface reservoirs can be understood better. The study of capillary pressure results in direct assessment of the capillary trapping capacity of CO_2 within a CCS project. Thus, in this investigation, a numerical approach is employed to analyse the effect of inlet fluid flow rate and wettability (in terms of contact angle) on pore-scale $scCO_2$ capillary pressure for various drainage and imbibition cycles for sand pack and sandstone followed by $scCO_2$ capillary trapping capacity.

2.2.3.2. Literature review on capillary trapping capacity

Widenschild et al. (2011) conducted core-flood experiments to estimate the effects of interfacial tension, viscosity and fluid flow rate on capillary trapping in synthetic glass beads. Results showed that initial non-wetting phase saturation values are optimized at decreasing non-wetting phase viscosities and low drainage flow rates. For residual non-wetting phase saturation values, the observed situation was the opposite.

However, they suggested further research in this regard. Iglauer et al. (2011) investigated the impact of the initial non-wetting-phase saturation and porosity on the residual non-wetting-phase saturation in sand packs and consolidated sandstones. The optimal porosity for CO_2 storage was around 22% for a measured maximum trapping capacity of 11%. Pentland et al. (2011) estimated primary drainage capillary pressure and the relationship between initial and residual non-wetting phase saturation through core-flooding experiments for a $scCO_2$-brine system in Berea sandstone. Their results demonstrated that the observed maximum trapped CO_2 saturation was 35%, which was less than the maximum trapped saturation of 48% for an equivalent n-decane/brine experiment in Berea sandstone. Pini et al. (2012) showed the influence of sub-core-scale capillary heterogeneity on fluid saturation at pore-scales for a CO_2-water system. They conducted laboratory experiments and measured fluid saturation with a micro-CT scanner. Suekane et al. (2010) investigated the micro-level mechanism of residual gas trapping in Berea sandstone. They used a micro-CT scanner to observe the fluid distribution in Berea and Tako sandstones. Moreover, they investigated the influence of capillary number and injected water amount on residual trapping in glass beads. The results showed that low-porosity reservoir rocks are good for residual trapping.

Pore-scale modelling is beneficial for studying various petro-physical parameters (such as capillary pressure) under different wettability conditions. With advances in numerical modelling, these various wettability conditions can be assigned as contact angles. Thus, it is relatively convenient to examine the numerical outcomes of various drainage and imbibition cycles in terms of capillary pressure and capillary trapping capacity. As the oil and gas industry has a desire to store more CO_2 safely within geological sources, this numerical procedure for estimating capillary pressure will add much to the future research and technology.

2.3. *Some important parameters central to this study*

2.3.1. Capillary Number

2.3.1.1. General Discussion

The capillary number is the dimensionless ratio of the viscous to capillary force. It is denoted by N_c. When $N_c > 1$, then the viscous force dominates the capillary force and vice versa. Generally, an N_c value of approximately 10^{-6} allows flow through pores in

a reservoir. According to Chatzis and Morrow (1984), the equation for capillary number is,

$$N_c = \frac{\mu v}{\sigma} \hspace{6cm} (2.3)$$

Where,

N_c = capillary number

μ = fluid viscosity

v = fluid velocity

σ = surface tension

In this work, fluid velocity values were considered to ensure that the capillary number remained greater than 10^{-6}. So, fluid velocities can be used to investigate their influence on fluid residual saturation and, thus, on the shape of the fluid relative permeability curves as described by Krevor et al. (2012). Moreover, as fluid relative permeability values are used in this work to predict capillary pressures, capillary numbers greater than 10^{-6} impose an effect on capillary pressure values.

2.3.1.2.　　Capillary numbers considered in this thesis

In this work, different capillary numbers are used during various fluid displacement processes. They are listed below in Table 2.1.

Table 2.1: Capillary numbers used in various fluid displacement processes

Reservoir rock ╲ Capillary number	Ottawa F42 sand pack	Berea sandstone
Drainage capillary number	1.5×10^{-5} 2.0×10^{-5}	1.0×10^{-3} 1.2×10^{-3}
Imbibition capillary number	1.5×10^{-5} 2.0×10^{-5} 1.0×10^{-6}	1.0×10^{-3} 1.2×10^{-3} 1.0×10^{-5}

2.3.2. Displacement mechanisms during drainage and imbibition processes

In a two-phase system, when a wetting fluid is displaced by a non-wetting fluid, it is called *drainage*. The reverse case is referred to as *imbibition*.

During the drainage process, not all of the wetting phase fluid is drained out of the pore spaces of the reservoir rock. Some amount of wetting phase is typically located

in the reservoir rock's smallest pores, which is treated as an irreducible amount of wetting fluid saturation (S_{wirr}). This is because the capillary forces required to remove the amount of fluid from these pore spaces is too large to overcome the lowest possible capillary pressure in the pore-body. Even though the capillary pressure will continue to increase, the disconnected wetting phase fluid will not be able to leave the pores. This situation is dependent on the fluid-phase topology in the locality of the pore-body. Once this lowest possible capillary pressure, or *threshold pressure,* is achieved, the fluid-fluid interface approaches quickly into the neighbouring pore-body. Alternatively, this can be called the *entry pressure*. As the capillary pressure is inversely proportional to the pore radius, the non-wetting phase can enter the pores only when the entry pressure associated with the pore (with the smallest radius) has been exceeded. This phenomenon is known as *piston displacement*. After this, the capillary pressure will continue to increase until the drainage cycle reaches equilibrium naturally or is stopped forcibly.

During the imbibition process, the wetting fluid is injected into the pore spaces and preferentially fills up the smaller pores first (Blunt, 2002). This is mainly due to the reduced amount of capillary pressure. The non-wetting fluid may be surrounded by the wetting fluid due to the difference in the pressure values.

There are multiple displacement mechanisms during drainage and imbibition cycles. They are *snap-off*, *invasion percolation*, and *piston-like filling* in pores and throats. When the pore spaces are occupied by the non-wetting phase, a film of wetting phase is presented in the pore perforations. As the non-wetting phase deescalates from the pore-throats, the amount of local capillary pressure decreases. The situation results in the expansion of the wetting film. Below a certain capillary pressure, the non-wetting phase presented in the pore-throat becomes unstable and also deescalates into the neighbouring pore-bodies. This phenomenon is known as *snap-off* (Blunt, 2002).

During the invasion percolation process, pores and throats are filled with fluids with the lowest possible non-wetting phase pressure. If for the first displacement, the largest throat is connected to the inlet, then wetting fluid within the throat (which is filled with wetting phase initially in a completely water/brine-wet system) is replaced by non-wetting fluid. In the next step, either the largest throat connected to the inlet or any pore adjacent to the filled-up throat can be filled up with the wetting phase again. This

process is repeated and causes increases in capillary pressure as smaller pores/throats are filled over time (Blunt, 2002).

In piston-like pore filling process, the main challenge is the number of water/brine filled adjacent throats. For this reason, empirical equations are used to determine capillary pressure values during the pore-filling process (Blunt, 2002). In piston-like throat filling, the opposite situation to non-wetting phase invasion occurs. This process is also critical to explain because the wetting phase moves into the throat, which is also filled with the same wetting phase in a two-phase system (Blunt, 2002).

2.3.3. Wettability

Wettability is the ability of a porous rock to retain contact with one of the fluid phases when there are two or more immiscible fluids within the system. It is a vital factor which governs the fluid flow distribution and mechanisms in the reservoir. Depending on the wettability, any reservoir rock may be water-wet, oil-wet or mixed-wet, where the contact angles are less than 90°, greater than 90° or close to 90°, respectively. Generally, saline aquifers suitable for geological sequestration of CO_2 are water-wet and oil reservoirs for enhanced oil recovery (EOR) are oil-wet.

The objective of this thesis is to alleviate the impacts of CO_2 on climate change by applying a safe and efficient CCS system. In this regard, the wettability of CO_2-brine-rock systems can play a major role in the effective and safe management of CO_2 entrapped within subsurface geological formations (saline aquifers and depleted oil reservoirs). This is because, in a single pore of any subsurface geological formation, different parts of the pore have different wettability values (Øren & Bakke, 2003). Moreover, fluids may organize themselves in different sizes of pores within geological formations, which is also dependent on their wettability values. Thus, different values of fluid saturation can be obtained at different fluid displacement cycles (drainage and imbibition). These fluid distribution scenarios within pore spaces, in turn, create significant impacts on fluid relative permeability and capillary pressure values. To investigate the effect of wettability (in terms of contact angles) on fluid relative permeability and capillary pressure at the pore scale, this work presents numerical simulation results and suggests future work. Furthermore, the impact of wettability can be very crucial for CCS project economics if it is extended to the reservoir scale. However, this is beyond the scope of this work.

2.3.4. Surface tension

Surface tension is a phenomenon in which the surface of a liquid faces tension due to the various intermolecular forces present within the liquid.

In this work, a value of 0.036 N/m is used for surface tension of $scCO_2$-brine. Also, the free surface flow model (Brackbill et al., 1992) is incorporated in ANSYS CFX, which is used to perform simulations of various drainage and imbibition cycles. In this model, a completely new method has been developed to incorporate surface tension effects on the movement of fluids at the pore scale. This surface tension model simplifies the calculation steps for surface tension and, thus, proceeds a step further to determine the influence of surface tension forces during numerical modelling of surface force-driven 3D fluid flow. The basis of this model is to apply a force density at each and every point of transition between fluids of different properties that is simply proportional to the curvature of the transition.

2.4. Description of some other important parameters

An outline of the two-phase pore-scale displacement mechanisms along, with a description of some important parameters, are presented in this section to provide a basis for understanding this thesis.

2.4.1. A brief history of carbon capture and storage (CCS)

In the late 1970s, the concept of CCS was first proposed by two researchers (Holloway et al., 2001). However, original research on CCS did not start until the early 1990s. Outstanding progress was made during this time regarding the prediction of injected CO_2 within geological formations. In the Sleipner gas field in the Norwegian North Sea, the first successful CCS test in a brine-saturated formation was performed. In the Sleipner project, CO_2 stripped from the produced natural gas was injected into the Utsira formation, which is basically a sand layer. The injection process started in October 1996 at a rate of 1 million tonnes per year. Over 10 million tonnes of CO_2 have now been injected. To-date, no notable operational problems have been observed (Jacobsen et al., 2008; Chadwik, 2014). In 2015, the Norwegian Government reviewed feasibility studies at Mongstad Refinery, Norway, and hoped to have a full-scale carbon capture demonstration project operational by 2020.

In the Salah on-shore gas field project in Algeria, a CCS project is already in operation. This project is situated in the Ahnet-Timimoun Basin in the Algerian Central Sahara. CO_2 produced from eight gas fields is injected into the producing hydrocarbon reservoir zones. The capacity of the site is 1.2 million tonnes per year (Riddiford et al., 2003).

According to the European Archive UK Government Web Archive, the Government of the United Kingdom launched a first tender process for a CCS demonstration project in 2007. This first CCS tender was cancelled in late 2011 due to the terms and cost associated with the Scottish Power/Shell/National Grid consortium. A second tender process was launched by the government in 2012. This second tender was cancelled in November 2015 following a government review. According to a memorandum of the UK Parliament, a large-scale CO_2 injection project into a depleted oil field named the Miller Field, was planned. Due to financial constraints, this project was not implemented.

The Weyburn field project in Canada was the first project which focused on using CCS and enhanced oil recovery (EOR) techniques together. According to grist.org, the coal-fired Boundary Dam Power Station in Saskatchewan, Canada, started in May 2011 and became operational in October 2014. As serious design and maintenance issues were found in the CCS system, this project operated only 40% of the time.

2.4.2. A brief literature review of numerical simulation of CCS

Numerical simulation can be used to analyse the movement of CO_2 at pore-scale. As monitoring of injected and trapped CO_2 is essential for the safe preservation of CO_2 in storage sites, numerical simulations create a CO_2 injection strategy which maximizes CO_2 storage volume and minimizes leakage risk. Thus, for an effective CO_2 storage design, researchers and engineers can predict CO_2 distributions and flow paths along with those of other fluid phases through numerical simulation.

The stochastic 3D model of the Frio formation (from the upper gulf coast of Texas) was used to investigate physical processes during CCS (Doughty & Pruess, 2004). The model was developed with the help of the TOUGH2 simulator to address vertical and lateral grid resolution, grid orientation effects, and the choice of characteristic curves. They did not consider chemical reactions between CO_2 and rock minerals. They concluded that non-wetting phase entrapment is potentially important and the choice

of residual solutions is dependent on the flow process. Qi et al. (2009) presented a CCS design strategy through the incorporation of a recently developed trapping model generated from a field-scale streamline-based simulator. Gas trapping and relative permeability hysteresis were included in the model. The basis of the model was pore-scale modelling results. Sensitivity studies were performed and the results demonstrated that the proposed CCS strategy was very sensitive to the estimated residual CO_2 saturation. Michael et al. (2010) published a review paper on existing CCS operations and shed light on future commercial storage operations (injection strategies, brine displacement situations). Hesse et al. (2010) numerically modelled complex geometries to show steady buoyancy-dominated flows as a cascade of flux partitioning events. With the help of this approach, they analysed 2D plume dispersal from a horizontal injection well. Finally, they revealed that the upscaling process of small-scale flow barriers, which is a very common practice in numerical simulation regarding CCS, didn't represent the entrapment of CO_2 accurately.

2.4.3. A brief literature review on storage sites for CCS

Three different sites (deep saline aquifers, oil reservoirs and gas reservoirs) can be suitable storage sites for CCSs. A concise description of these is presented below.

2.4.3.1.   Deep saline aquifers

Saripalli et al. (2000) demonstrated that deep saline aquifers can act as cost-effective and efficient storage sites. The requirements are that they have a good geological top seal, a large volume, and reasonable permeability and pressure. If these conditions can be maintained accurately, then trapped CO_2 can be retained within aquifers for long periods without any risk of leakage and unnecessary increase in saline aquifer pressure. Ennis-King et al. (2005) suggested that residual gas trapping, dissolution of CO_2 and the balance between up-dip migrations are the factors that control the final distance travelled by trapped CO_2. They proposed that convective mixing is the perfect mechanism for the dissolution of CO_2 in formation water. TOUGH2 was used in their work to model the solubility of CO_2 in formation water as a function of temperature, pressure and salinity. It was evident from their work that, in the course of time, CO_2 is trapped in a mobile layer underneath cap-rock. Pruess et al. (2001) introduced and described a new term: *capacity factor* (the fraction of the aquifer pore volume that is accessible to CO_2). Also, they studied the amount of trapped CO_2 at different phases under different conditions in typical saline aquifers. However, they neglected reservoir

heterogeneity, hydrodynamic instability and capillary effects along with other properties. Spiteri et al. (2005) applied relative permeability hysteresis to model CCS. They proposed a new technique for entrapment of CO_2 and measurement of water-flood relative permeability through pore-network simulation. The results showed that hysteresis is the most important factor for predicting the migration and final distribution of CO_2. Obi et al. (2006) developed a streamline-based simulator to study CCS in a deep saline aquifer by incorporating equilibrium mass transfer between phases and rate-limited reactions. Their results illustrated that dispersion can have an impact on the shape of the contaminant plumes at the field scale and that the transport of CO_2 is dominated by high-permeability channels.

2.4.3.2. Oil reservoirs

Lake et al. (1990) suggested that miscible flooding is the key mechanism behind EOR by CO_2 injection. The process of miscible flooding is the summation of the extraction of hydrocarbon from the oil into the CO_2, and the dissolution of CO_2 into the oil. Taber et al. (1997) demonstrated the disadvantage of CO_2 flooding in EOR processes due to the unfavourable mobility ratio between oil and CO_2. However, they estimated that this process can be widely used in sandstone and carbonate reservoirs with a wide range of permeability values and thicknesses of hydrocarbon-bearing zones. Gough et al. (2010) proposed that oil reservoirs are the most effective CCS storage sites, not only for CO_2 entrapment but also for EOR. Dai et al. (2013) demonstrated some optimization techniques in order to increase both CO_2 storage and oil recovery. They are water alternating gas (WAG) injection, CO_2 injection in the capillary transition zone, injection of CO_2 into an aquifer below the reservoir, and usage of horizontal wells for both injector and producer.

2.4.3.3. Gas reservoirs

Orr and Silva (1987) demonstrated the basic transport mechanism relevant to the use of CO_2 for pressure maintenance and condensate vaporisation in CCS. Calabrese et al. (2005) reported that if CO_2 is injected in a gravity-stable manner in a storage site, the dispersive mixing between CH_4 and CO_2 is minimal at the field scale. Bear (2013) demonstrated the diffusion mechanisms of CO_2 storage elaborately in his book. According to his work, they are convective diffusion, molecular diffusion and mechanical dispersion. He suggested that for effective CCS and pressure maintenance

purposes, the tendency of CO_2 to mix with CH_4 and the resulting CO_2 concentration in the storage site are very important.

2.4.4. Trapping mechanisms

There are four recognised trapping methods for storing CO_2 within the pore spaces of geological reservoirs. They are:

(i)   Stratigraphic and structural trapping;

(ii)   Solubility trapping;

(iii)   Mineral trapping; and

(iv)   Residual or capillary trapping.

These trapping mechanisms are presented graphically in Figure 2.2.
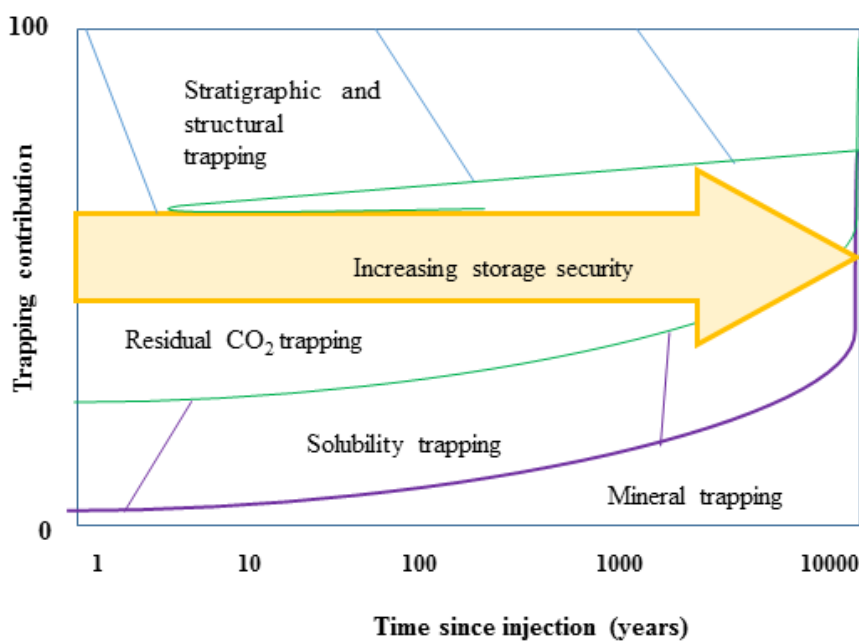
Figure 2.1: Contribution of different trapping mechanisms as a function of time (source: adapted from IPCC SRCCS 2005).

In the first type of trapping mechanism, stratigraphic and structural trapping, and upward relocation of buoyant CO_2 is blocked by an impermeable barrier in the reservoir or saline aquifer, commonly known as *cap rock*. Therefore, stratigraphic and structural trapping plays an important role in securing CO_2, as shown in Figure 2.1. However, there is the chance of CO_2 leakage through the cap seal. Also, trapped CO_2 can escape to the surface through penetration into the wells. Thus, it is hardly possible

to speed up stratigraphic and structural trapping compared to the other three trapping mechanisms. With this drawback, it is very difficult to change the geological structure of the formation which, in turn, makes stratigraphic and structural trapping less favourable than other trapping mechanisms.

The second type of trapping mechanism, solubility trapping, occurs when CO_2 is dissolved into the formation brine, and dense CO_2-saturated brine descends into the storage site (Riaz et al., 2006; Burnside et al., 2014). The third type of trapping mechanism, mineral trapping, occurs when dissolved CO_2 reacts with the formation brine or solid minerals (which originate from the host rock), as suggested by Xu et al. (2003). In terms of security, mineral trapping is best. However, it is actually a long-term process and may require many years for effective trapping (IPCC, 2005).

The fourth mechanism, residual or capillary trapping, is more expeditious compared to the other three types and may take from several months to years to be completed, as suggested by Burnside et al. (2014). As the capillary pressure influences CO_2 plume migration and the determination of $scCO_2$ capillary pressure at the pore scale is quite complex, the understanding of the mechanism behind this trapping category is quite complex. Moreover, identification of the factors which influence this trapping mechanism is important, especially to ensure integrity and long-term CO_2 storage security.

2.4.5. Porous Media

A porous medium consists of a solid structure (rock matrix) and interconnected or disconnected voids (pores). Any fluid (gas or liquid) may stay within the pores of a reservoir rock. Biological structures (lungs and bones); artificial material (cements, textiles); geological media (sand, sandstone and carbonates) are examples of porous media. If any fluid (liquid or gas) can pass through the porous medium, then it called *permeable* porous media. The opposite is known as *impermeable* porous media. Also, porous media can be divided into either *consolidated* or *unconsolidated* types. Consolidated media (limestone or sandstone) can be compacted over time. On the other hand, unconsolidated media (sand or sand pack) are less densely packed and have larger pore spaces compared to consolidated media.

Immiscible fluids include any two fluid pairs (for instance, oil-water or gas-water) with limited mutual solubility that form two separate phases. In a water-wet immiscible

system (gas-water), the rock (solid) is preferentially surrounded by water, because the attractive forces are stronger between water and rock than between gas and rock. Thus, in a two-phase (fluid) system, a fluid with a stronger tendency to be attracted to and absorbed by the surrounding solid (rock) than the other fluid, can be defined as *wetting fluid*. The other fluid is referred to as *non-wetting fluid*. The distribution of the wetting and non-wetting fluids in a two-phase system within the pore spaces of any rock is influenced by the two factors: the pore geometry and wettability of the porous medium (Blunt, 2001).

Nowadays, an analysis of fluid flow through porous media for two-phase flow (scCO$_2$-brine or oil-brine) is significant for several applications (especially CCS and EOR). In order to develop an effective microscale numerical model, a good understanding of pore-scale fluid flow mechanisms is essential. However, microscale analysis is more complicated than macroscale analysis, and two-phase micro-scale analysis is more complex than that of single-phase flow. Due to the considerable interaction among gravitational, viscous and capillary forces, and the presence of various physical phenomena, it is challenging to blend microscopic parameters together with essential physics (Blunt, 2001).

2.4.6. Porosity

In a porous medium, porosity represents the fraction of the total volume of the pore space. Actually, for most experimental and numerical applications, *effective porosity* is used, which is the fraction of the total volume of the pore spaces that are connected to each other within the porous medium.

2.4.7. Representative Elementary Volume (REV)

The representative elementary volume (REV), is the minimum volume required to obtain an accurate computation for an average representative quantity. For volumes smaller than the REV, an average representative quantity or property cannot be defined. In other words, REV is the smallest volume in which a measurement can be performed that will produce a realistic result. The most common representative quantities are electromagnetic properties, thermal properties, hydrogeological properties, etc.

In pore-scale fluid flow within geological rock samples, REV is a common term used to describe the 3D representation of a reservoir rock at the microscale. REV is

dependent on the sample rock and the property being averaged. To achieve REV in the micro-pores of geological reservoir rocks, an initial measurement of the porous samples is required. Then, the sample size is increased gradually and the uncertainties are reduced. In the course of time, the sample size becomes large enough to achieve consistent readings, which is called REV.

2.4.8. Absolute Permeability

Absolute permeability is a measure of the ability of a porous material (soil, granular beds and porous rocks) to allow fluids to pass through it. According to Darcy's law,

$$Q = -\frac{kA(P_b - P_a)}{\mu L} \tag{2.4}$$

Where the total discharge rate, Q (m^3/s) is equal to the product of the intrinsic permeability of the medium, κ (m^2), the cross-sectional area of flow, A (m^2), and the total pressure drop $(P_b - P_a)$ (Pa), divided by viscosity μ (Pa·s), and the length over which the pressure drop is taking place, L (m).

The above equation for single-phase (fluid) flow is the basic equation for absolute permeability (single-phase permeability) determination. The negative sign is required as fluid flows from the high pressure to the low-pressure area. To perform an experimental calculation of absolute permeability and for the above equation to be valid, some criteria must be satisfied. The criteria are: the flow must be laminar, incompressible and horizontal, 100% saturation with fluid must be achieved, and there must be no chemical reactions between the sample rock and the fluid. Moreover, grain size and sorting, residual water saturation, porosity, and cementation, influence the absolute permeability determination. An accurate representation of absolute permeability will provide subsequent relative permeability studies with better quantitative results.

3. Chapter 3 Numerical modelling for two-phase (scCO$_2$-brine) flow into porous media

Pore-scale multiphase flow behaviour influences various macroscopic properties of geological porous media (capillary pressure and relative permeability). Many methods have been developed to create three-dimensional (3D) representations of geological porous media with the help of computers during recent decades to better understand multiphase flow behaviour and its influences on various properties of fluids and porous media (e.g. rock). Huge advancements in computer science, physics and mathematics have enabled researchers and scientists to observe the inner structures of porous rocks via various methods. Among all of these methods, micro-CT imaging is a direct method that can provide a high-resolution 3D structure of the pore spaces of geological reservoir rock. These images of the micro-pores of samples can be used to create a numerical model (through a numerical simulator), which will act as a mirror image of the reservoir sample. Then, the governing factors controlling the flow pattern within the porous media can be investigated. There are many commercially available numerical solvers which not only create exact 3D replicas of reservoir samples but also employ various numerical methods to deal with these investigation processes.

To obtain solutions for two-phase flows, a numerical algorithm is adopted in numerical solvers, which is described in detail in Versteeg and Malalasekera (1995). In this numerical algorithm method, the region of interest is divided into small sub-regions called *control volumes*. For each control volume, the equations are discretised and solved iteratively. So, an approximate value for each variable at specific points throughout the domain can be obtained, which is equal to a full pore-scale representation of the flow behaviour. In this work, the commercial computational fluid dynamics (CFD)-based solver ANSYSCFX is utilized for this purpose.

This chapter presents a discussion of numerical modelling for two-phase flow through porous media. This discussion covers the governing mathematical model used for pore-scale simulation, and the prepossessing of numerical models to conduct pore-scale simulation studies using a CFD-based simulator with specific reference to using scCO$_2$ and brine as fluids, and Ottawa F42 Sand Pack, Berea sandstone, and Bentheimer sandstone as porous media.

3.1. Governing Mathematical Model

Although the Darcy equation is used as one of the fundamental principles to analyse fluid flow through porous media, especially in the field of petroleum engineering, this equation can be related to microscale governing equations with the help of Stokes' law (Narsilio et al., 2009). The flow of fluid through a medium can be described by Navier-Stokes equations, which comprise continuity and momentum equations.

The general continuity equation (ANSYS CFX Solver Theory Guide, 2006) is given by:

$$\frac{\partial \rho}{\partial t} + \nabla \cdot (\rho \mathbf{v}) = 0 \tag{3.1}$$

The general momentum equation (ANSYS CFX Solver Theory Guide, 2006) is:

$$\frac{\partial \rho \mathbf{v}}{\partial t} + \nabla \cdot (\mathbf{v}\mathbf{v}) = -\nabla p + \nabla \cdot \boldsymbol{\tau} + \mathbf{F} \tag{3.2}$$

Where ∇ the divergence, v is the velocity vector, p is pressure, and ρ is density. **F** is the force vector, which includes the gravity vectors (**F$_g$)** due to body force and force due to interfacial tension (**F$_s$**) at the interface between the fluid phases, and can be expressed as:

$$\mathbf{F} = \mathbf{F_g} + \mathbf{F_s} \tag{3.3}$$

Finally, $\boldsymbol{\tau}$ is the viscous stress tensor. The stress tensor is associated with strain rate and can be expressed as:

$$\boldsymbol{\tau} = \mu[\nabla \mathbf{v} + (\nabla \mathbf{v})^{\mathrm{T}}] \tag{3.4}$$

The following assumptions are made during pore-scale simulation of a supercritical CO_2 (scCO_2) and brine system using the ANSYS-CFX simulator:

- The change in fluid densities (i.e. densities of scCO_2 and brine) at the pore scale at very low flow rates or velocities is very small or negligible.
- The fluids in pores flow in isothermal conditions (i.e. the fluids are in a state of thermal equilibrium); and
- The dissolution effect at the scCO_2-brine interface is very insignificant, so the mass exchange rate at the interface of scCO_2 and brine is neglected.

The force vector due to body force in Equation 3.3 is accounted for in terms of buoyancy force, and is given by (ANSYS CFX Solver Theory Guide, 2006):

$$\mathbf{F_g} = (\rho - \rho_r)\mathbf{g} \qquad\qquad 3.5$$

Where ρ_r is the density of the fluid at the reference location ($\vec{r}_r$), which is calculated in ANSYS-CFX based upon absolute pressure using the equation (ANSYS CFX Solver Theory Guide, 2006).

$$p_{abs} = p + p_r + \rho_r \vec{g}(\vec{r} - \vec{r}_r) \qquad\qquad 3.6$$

Where p_r is the pressure at the reference location and p_{abs} is the absolute pressure. p_{abs} is used to evaluate fluid properties that is the function of pressure. The components of the gravity vector $\mathbf{g}$ in the x, y and z directions are: $g_x = 0$, $g_y = -9.81$ m/s, and $g_z = 0$.

The other force term due to surface tension is modelled in ANSYS-CFX based upon the continuum free surface model proposed by Brackbill et al. (1992). Further details of this model are discussed later in Section 3.1.1. The forces due to interfacial tension are also discussed in Section 3.1.1.

3.1.1. Numerical solution using ANSYS-CFX

To obtain solutions for two-phase $scCO_2$-brine flow, the governing equations discussed in Section 3.1 and the commercial CFD-based solver ANSYS-CFX are utilized. The samples considered include Ottawa F42 Sand Pack, Berea sandstone and Bentheimer sandstone. Models of these samples were constructed from high-resolution X-ray computed tomography (micro-CT) images. Further details of the image processing and numerical model construction are discussed below in Section 3.2.

In ANSYS CFX, an Eulerian-Eulerian multiphase flow approach was utilized to solve the momentum, pressure-based continuity and volume fraction equations (ANSYS CFX-Solver Theory Guide, 2017). The pressure gradient at the interface between brine and $scCO_2$, and the interphase momentum transfer were calculated using the free surface flow model (Brackbill et al., 1992). In this model, the surface tension force is considered as a volume force concentrated at the interface. The continuum surface force model was considered in the free surface flow model to describe surface tension force. In this work, brine was considered as a primary fluid, and $scCO_2$ was considered

as the secondary fluid (Figure 3.1). Figure 3.1 illustrates the free surface interface between brine and scCO$_2$ within the pore spaces of the geological samples. Brine and scCO$_2$ are denoted by α and β, respectively.
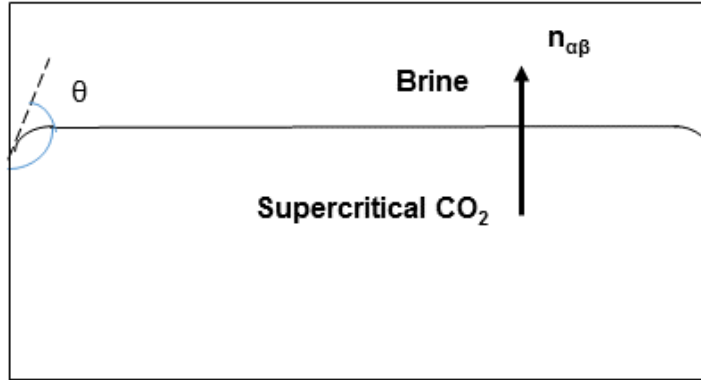
Figure 3.1 Free surface interface between brine and scCO2 at the pore level (after ANSYS-CFX Solver Theory Guide, 2006).

In Figure 3.1, when the interface between brine and scCO$_2$ intersects a wall, the estimation of wall adhesion can be evaluated by specifying the contact angle. The interface normal vector $\mathbf{n}_{\alpha\beta}$ must satisfy the wall contact angle θ.

According to the continuum surface force model (ANSYS CFX-Solver Theory Guide, 2006), the surface tension force, F$_{\alpha\beta}$ is given by:

$$F_{\alpha\beta} = f_{\alpha\beta} . \delta_{\alpha\beta} \tag{3.7}$$

Where,

$$f_{\alpha\beta} = \sigma_{\alpha\beta} k_{\alpha\beta} \mathbf{n}_{\alpha\beta} + \sigma \nabla_s \tag{3.8}$$

and,

$$\delta_{\alpha\beta} = |\nabla r_{\alpha\beta}| \tag{3.9}$$

$$S_{\alpha\beta} = \nabla . \mathbf{n}_{\alpha\beta} \tag{3.10}$$

In these equations (3.7-3.10):

$\sigma_{\alpha\beta}$ = surface tension coefficient;

$\boldsymbol{n}_{\alpha\beta}$ = interface normal vector pointing from brine to scCO$_2$ (calculated from the gradient of a smoothed volume fraction);

∇_s = Gradient operator on the interface; and

S = surface curvature.

The right-hand side of Equation 3.8 describes the normal and tangential components of the surface tension force, respectively. The normal component arises from the interface curvature and the tangential component from variations in the surface tension coefficient. The left-hand side of Equation 3.9 is known as the *interface delta function*. The value of this term approaches zero away from the interface, which again expresses that the surface tension force is active only near the interface.

To track the interface between scCO$_2$ and brine, the laws of conservation of mass and momentum between the scCO$_2$ and brine volume fractions were employed. The volume fraction of the qth phase, V_q, is expressed by:

$$V_q = \int_V \alpha_q dV \qquad 3.11$$

Where

$$\sum_{q=1}^{n} \alpha_q = 1 \qquad 3.12$$

These equations are treated as the core of fluid flow modelling (ANSYS CFX-Solver Theory Guide, 2006). For a particular set of boundary conditions (for instance, inlets, outlets and walls), the fluid velocity, pressure etc. can be predicted for a given sample through these equations.

An Eulerian-Eulerian multiphase flow model was employed for this thesis. Within the Eulerian-Eulerian model, certain interphase transfer terms (for example, calculation of interfacial area density), can be modelled using the free surface model discussed earlier.

The interphase momentum transfer, $M_{\alpha\beta}$, occurs due to the interfacial forces acting on each phase (brine and scCO$_2$). The details of the model can be found in the ANSYS CFX-Solver Theory Guide (2006). The total force on phase α (brine) due to interaction with the other phase β (scCO$_2$) is expressed as M_α and is given by:

$$M_\alpha = \sum_{\beta \neq \alpha} M_{\alpha\beta} \qquad 3.13$$

The interfacial forces between the two phases are equal and opposite, so the sum of the net interfacial forces is zero:

$$(M_{\alpha\beta} = -M_{\beta\alpha}) \text{ Or, } \sum_\alpha M_\alpha = 0 \qquad\qquad 3.14$$

The total interfacial force acting between two phases may arise from various independent physical forces (interphase drag force, lift force, wall lubrication force, virtual mass force, turbulence dispersion force, etc.). In ANSYS CFX, there are different physical models that can explain these forces. In this thesis, the 'interphase drag model' is used to describe the total interfacial drag force between the brine and scCO$_2$. For the interphase transfer, the dominant force was the drag force with a drag coefficient of 0.44 N/m. The total drag force was calculated from the dimensionless drag coefficient, which is given by (ANSYS CFX-Solver Theory Guide, 2006):

$$C_D = \frac{D}{0.5\,A\,\rho_\alpha\,(U_\alpha - U_\beta)^2} \qquad\qquad 3.15$$

Where ρ_α is the fluid density of phase α, $(U_\alpha - U_\beta)$ is the relative speed of phases α and β, D is the magnitude of the drag force and A is the projected area of the body in the direction of flow. The continuous phase is denoted by α, and the dispersed phase is denoted by β.

3.2. *Assumptions and pre-processing of the numerical model*

AVIZO and ANSYS ICEM CFD were used to create a surface mesh and volume mesh of the geological samples (Ottawa F42 Sand pack, Berea and Bernheimer sandstone) based on micro-CT images. These volume meshes were used to run simulations of the various drainage and imbibition processes. For the various drainage and imbibition processes, inlet fluid velocities were calculated from various capillary numbers (1.5×10^{-5}, 10^{-3}, 2×10^{-5}, 1.2×10^{-3}, 1.0×10^{-6} and 1.0×10^{-5}). Furthermore, different values of contact angles were considered for the simulation of drainage (5° and 45°) and imbibition (30°, 45° and 85°) processes, respectively. The results of these simulations are discussed elaborately in subsequent chapters (Chapters 4, 5 and 6). Figure 3.2 shows a 3D view of an example pore-scale model processed by AVIZO.
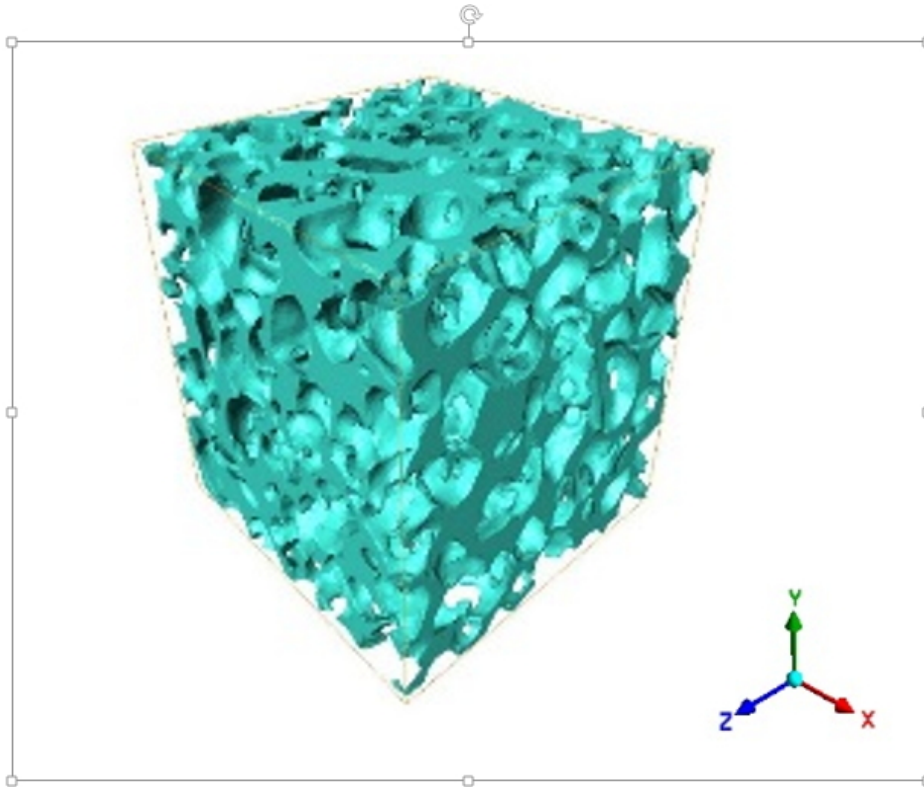
Figure 3.2: Example 3D model of the Ottowa F42 Sand Pack showing pore spaces (processed by AVIZO).

For the simulations, the following assumptions were made:

- The $scCO_2$ is at supercritical state within the entire computational domain.
- The fluid flow is an unsteady-state flow.
- The geological samples are initially fully saturated with brine.
- Within the pore spaces, the samples, $scCO_2$ and brine are in an immiscible phase, and the effect of mutual dissolution was neglected.
- In Figure 3.2, a cube is represented by the voxel of the Ottawa F42 Sand Pack. In this cube, it is assumed that all faces are impermeable except the inlet and outlet. So, the fluids cannot penetrate through the other walls.
- Both fluids (brine and $scCO_2$) move in three dimensions (x, y, z) within the cube. Although $scCO_2$ is considered as compressible fluid, and brine is generally incompressible, both fluids are assumed to be incompressible (their densities are constant) in order to simplify the simulation process. This infers

that spatial and temporal variations in density were neglected relative to the velocity components (u, v, w).

- Fluid velocities are taken in all three directions (x, y, z). Fluid velocities in the x and z directions were considered to equal zero. So, the flow remained invariant in these directions. Only the velocity in the y-direction was considered and took the effect of gravity during the numerical simulation.

A flowchart for the creation of the surfaces and volume meshes of the samples is presented in Figure 3.3.
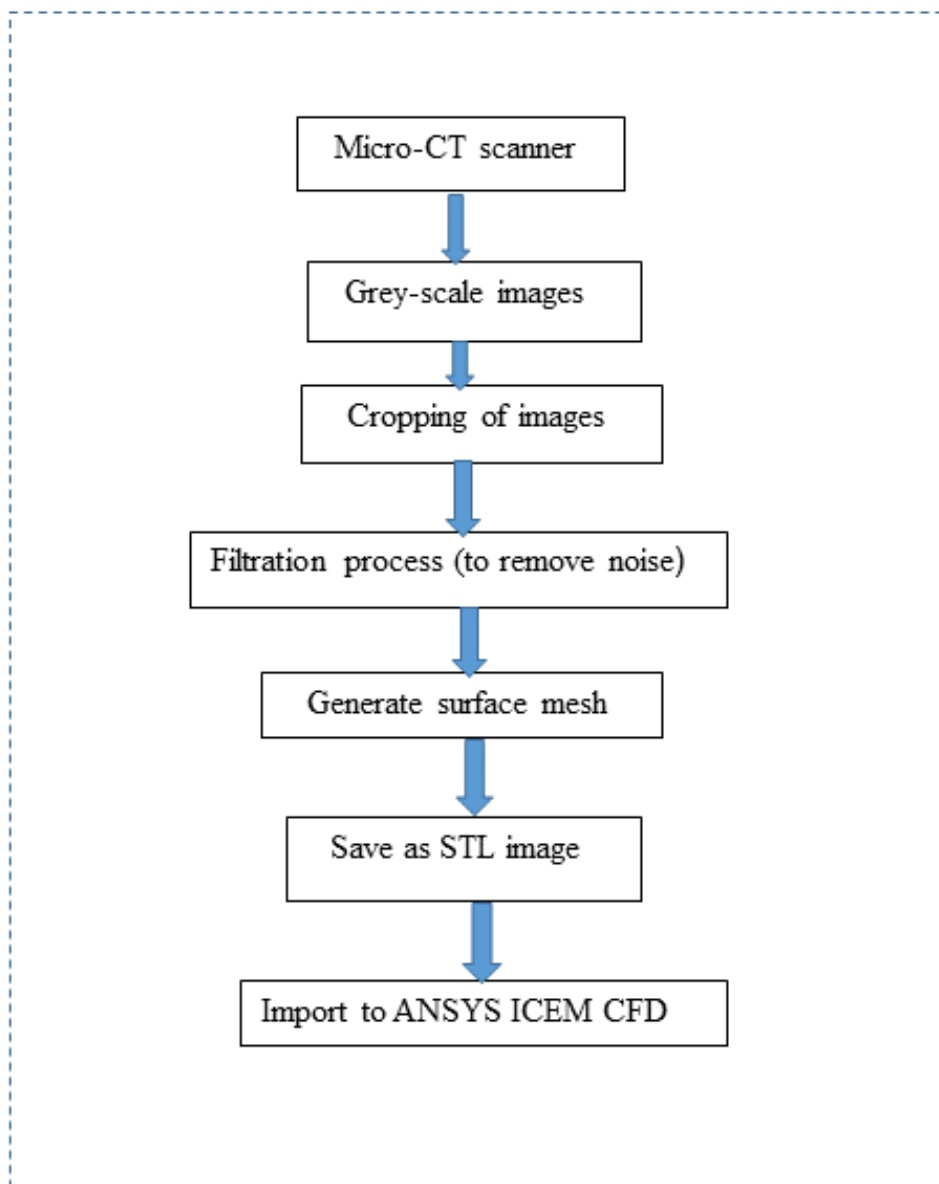
Figure 3.3: Flowchart illustrating the procedure for creating a numerical model from micro-CT images.

The micro-CT images of the samples were obtained as two-dimensional (2D) slices of 16-bit greyscale images, as shown in Figure 3.4. The image dimensions used in the model are approximately $300 \times 300 \times 300$ voxels (1 voxel $\cong 5.84\,\mu m$). The pore spaces of these images were separated from grains after segmentation using AVIZO image processing software (Avizo Software User's Guide, 2018). It can be seen in this sample image (Figure 3.4) that the pores are void and connected with each other through narrow ducts and throats. The individual pores are segmented with the watershed algorithm. Segmentation of the greyscale voxel volume (element volume) was conducted based upon the histogram of the luminosity values of all voxels. The peaks and valleys in the histogram were used to differentiate between solid (rock) and void (pore). This histogram, along with the watershed segmentation process, eliminates arbitrary voxel misidentification (Andrew et al., 2014). After completion of the segmentation process, in the generated matrix, solid and void were represented by 1 and 0, respectively. After the watershed segmentation process was completed, the segmented pores could be visualized as shown in Figure 3.5, which can be used to generate a surface mesh.

In the greyscale image shown in Figure 3.4, each greyscale tone refers to the X-ray mass absorption coefficient of the specific voxel. The greyscale values were assigned to different phases for quantitative analysis, such as rock or air and, consequently, porosity and absolute permeability were estimated. The accuracy of the estimation of absolute permeability strongly depends on the quality of the segmentation process discussed above.

These 2D images were stacked to form the 3D image shown in Figure 3.6, and to generate surface meshes. The generated surface meshes were further simplified by the surface simplification editor in AVIZO.

The quality of the AVIZO-generated models was further controlled by conducting intersection and orientation tests. The intersection test ensures that there are no intersecting triangles existing in the surface mesh. The total number of intersecting triangles can be manually repaired by four basic options (edge flip, edge collapse, edge bisection and vortex translation). Upon successfully passing the intersection test, the orientation test was conducted for the identification and removal of any inconsistent

triangles. These inconsistent triangles may emerge after surface simplification and can result in a partial overlap of the materials bounded by the triangles. Edge flip, edge collapse, edge bisection and vortex translation were utilized to perform the orientation test. There are two prerequisites for the orientation test: a) the generated surface must be free of intersections, and b) the outer triangles of the generated surface must be assigned to the material's exterior. If these prerequisites are not met, then falsely reported orientation may cause serious errors in the generation of the tetrahedral grid necessary for numerical simulation.
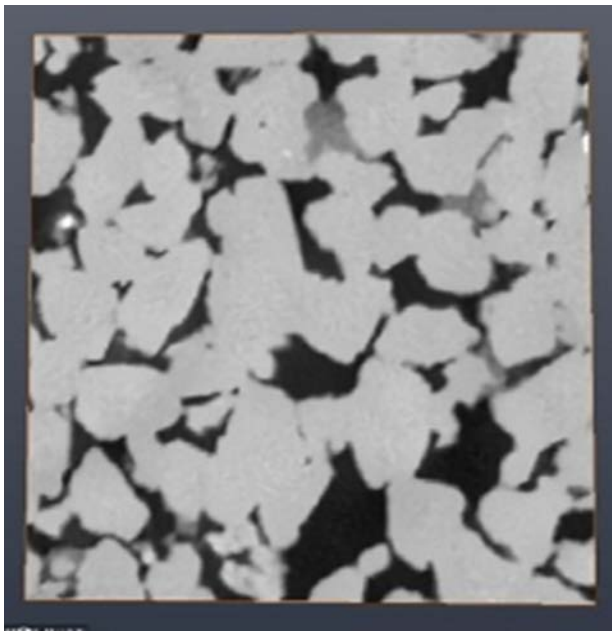
Figure 3.4: 2-Dimensional micro-CT scanned image of the Berea sandstone.
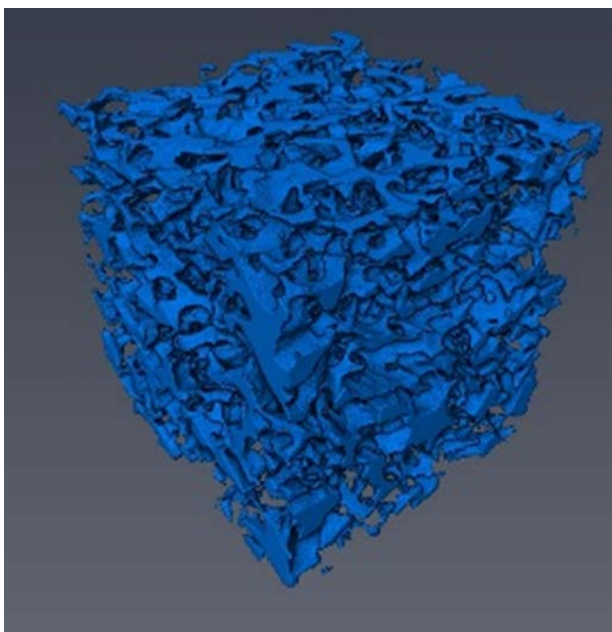
Figure 3.5 Segmented pore spaces of the Berea sandstone.
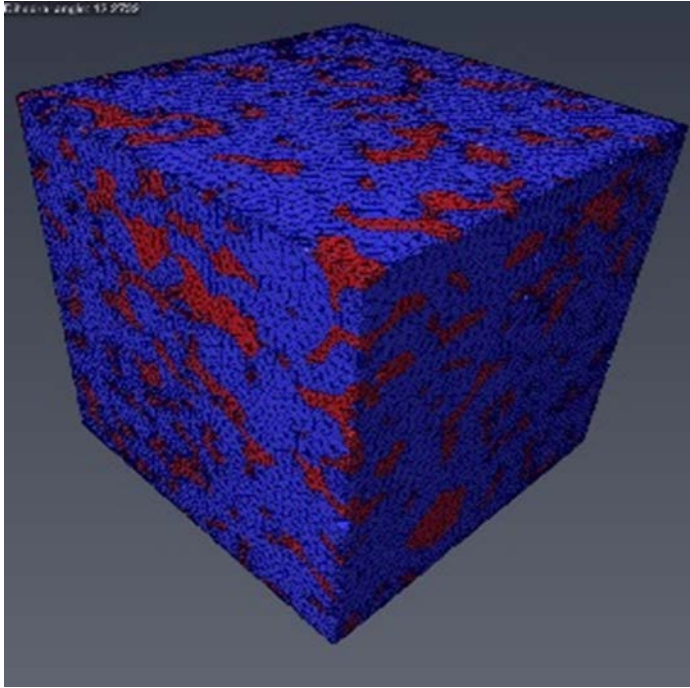
Figure 3.6: Surface mesh of the Berea sandstone processed using AVIZO software.

It is also important to check the aspect ratio, dihedral angle and tetra quality to generate a quality mesh, on which the simulation results are highly dependent. The aspect ratio refers to the ratio of the radii of the circumcircle and in-circle of each triangle. The largest aspect ratio should be below 10. The 'flip edges' tool in AVIZO may be used to improve the aspect ratio. *Dihedral angle* refers to the angle between each pair of adjacent triangles at their common edge. The smallest dihedral angle should be larger than 10 degrees. In the case of small dihedral angles, the 'edge flip' option may be utilized for further improvement. The tetra quality or the aspect ratio of a tetrahedron is defined as the ratio of the radii of the circumsphere and the inscribed sphere. The largest tetrahedral aspect ratio should be below 25. The 'vertex translation' and the 'edge flip' operations were utilized to manually repair large tetrahedron aspect ratios.

Upon converting the micro-CT scanned images into the surface mesh (in STL file format), the mesh was then imported to the commercial software ANSYS-ICEM-CFD to generate the volume mesh. The volume mesh of the whole pore space was generated initially. Since such disconnected void spaces do not contribute to permeability, all disconnected pore spaces were then truncated out of the mesh to improve flow analysis and save computational time. The process involved in the generation of the volume

mesh from the surface mesh (created from micro-CT images by AVIZO) using ANSYS ICEM CFD is illustrated in the flowchart shown in Figure 3.7.
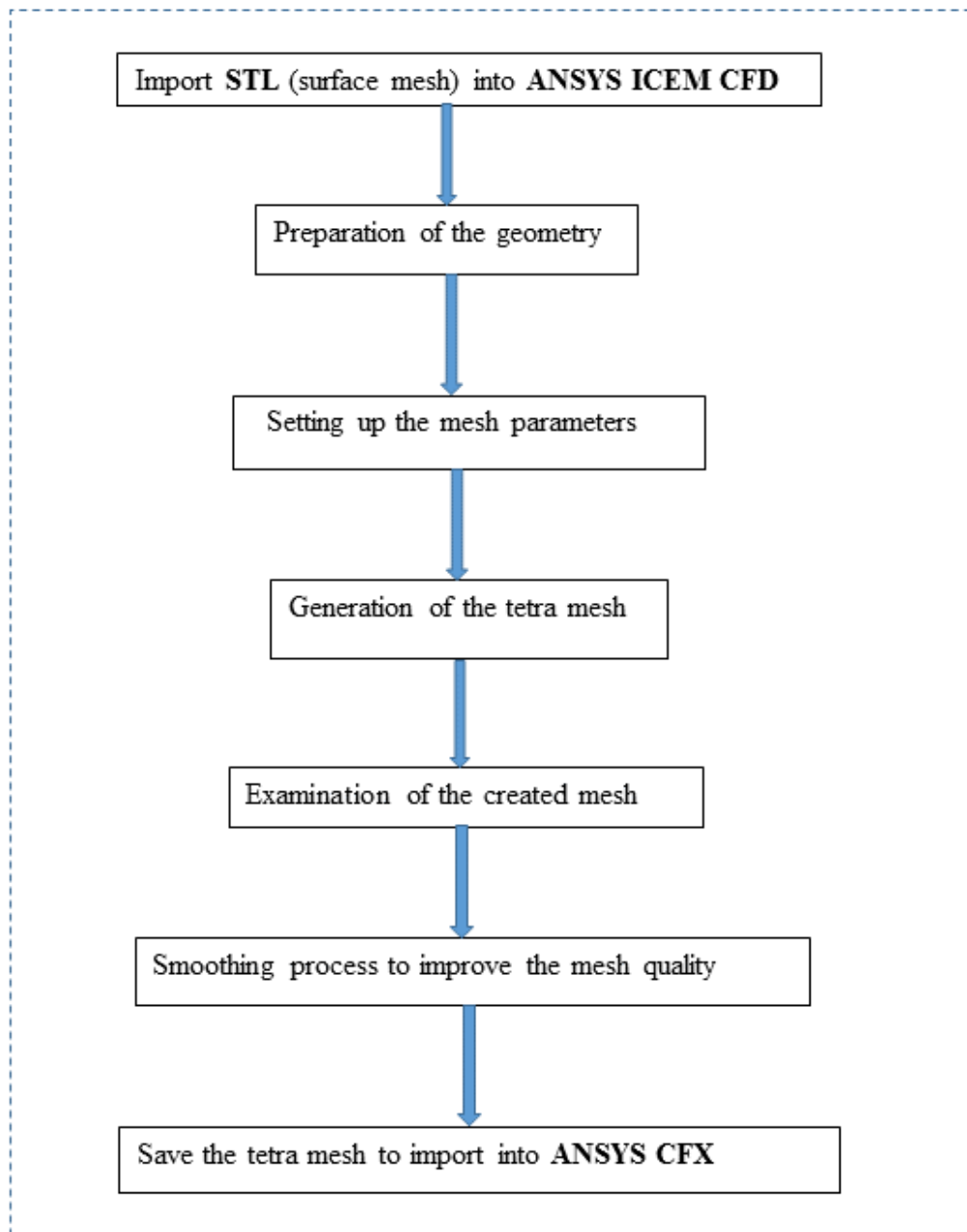
Figure 3.7: Flowchart showing the process of generating the volume mesh in ANSYS ICEM CFD.

The surface mesh imported from AVIZO to ANSYS-ICEM CFD has no definitive representation for boundary conditions for the surfaces. This needs to be processed by setting up various parameters to generate the volume mesh.

In ANSYS ICEMCFD, the 'Global mesh setup' option administers various general and definitive meshing specifications to create the necessary atmosphere to generate the required volume mesh. At the beginning, the mesh size is defined. Then, the ANSYS ICEM CFD Tetra Mesher creates the volume mesh by filling up the surface mesh with tetrahedral elements. In this research work, the 'Octree approach' was used (which is the best choice for complex geometry like the pore spaces of a rock sample), which is capable of providing good quality tetrahedral meshes. A flow diagram illustrating the various steps followed for the generation of the tetra mesh is shown in Figure 3.8.
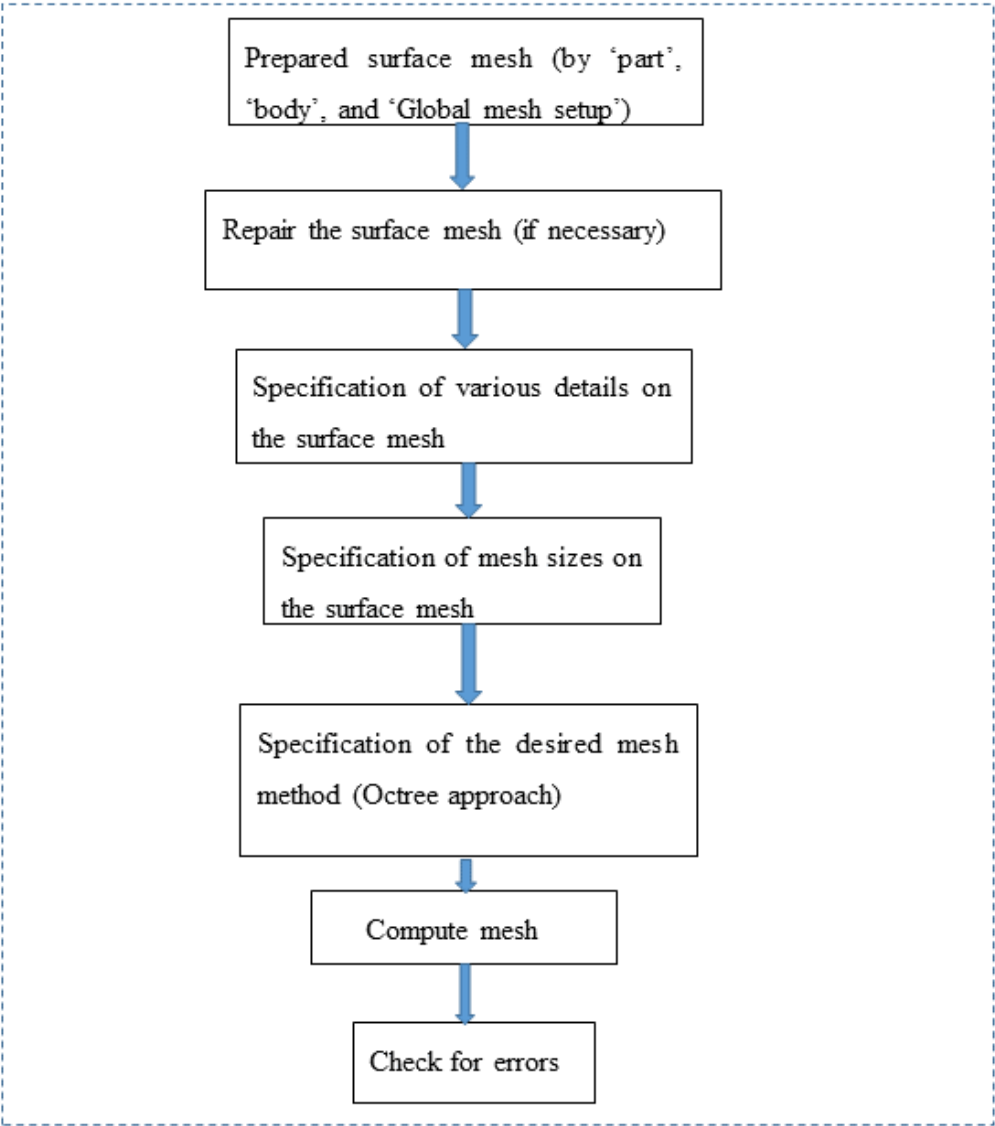
Figure 3.8: Flow diagram illustrating the various steps followed to generate the tetra mesh (ANSYS ICEMCFD User Manual, 2012).

The computed mesh may undergo a smoothing process again if necessary. After the smoothing process, a quality histogram is generated automatically. Then, it is ready to check for errors.

Before checking errors, the generated mesh was examined by the 'cut plane' approach. With the help of this approach, the generated mesh can be diagnosed in the x, y, and z directions. Thus, further smoothing requirements can be determined through this examination step. If the mesh is not properly generated, then further smoothing can be applied without adjusting the tetrahedrals.

The 'check mesh' editing tool in ANSYS ICEMCFD facilitates the necessary procedures to check and fix problems in the generated mesh (ANSYS ICEMCFD User Manual, 2012).

Possible sources of error are:
1. Inappropriate usage of meshing methods
2. Inappropriate resolution or distribution while creating the surface mesh
3. High skewness
4. Large aspect ratio
5. Incorrect mesh orientation
6. Uncovered faces
7. Missing internal faces.

Consequences of possible errors:
1. Crashed mesh.
2. Incorrect solution (volume mesh)
3. Unwanted or hanging elements
4. Unwanted holes or gaps
5. Failure to write or read the generated mesh into ANSYS CFX
6. Solution fails to converge or run.

A number of manual and automatic options in this specific tool can solve the above issues. A histogram can show the desired results. Moreover, this tool can improve the mesh quality. Quality checking is important because a poor quality mesh can result in

inaccurate solutions or very slow convergence. The quality checking process is described in Figure 3.9.
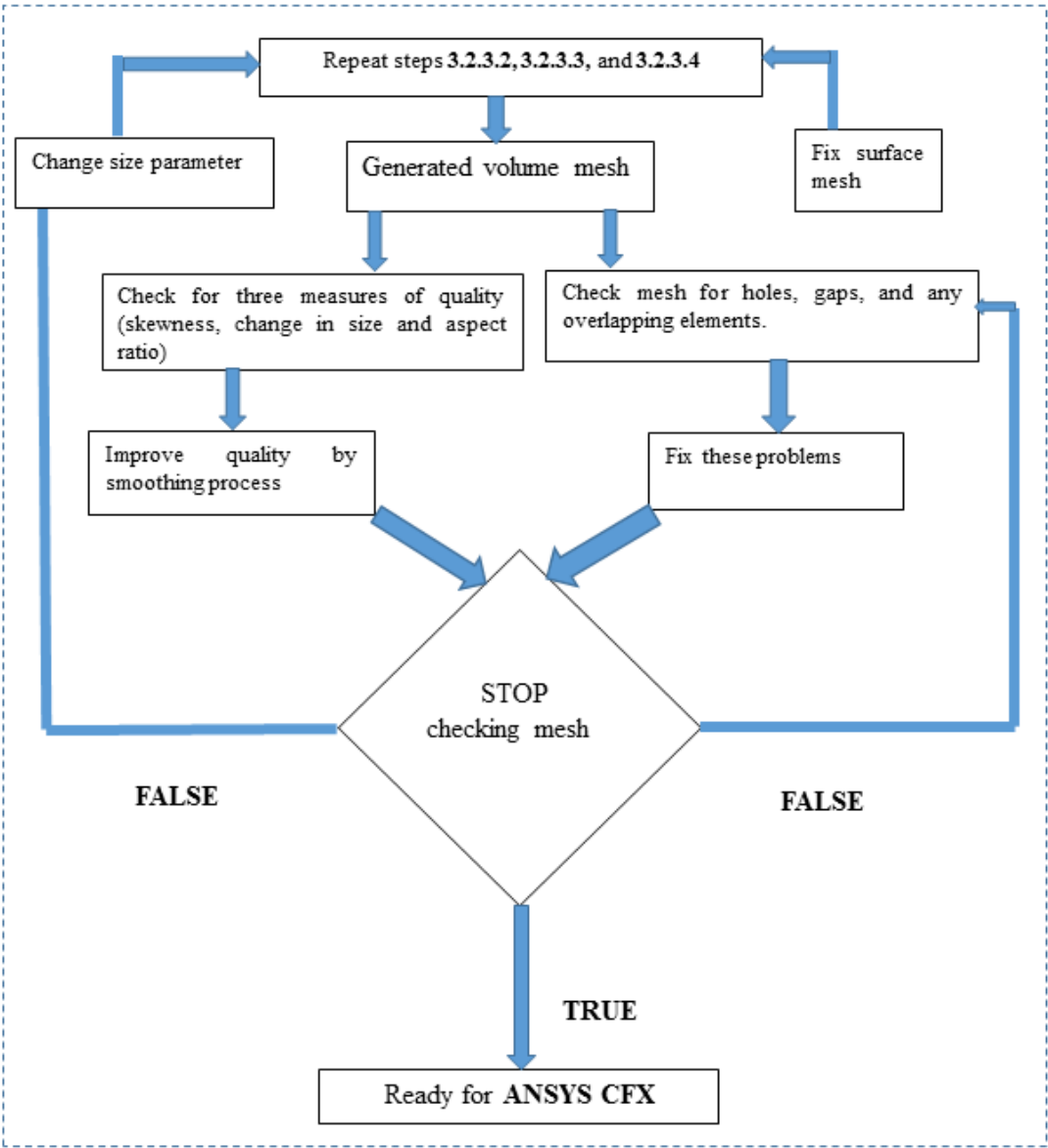
Figure 3.9: Flowchart illustrating the process of improving mesh quality (ANSYS ICEMCFD User Manual, 2012).

3.3. *Numerical Simulation workflow in ANSYS CFX*

ANSYS-CFX is a popular commercial 3D computational fluid dynamics (CFD)-based multipurpose simulator. It uses an element-based finite volume method to discretise the mass, momentum and transport equations. In this method, convergence can be achieved with a lower number of iterations than other commercial codes. The

workflow used to estimate various parameters by ANSYS CFX is shown in Figure 3.10.


```
┌─────────────────────────────────────────┐
│   Volume mesh from ANSYS ICEM CFD        │
└─────────────────────────────────────────┘
            │
┌─────────────────────────┐
│     ANSYS CFX-Pre       │
└─────────────────────────┘
            │
┌─────────────────────────┐
│    ANSYS CFX-Solver     │
│   Solve transient flows │
└─────────────────────────┘
            │
┌─────────────────────────────────────────────────────┐
│ Fluid saturation and pressure values are recorded at │
│ every simulation second (from the beginning to the end) │
└─────────────────────────────────────────────────────┘
            │
         ◇ After a certain simulation time
           period, the system reached steady-
           state condition,
                    NO / YES
┌─────────────────────────┐
│  The simulation has stopped. │
└─────────────────────────┘
            │
┌─────────────────────────────────────────┐
│  Post-processing with ANSYS CFD-Post     │
└─────────────────────────────────────────┘
```
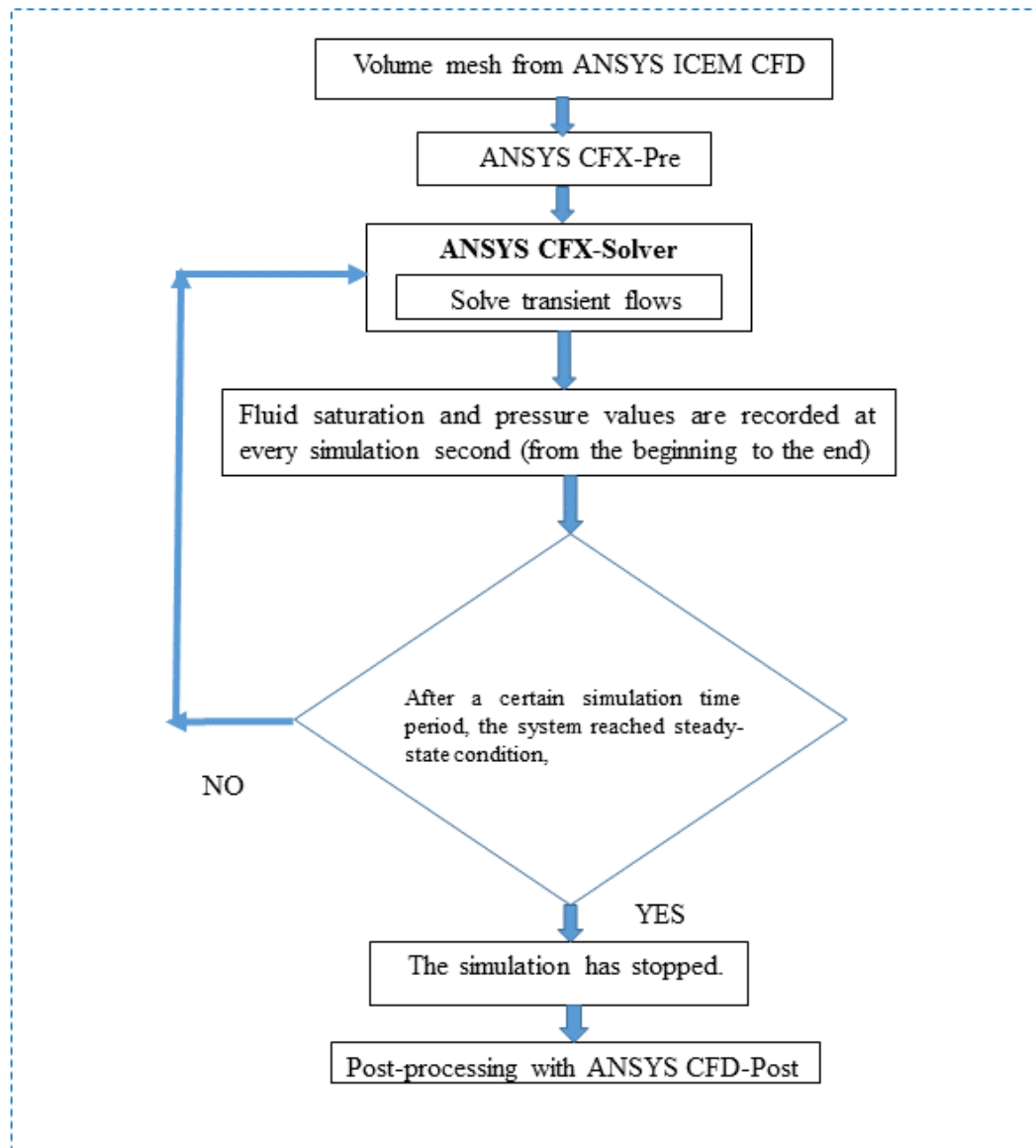
Figure 3.10: Flowchart for numerical simulation on the generated volume mesh by ANSYS CFX (ANSYS CFX-Solver Modelling Guide, 2009).

A refined volume mesh was used in this study to run transient simulations through ANSYS CFX. Before running with transient behaviour, steady-state behaviour was observed for single-phase (brine) flow. Moreover, isothermal flow was considered. The transient flow was investigated (with buoyancy effects) using the full buoyancy model explained earlier in Section 3.1 (Equations 3.5 and 3.6).

Initially, the numerical model was considered to be saturated with brine before the scCO$_2$ injection (drainage) process. At the beginning of the drainage process, scCO$_2$ was injected and fluid saturation and pressure were monitored. The scCO$_2$ injection was ceased when the pressure appeared to be constant.

The boundary conditions used were a combination of various properties or conditions which act on the surfaces of domains. For the drainage process, the boundary conditions at the inlet point were specified as the injection velocity for the non-wetting phase (scCO$_2$), and zero velocity for the wetting phase (brine). The inlet velocity of scCO$_2$ was considered based on different capillary numbers. For imbibition, the boundary conditions at the inlet were considered to be the reverse of the drainage process. The boundary conditions specific to certain samples are discussed in detail in subsequent chapters.

In the numerical model, the pressure boundary condition was specified at the outlet with a relative pressure set to zero. So, the pressure predicted at the inlet is equal to the differential pressure or pressure drop between the inlet and outlet of the volume mesh.

All the other faces of the numerical models were assumed to be impermeable. This condition was achieved by applying no-slip wall boundary conditions. The convergence criterion was set as 10^{-5}. All simulations were run with a time-step size of 0.01 s based on Courant number. In ANSYS CFX, the Courant number (N_c) is used to find the appropriate time step for a given mesh (ANSYS CFX-Solver Modelling Guide, 2009. The Courant number describes the stability or variation of the flow around a control volume; and is defined as $N_c = u \frac{\Delta t}{\Delta x}$, where u is fluid velocity; Δt is the time step size; and Δx is the length of smallest mesh element.

4. Chapter 4: Numerical simulation for scCO$_2$-brine distribution and prediction of capillary pressure and relative permeability

In this chapter, the scCO$_2$-brine distribution in the pore spaces of the Ottawa F42 Sand Pack and prediction of its relative permeability and capillary pressure are presented. These are discussed based on numerical simulation studies using the commercial computational fluid dynamics (CFD)-based numerical simulator ANSYS CFX. This chapter is based on the authors' paper (Jahan et al., 2017).

4. Background

Laboratory-based two-phase flow experiments involve the use of sets of equipment at certain operating conditions to create conditions similar to those found in reservoirs. Whereas in numerical experiments, CFD-based simulation involves modelling the problem numerically according to nearly exact reservoir conditions to analyse, predict and better understand the mechanisms involved. In this work, a CFD-based numerical approach was adopted to investigate scCO$_2$ capillary pressure in a scCO$_2$-brine system in a geological storage system. The particular study considers the Ottawa F42 Sand Pack, which is often used for geological storage for carbon capture and sequestration (CCS) projects. The numerical approach attempts to predict scCO$_2$ capillary pressure within micro-pores of the Ottawa F42 Sand Pack in a scCO$_2$-brine system. As experimental or numerical results related to scCO$_2$-brine systems with which to validate the estimated scCO$_2$ capillary pressure in the Ottawa F42 Sand Pack are not available in the literature, a number of numerical simulations (for drainage and imbibition processes) were carried out first. These were validated by comparing the developed numerical model with available experimental and numerical results, assuming that the numerical model can be analogously used to analyse two-phase flow behaviour. The validated numerical model was then used to model the scCO$_2$-brine system.

4.1 Numerical Modelling and Validation

4.1.1. Numerical Model

As discussed, due to the unavailability of data for $scCO_2$-brine systems, the numerical model was validated against known results for oil-brine systems in order to justify whether it can be analogously used to analyse $scCO_2$-brine flow. In this respect, ANSYS CFX, a module of the CFD-based numerical simulator ANSYS, was used to investigate the fluid (oil and brine) relative permeability and oil capillary pressure within the oil-brine system. A set of numerical simulations (for drainage and imbibition processes) were conducted on the micro-pores of the Ottawa F42 Sand Pack. A description and simulation results, including validation of the model, are discussed below. The capillary pressure and relative permeability for the drainage and imbibition processes were predicted using results obtained from numerical simulation studies and the analytical models presented in Section 4.1.2. The model was validated through comparison with existing studies, see Section 4.1.3.

4.1.2. Model description

The numerical model was created from micro-CT images of an Ottawa F42 Sand Pack sample. The micro-CT images were processed using the Avizo software (Thermo Scientific™). Avizo helps to conduct visualization, processing and quantification of pore spaces of the geological rock samples. It is used to separate the network of pore spaces and capture the actual network of pore spaces in the Ottawa F42 Sand Pack sample, enabling generation of a 3D surface mesh of the sample. The image size of this sample was $300 \times 300 \times 300$ voxels, with porosity and permeability ranges of 34.1–36.7% and 38–46 Darcy (Iglauer & Muggeridge, 2013). The generated surface mesh was then converted into a volume mesh using the ANSYS ICEM CFD processor, as shown in Figure 4.1(a-b). The CFD-based simulator ANSYS-CFX was used to simulate drainage and imbibition processes. Further details of this process are comprehensively discussed in Chapter 3.

Figure 4.1(a) shows a 3D view of the volume mesh of the Ottawa F42 Sand Pack sample. The details of this mesh are shown in 2D in Figure 4.2 (b), with an enlarged view in Figure 4.1(c).
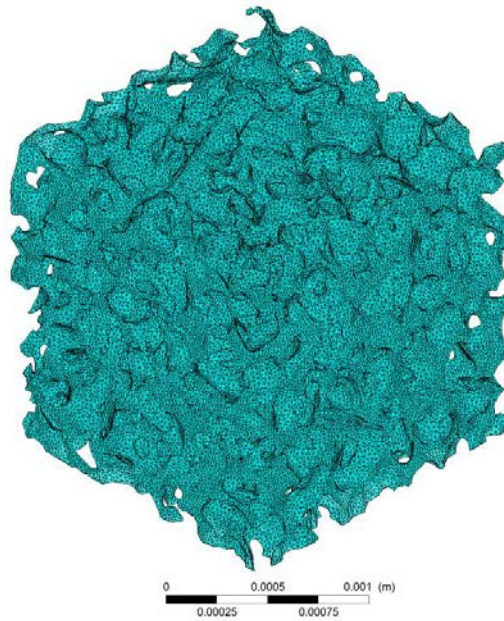
(a)
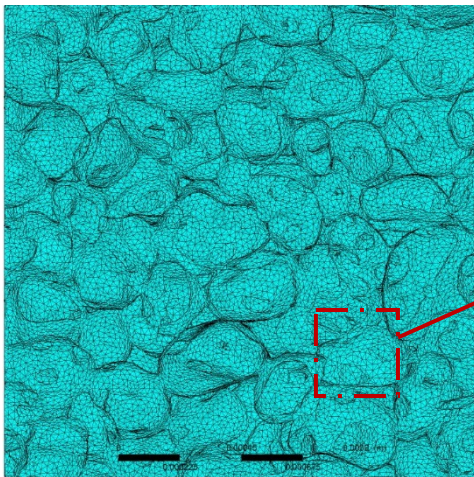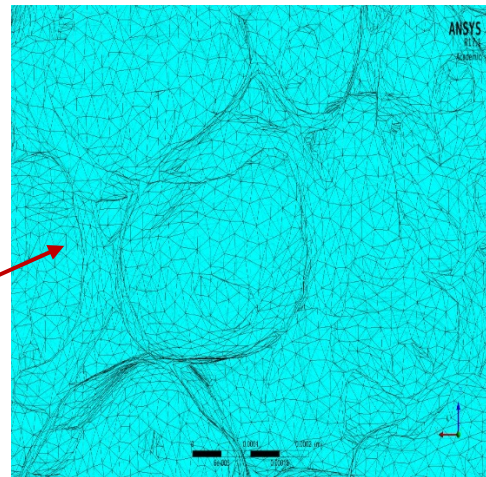
(b)   **(c)**

Figure 4.1: Generated volume mesh of Ottawa F42 Sand Pack: (a) 3D view, (b) 2D view with enlargement in (c).

The capillary number plays an important role in the distribution and uniformity of fluid phases in porous media. For instance, a capillary number greater than 10^{-7} can result in a uniform distribution of brine and $scCO_2$ (Blunt, 2001). Capillary numbers greater than 10^{-6} can affect the shape of the fluid relative permeability curves (Krevor et al., 2012). In order to have a uniform two-phase fluid distribution and to incorporate the effect of capillary and other forces in the porous medium, four different capillary numbers (1.5×10^{-5}, 2.0×10^{-5}, 1.0×10^{-3}, and 1.2×10^{-3}) were considered in this study.

4.1.2.1.   Boundary conditions and inlet fluid velocity

In the simulation model, for pressure boundary conditions, the pressure at the outlet was set to zero so that the direct pressure predicted at the inlet could be considered as the differential pressure, or pressure drop, between the inlet and outlet of the mesh. All the other faces of the model were assumed to be impermeable, which was achieved by applying no-slip wall boundary conditions. In fluid dynamics, the 'no-slip condition' for viscous fluids expresses a solid boundary where the fluids have zero velocity relative to the boundary. In this research work, cubic-shaped samples (models) are considered. For cubic-shaped samples, fluid velocities at all the other 4 (four) faces (except the inlet and outlet) are assumed to be zero, which was achieved by applying no-slip wall boundary conditions. As the velocities showed zero values, it is assumed that no fluid is moving towards the outside of the model through the other faces except the inlet and outlet. According to ANSYS CFX-Solver Modelling Guide (2009), a wall represents an impenetrable boundary to fluid flow. In addition, all simulations were run with a time-step size of 0.01 s in order to reduce the computational time for faster convergence. Initially, the numerical model was considered to be saturated with brine before the injection (drainage process) of other fluid (e.g. $scCO_2$).

For the drainage process, the inlet velocity of $scCO_2$ at the inlet was set to zero. The brine velocity was calculated from the corresponding capillary number. Similarly, during the imbibition process, the inlet velocity of brine was set to zero, while that for $scCO_2$, it was calculated from the corresponding capillary number (using Equation 2.1).

4.1.3. Analytical model for the prediction of capillary pressure and relative permeability for drainage and imbibition processes

4.1.3.1.   Prediction of Relative Permeability

The brine and oil relative permeabilities were calculated using the widely-used Corey relative permeability correlation (Corey, 1954; Li et al., 2006). Based on this model, the relative permeability in the case of drainage was calculated using Equations 4.1-4.2. Observed fluid saturation values were used in these equations to predict fluid relative permeability values.

$$K_{rw} = (S_w^*)^4 \tag{4.1}$$

$$K_{nrw} = (1 - S_w^*)^2 [1 - (S_w^*)^2] \tag{4.2}$$

Where,

$S_w^* =$ Normalized brine residual saturation $= \frac{S_w - S_{wc}}{1 - S_{wc}}$;

$S_w =$ Brine saturation at various times;

$S_{wc} =$ Connate brine saturation, which is predicted from numerical simulation;

$K_{rw} =$ Brine relative permeability;

$K_{nrw} =$ Oil relative permeability.

Prediction of Imbibition Relative Permeability

The brine and oil relative permeability values for imbibition processes were predicted (Land et al., 1968) as below. In the Equation 4.3, P_c values are considered from the laboratory-based experimental data published in the literature as presented by Iglauer and Muggeridge (2013). With the help of the Equation 4.3, K_{or} is derived and used in the Equation 4.8 to estimate P_c. This numerically obtained value of P_c is compared with the values from published research works. Results showed good agreement with the published literatures. Thus, no further iteration process is required.

A. Prediction of oil relative permeability

Oil relative permeability can be predicted with the help of the following equation:

$$K_{or} = K_r^o \, S_{0,F}^{*2} \left[1 - \left(1 - S_{o,F}^* \right)^{\frac{2+\lambda}{\lambda}} \right] \tag{4.3}$$

Where K_r^o is the oil relative permeability at connate brine saturation, which can be calculated using the following correlation (Standing, 1975):

$$K_r^o = 1.31 - 2.62 \, S_{wc} + 1.1(S_{wc})^2$$

Where,

$S_{o,F}^* =$ Normalized free oil saturation at various times;

$\lambda =$ pore-size distribution factor, which is the slope of a plot of log $1/P_c$ vs log S_w^*.

B. Prediction of brine relative permeability:

Brine relative permeability can be estimated by these correlations (Land et al., 1968):

$$K_{rw} = S_w^{*2} \left[(S_w^* + S_{ot}^*)^2 - \frac{2}{C^2} \left(\ln \frac{1-\{(1-S_{or,\,max}^*)(S_w^*+S_{ot}^*)\}}{1-\{S_{wi}^*(1-S_{or,\,max}^*)\}} + \frac{1}{1-\{(1-S_{or,\,max}^*)(S_w^*+S_{ot}^*)\}} \right. \right.$$

$$\left. \left. - \frac{1}{1-\{S_{wi}^*(1-S_{or,\,max}^*)\}} \right) \right] \tag{4.4}$$

For this equation, the normalized trapped oil saturation S_{ot}^* is estimated first. Then, other parameters were estimated and inserted in Equation (4.4) to determine K_{rw}.

B.1 Normalized trapped oil saturation (S_{ot}^*) determination

To determine normalized trapped oil saturation (S_{ot}^*), the correlations (Standing, 1975) given by Equations (4.5) and (4.6) were used:

$$S_{o,F}^* = 0.5 \left[(S_o^* - S_{or}^*) + \sqrt{\{(S_o^* - S_{or}^*)^2 + \tfrac{4}{C} (S_o^* - S_{or}^*)\}} \right] \tag{4.5}$$

$$S_{ot}^* = S_0^* - S_{o,F}^* \tag{4.6}$$

The correlation for Land's trapping coefficient, C, is given by Equation (4.7):

$$C = \frac{1}{S_{or}^*} - \frac{1}{S_{ot}^*} \tag{4.7}$$

Where,

$S_{o,F}^*$ = Normalized free oil saturation as a function of simulation time;

S_{ot}^* = Normalized trapped oil saturation as a function of simulation time;

S_{or}^* = Normalized oil residual saturation $= \frac{S_{or}}{1-S_{wc}}$;

S_{oi}^* = Normalized oil initial saturation $= \frac{S_{oi}}{1-S_{wc}}$;

S_o^* = Normalized oil saturation as a function of simulation time;

C = Land trapping coefficient.

S_{or}^*, S_o^*, and $S_{o,F}^*$ were determined using Equation (4.5); and the numerical simulation results for drainage and imbibition processes after the system is reached a steady-state condition. A steady state is assumed to be established when the pressure drop appears to be constant. The corresponding initial and residual fluid saturations (S_{wi}, S_{oi} and S_{or}) are then directly obtained from the simulation. Upon calculation of S_o^* and $S_{o,F}^*$, the normalized trapped oil saturation with time, $S_{ot}*$, is calculated using Equations 4.6-4.7. Using analytical Equations 4.1-4.7 and data from the simulation, the relative permeability for both imbibition and drainage processes were calculated.

The various saturations described above were obtained by numerical simulation for the Ottawa F42 Sand Pack (oil-brine system), and are summarized in Table 4.1.

Table 4.1: Various saturation values obtained from simulation.

Various saturations	Obtained value from simulation
Connate brine saturation, S_{wc}	0.16
Maximum residual oil saturation, $S_{or,max}$	0.77
Initial brine saturation, S_{wi}	0.16
Initial oil saturation, S_{oi}	0.84
Residual oil saturation, S_{or}	0.05

In this Table 4.1, a value of initial water (brine) saturation is provided for a specific simulation time (for example purpose). For other values of simulation times, different initial water (brine) and corresponding oil saturation values were used to predict relative permeability and capillary pressure values. According to the ANSYS CFX simulator, the summation of water (brine) and oil saturation must be equal to 1(one). So, there are different values of fluid (oil and brine) saturation at different simulation times.

4.1.3.2. Capillary pressure

The capillary pressure was estimated using Equation (4.8), as follows (Babchin et al., 2014):

$$P_c = \sigma cos\theta . S_v S_o^* + A \tag{4.8}$$

Where,

σ = Surface tension, N/m;

θ= contact angle in degrees;

S_v = Specific surface area =. $\dfrac{\varnothing^{0.5}}{K} . \dfrac{(K_{nw}^{0.5}+K_w^{0.5})}{(K_{nw}+K_w)^{0.5}}$ (Babchin et al., 2014);

S_o^* = Normalized oil saturation as a function of time;

$\varnothing$ = Porosity;

K= Absolute permeability, m^2;

K_{nw} = Non-wetting phase relative permeability;

K_w = Wetting phase relative permeability;

A = Constant equal to the capillary pressure at the residual saturation point for a drainage process and zero for an imbibition process.

The process for calculating the relative permeability of different phases is described in the flow diagrams shown in Figures 4.2 (a-d).
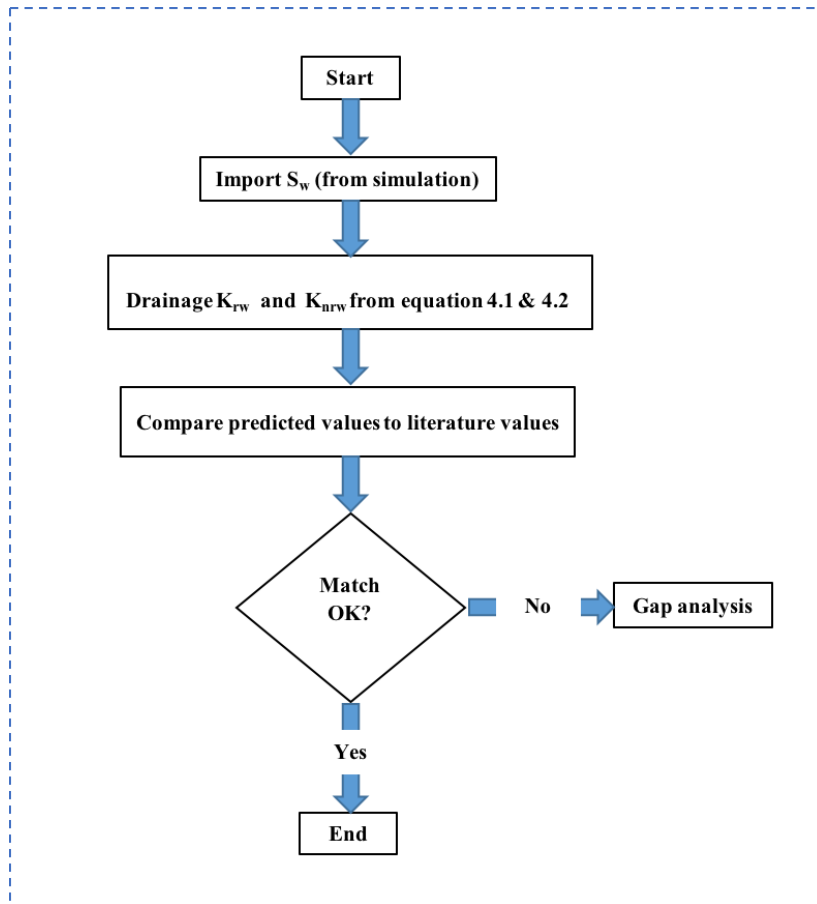
Figure 4.2(a): Flowchart for drainage relative permeability prediction.
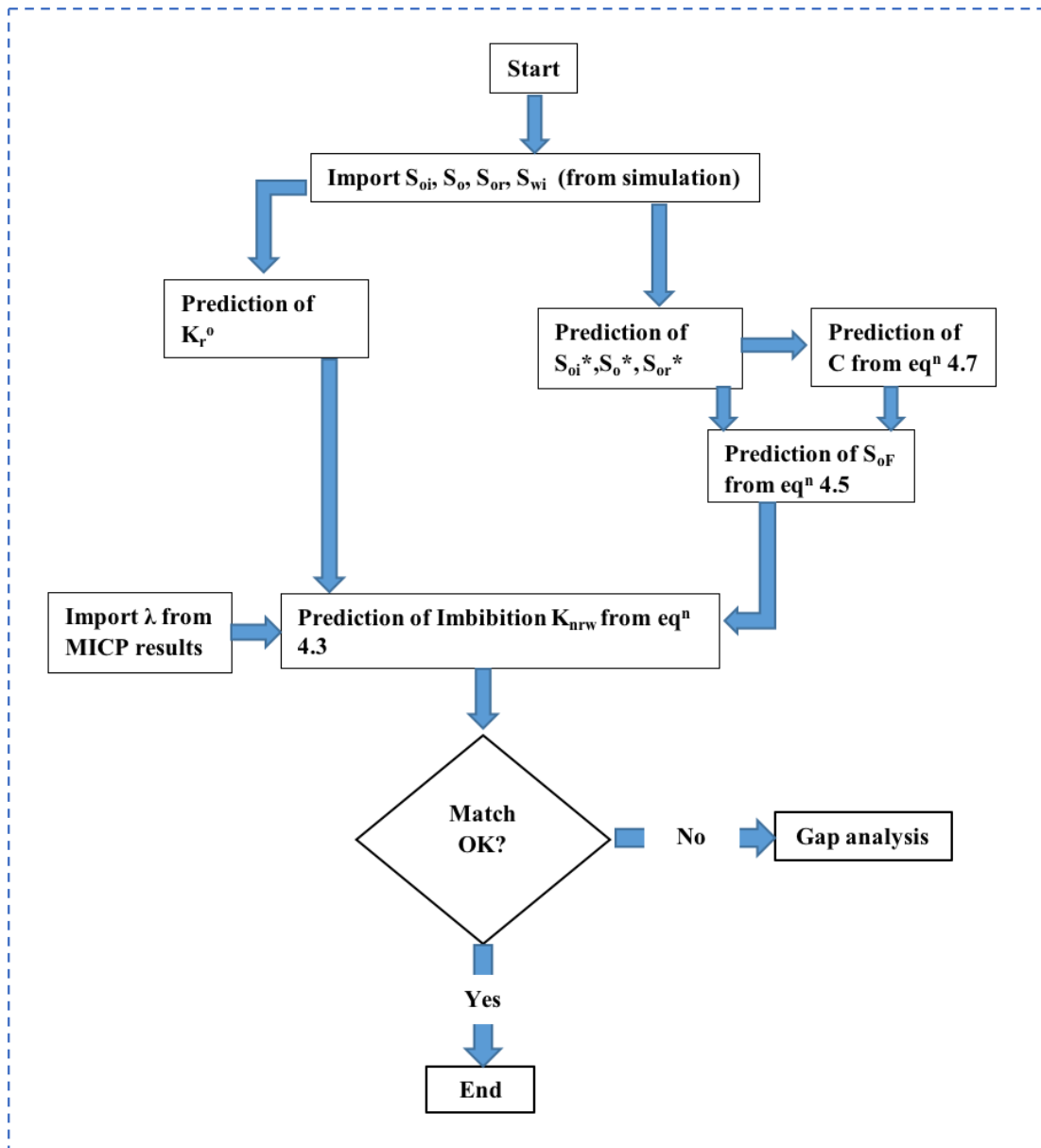
Figure 4.2(b): Flowchart for imbibition non-wetting phase relative permeability prediction.
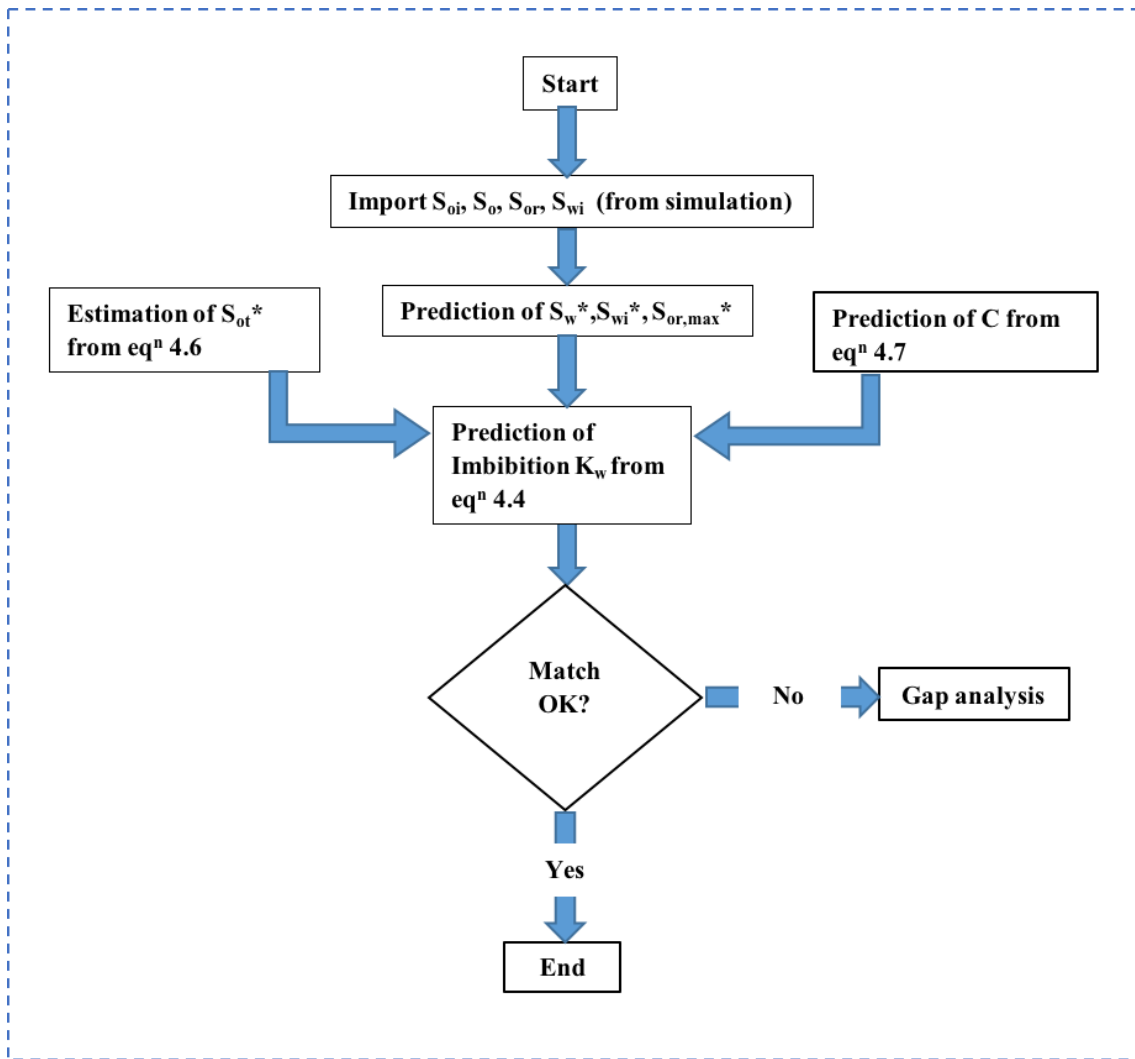
Figure 4.2(c): Flowchart for imbibition wetting phase relative permeability prediction.
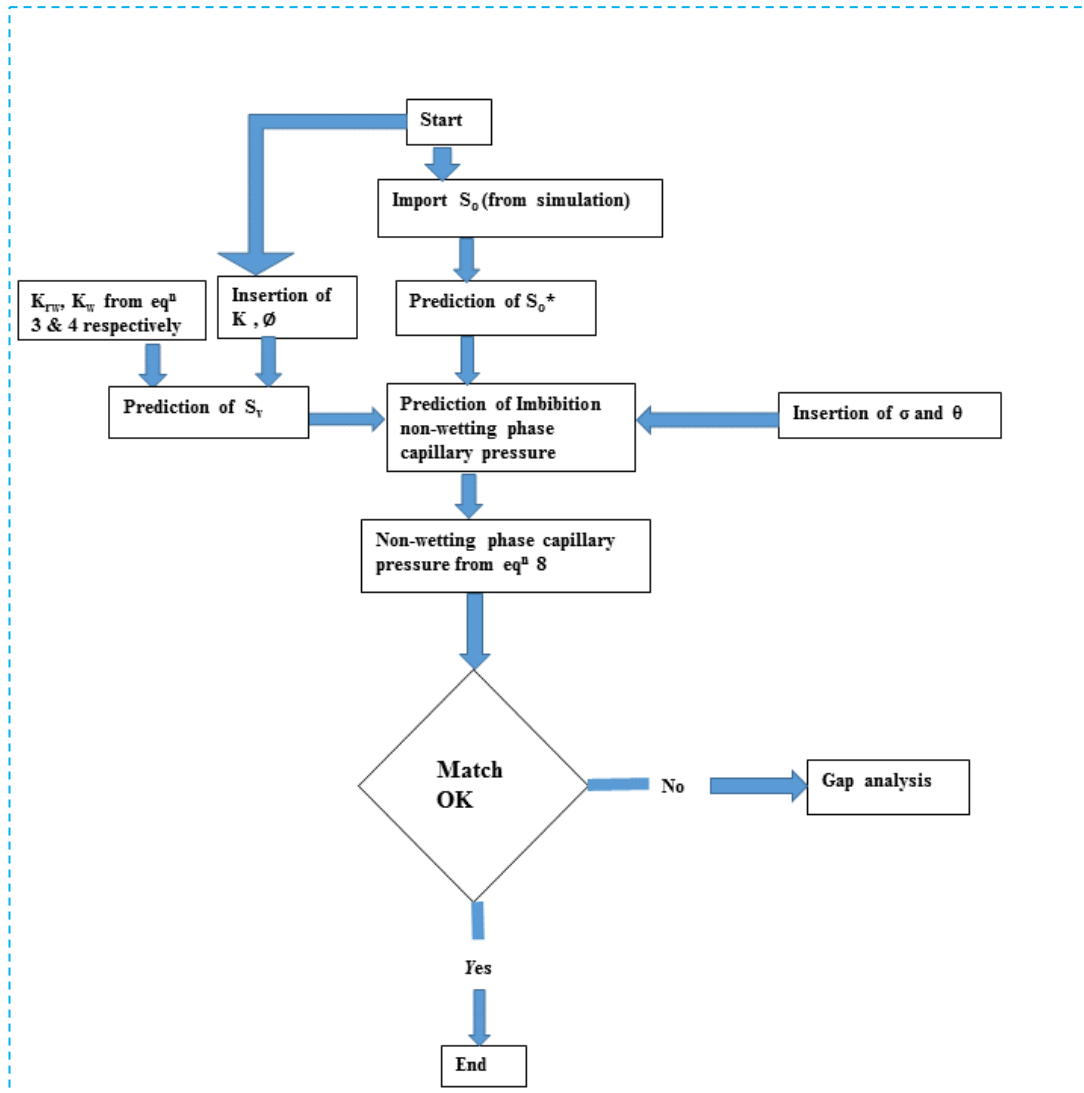
Figure 4.2(d): Flowchart for non-wetting phase capillary pressure prediction.

4.1.4. Comparative study and model validation

Due to the lack of the experimental or numerical data for $scCO_2$-brine systems, an oil-brine system was considered to validate the numerical work, in combination with the analytical method presented in Section 4.1.2, based on the assumption that the developed numerical model can be analogously used for the $scCO_2$-brine system in the Ottawa F42 Sand Pack.

4.1.4.1.   Simulation of the oil-brine system

The numerical model for the Ottawa F42 Sand Pack, as described earlier in Section 4.1.1, was used to predict fluid relative permeability for both drainage and imbibition processes. The inlet velocity, contact angle and capillary number used for simulation

of the drainage process were 0.026 m/s, θ = 5 and 2.5 × 10^{-4}, respectively. For the simulation of the imbibition process, an inlet velocity of 0.03 m/s, contact angle θ = 45° and capillary number of 2.5 × 10^{-4} were used. These inlet fluid velocities were calculated from the corresponding capillary numbers (i.e. 2.5 × 10^{-4} and 7.0 × 10^{-4}) using Equation 2.1, as presented in Chapter 2. After completion of the drainage and imbibition processes, the fluid saturation and pressure drop were observed and quantified accordingly from the simulation. Then, the fluid relative permeability was predicted using the analytical models presented in Section 4.2.3. The simulation results were compared with similar works for validation.

4.1.4.2.   Formation and fluid properties:

Oil (n-octane) and brine were considered as the two fluids used in the numerical simulation for validation purposes. The oil viscosity and oil-brine surface tension considered were 5.08 × 10^{-4} Pa.s and 51.64 × 10^{-3} N/m, respectively (Pentland et al., 2011).

The Ottawa F42 Sand Pack sample appeared to be strongly water-wet and had a composition of more than 99.8 wt% quartz (Iglauer & Muggeridge, 2013). Also, its porosity and permeability were considered to be 0.354 and 42 D, respectively (Iglauer & Muggeridge, 2013).

4.1.5 Comparison of predictions

The fluid relative permeability for Ottawa F42 Sand Pack was estimated using simulations and the analytical model described in Section 4.1.2 and was compared with similar published work carried out by Talabi et al. (2008) for the same F42 Sand Pack. The F42 Sand Pack used by Talabi et al. (2008) appeared to be similar (same porosity and permeability) to that of the Ottawa F42 Sand Pack used in the present study and, hence, these data were used in the oil-brine simulations.
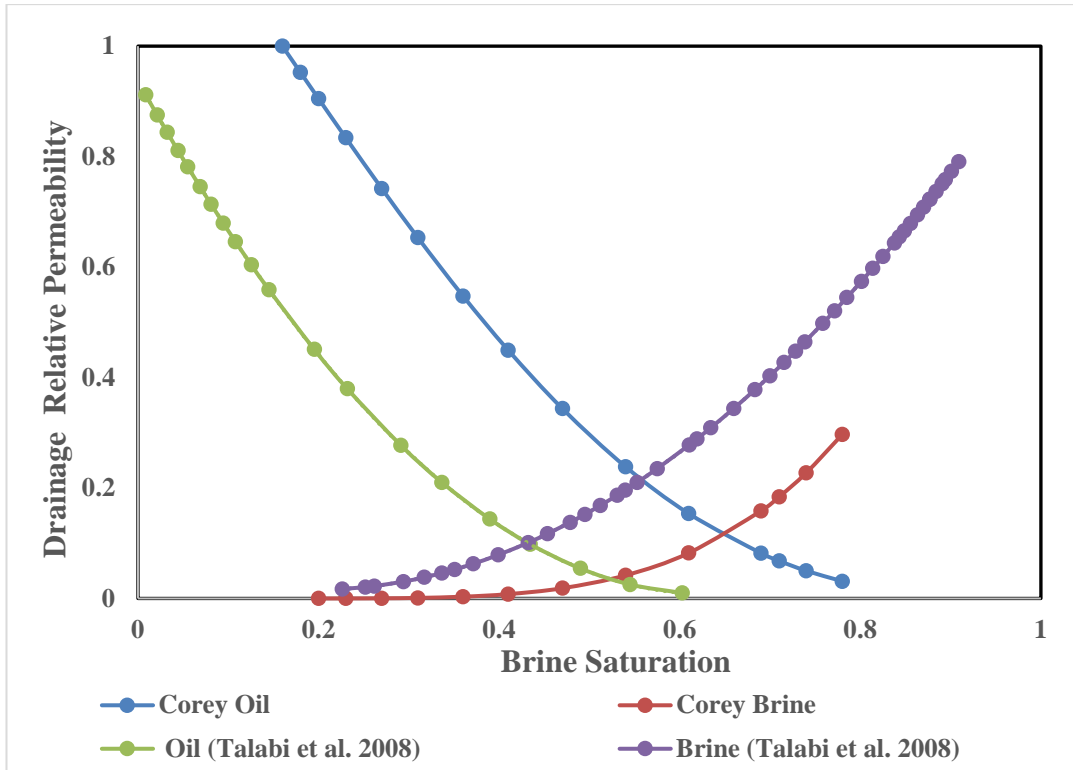
Figure 4.3 (a)
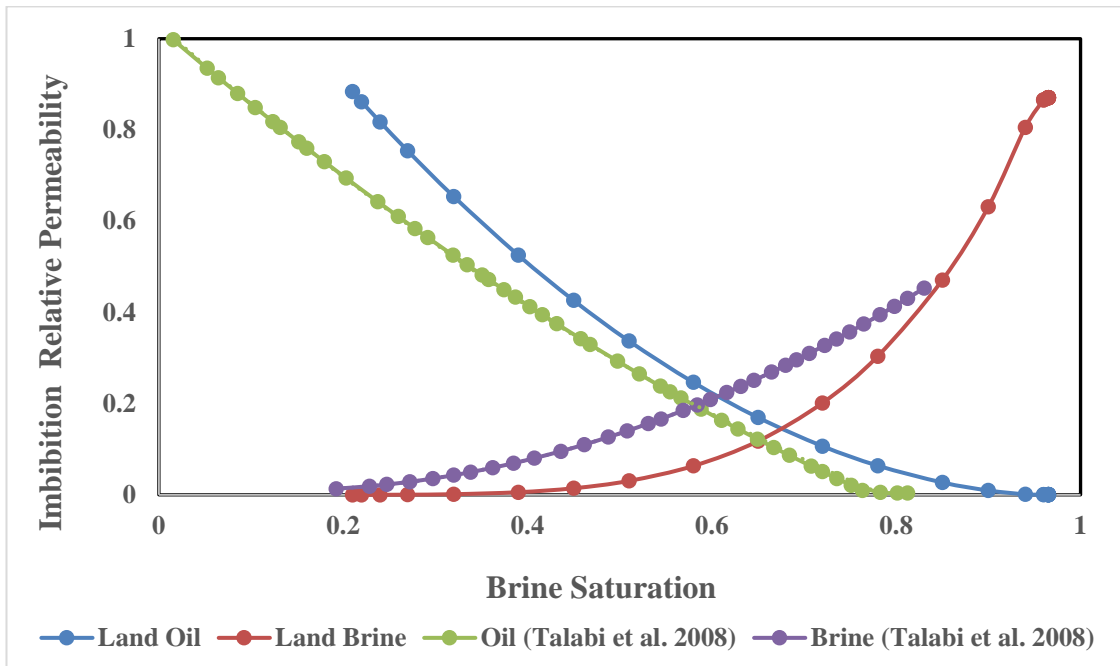
Figure 4.3(b)

Figure 4.3: Comparison of oil and brine relative permeability as functions of brine saturation for Ottowa F42 Sand Pack for the drainage process (a), and imbibition process (b).

It can be observed from Figure 4.3(a-b) that Talabi et al.'s (2008) data appears to under-predict the brine relative permeability and over-predict the oil relative permeability as compared with the results obtained by the current study (based on numerical simulation and analytical models). However, the imbibition contact angle for the Ottawa F42 Sand Pack was 45° in this work. However, a range of imbibition contact angles (55–65°) was used in the work of Talabi et al. (2008). The exact value of drainage contact angle was not available in Talabi et al. (2008). Thus, the oil relative permeability for the Ottawa F42 Sand Pack (drainage and imbibition) is predicted to be higher than that of F42 Sand Pack, which results in less oil trapping. However, the results from the current study follow the same trend as that presented by Talabi et al. (2008).

4.2. *Simulation of scCO₂-brine system and visualisation of CO₂ and brine distribution*

After the comparative study of the oil-brine system, the proposed numerical model was used to simulate a scCO$_2$-brine system. In this regard, inlet fluid velocities were calculated from capillary numbers (as before for the oil-brine system). Details of capillary numbers and boundary conditions followed by discussion on numerical process are elaborated below. The discussion of scCO$_2$-brine visualization patterns at different conditions are also presented.

Selection of capillary numbers

According to Blunt (2001), capillary numbers greater than 10^{-7} are responsible for flow that causes a uniform distribution of brine and supercritical CO$_2$. In a two-phase flow system, capillary numbers greater than 10^{-6} can pose affect the shape of the fluid relative permeability curves (Krevor et al., 2012). To achieve a uniform two-phase fluid distribution and to incorporate the effect of capillary and other forces in the porous medium, four different capillary numbers (1.5×10^{-5}, and 2.0×10^{-5}, 1.0×10^{-3}, 1.2×10^{-3}) were considered in various drainage and imbibition processes for the scCO$_2$-brine system.

Boundary conditions

In the simulation model, for pressure boundary conditions, the pressure at the outlet was set to zero. So, the direct pressure predicted at the inlet can be considered as the

differential pressure or pressure drop between the inlet and outlet of the model. All the other faces of the Ottawa F42 Sand Pack model were assumed to be impermeable, which was achieved by applying no-slip wall boundary conditions. In addition, all simulations were run with a time-step size of 0.01 s in order to reduce computation time for faster convergence. Initially, the numerical model was considered to be saturated with brine before the $scCO_2$ injection (drainage) process commenced.

For the drainage process, the injection rate at the inlet was set to zero for $scCO_2$ and that for brine was calculated from the capillary number. For imbibition, the injection rate at the inlet was set to zero for brine and that for $scCO_2$ was calculated from the corresponding capillary number.

Details of simulation processes

In the first set of numerical experiments, a uniform $scCO_2$ injection velocity of 0.026 m/s was used at the inlet of the numerical model (Ottawa F42 Sand Pack) for the drainage process. This velocity was calculated from the capillary number 1.5×10^{-5}. For set 1, the simulation of the drainage process was run with a contact angle of 5°. After completion of the drainage process, the brine injection (imbibition) process was run with a contact angle of 45° and a uniform brine injection velocity of 0.03 m/s. This velocity was calculated from a capillary number of 1.0×10^{-3}. In the second set of numerical experiments, two different capillary numbers were considered arbitrarily for the simulations of the drainage and imbibition processes: 2×10^{-5} and 1.2×10^{-3}, respectively. At this stage, simulations of the drainage and imbibition processes were run with contact angles of 5° and 30°, respectively. The fluid saturations and variations in pressure drop for each flow sequence were observed accordingly.

The distribution of $scCO_2$-brine flow and variations in pressure drop for sets 1 and 2 are presented in the next sections. Detailed representations of $scCO_2$-brine distributions for set 2 are presented in Appendix D.

4.2.1. Simulation of the drainage process (set 1)

Figure 4.4(a-c) shows the distribution of fluids in the Ottawa F42 Sand Pack during the drainage process for set 1 (with a fluid injection rate = 0.026 m/s).
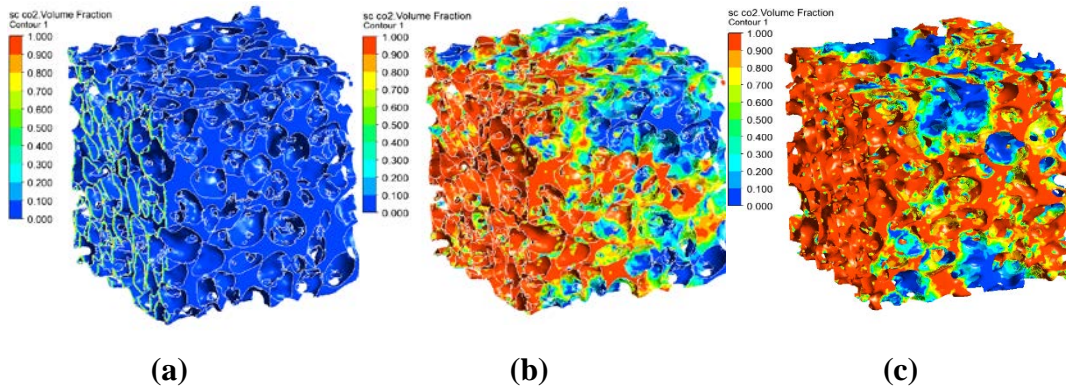
Figure 4.4(a-c) showed the distribution of brine and scCO$_2$ in the Ottawa F42 Sand Pack at various simulation times during the drainage process. In these figures, red indicates the scCO$_2$ distribution and blue indicates the brine distribution. The flow direction is from left to right.

At the beginning of the drainage simulation, with a simulation time of zero seconds, the sample was considered to be fully saturated with brine, which is shown as blue colour in Figure 4.4(a). Eventually, after the commencement of the drainage simulation with injection of scCO$_2$, different combinations of scCO$_2$-brine phase distribution were observed.

Figure 4.4(b) represents the scCO$_2$-brine phase distribution within the pore spaces at the middle of the simulation of the drainage process (simulation time = 10 s). The value of residual scCO$_2$ saturation (at this stage) was about 0.686 (scCO$_2$-brine phase distributions are represented by red, yellow, orange and light green in the pore spaces). Brine was distributed mostly in the corners of the scCO$_2$-filled pore spaces and throats, which represents an invasion percolation process (Blunt, 1998). Also, CO$_2$ movement at this stage was influenced by gravity segregation (Qi et al., 2009). Gravity segregation is the tendency of CO$_2$ to migrate to the top under the influence of buoyancy, as the density and viscosity of CO$_2$ are much lower compared to those of brine.

Figure 4.4(c) represents the scCO$_2$-brine phase distribution after the completion of the drainage process (simulation time = 25 s). It is clear from Figure 4.4(c) that brine was present in crevices within pore spaces and also may have been present in the smaller pores and throats. The scCO$_2$-brine phase distributions are represented by light and dark blue in Figure 4.4(c). Moreover, more brine was displaced by scCO$_2$ than shown

in Figure 4.4(b) and it gathered at/near the outlet (the $scCO_2$-brine distribution shows less blue coloured region than before). In this case, the $scCO_2$ saturation was observed to be 0.70 (represented by red, yellow, orange and light green in the pore spaces). It can be concluded that the instability of the fluid displacement front reduces the sweep efficiency and, thus, $scCO_2$ saturation decreases (Suekane & Ushita, 2011).

If this process is continued for more than 25 s, then further displacement of brine by $scCO_2$ is expected (Raeini et al., 2014).

4.2.2. Simulation of the drainage process (Set 2)

For set 2, a uniform velocity of 0.035 m/s was used in the simulation of the drainage process. This value is calculated from the capillary number 2.0×10^{-5}. Figure 4.5(a-c) represents the 3D fluid ($scCO_2$-brine) distribution for the drainage process for set 2. Figure 4.5(d) shows the variation in pressure drop from the inlet to the outlet of the sample during the drainage processes (for both sets).

(a)   (b)   (c)
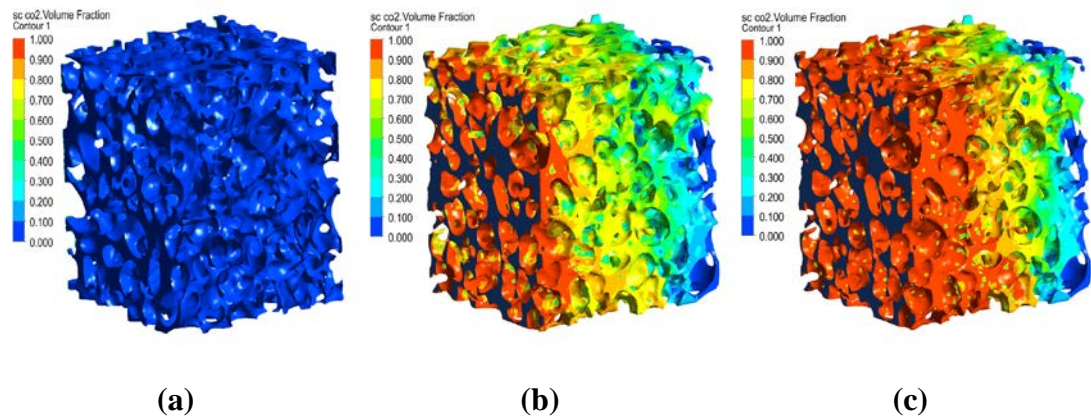
Figure 4.5: (a-c) Show the distributions of trapped brine (red) and $scCO_2$ (blue) in Ottawa F42 Sand Pack at various simulation times for set 2. The flow is from left to right.

At the beginning of the simulation, as observed in Figure 4.5(a), there was no $scCO_2$ within the pore zones because the sample was fully saturated with brine. Blue colour represents this situation in Figure 4.5(a).

In Figure 4.5(b), at a simulation time of 10 s, it can be observed that more brine was displaced with $scCO_2$ than before (more red, blue, green and yellow coloured regions). At this point, the value of initial $scCO_2$ saturation is observed to be about 0.64.

At a simulation time of 25 s, the drainage process was stopped. Figure 4.5(c) shows the distributions of brine and $scCO_2$ within the pore zones at this time. The residual saturation of brine was observed to be 0.225. Actually, a significant amount of brine appeared to be present (near the outlet) after the completion of drainage, as depicted in Figure 4.5(c) by blue colour. If the simulation continued for a longer period, the brine saturation would be expected to decrease further.

Figure 4.5(d) describes the variation in pressure drop as a function of simulation time for various drainage processes.
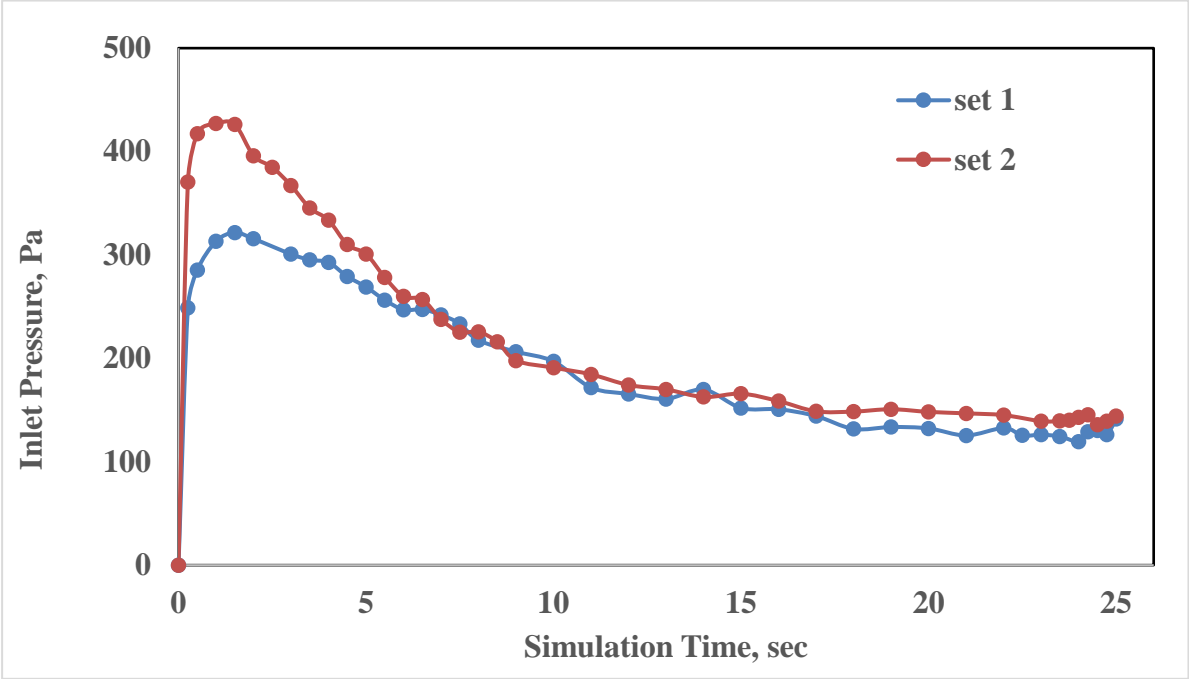
Figure 4.5(d): Variation in pressure drop as a function of simulation time for the drainage processes.

As can be seen in Figure 4.5(d), the pressure drop during drainage was 322 Pa at a simulation time of approximately of 1.5 s for set 1. This pressure drop may be considered as the threshold pressure drop at which $scCO_2$ starts to invade the sample. The threshold pressure can be considered as the minimum pressure required to break the thick brine film surrounding all the solid surfaces, and this is reflected by a sharp decrease in pressure (see Figure 4.5(d)). This threshold pressure, however, is dependent on the curvature of the pore wall and the mineralogy of the solid surfaces of the rock sample (Blunt, 1998). At a simulation time of 15 s, the pressure drop appeared to be almost constant, which infers that the drainage process reached a

steady-state condition. At the end of the drainage process (time = 25 s), the pressure drop was about 140 Pa.

Similarly, the threshold pressure drop during drainage was observed to be 427 Pa at a simulation time of approximately 1.0 s for set 2. After this point, the pressure started to decrease as both $scCO_2$ and brine drained out at the outlet. At the end of the drainage process (25 s), the pressure drop was 145 Pa when the system reached a steady state.

4.2.3. Simulation of the imbibition process (set 1)

Simulation of the imbibition process involved the injection of brine into the pore spaces. These micropores were assumed to be saturated with brine and $scCO_2$ after completion of the drainage process (set 1).

Figure 4.6(a-c) shows the fluid ($scCO_2$-brine) distribution within pore spaces of the Ottawa F42 Sand Pack for the simulation of imbibition with an inlet brine velocity of 0.03 m/s (set 1).

| (a) | (b) | (c) |
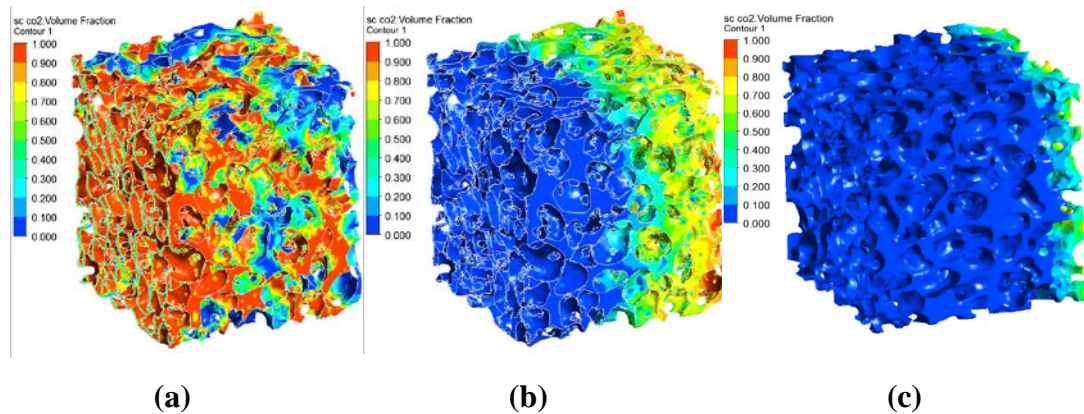
Figure 4.6: (a-c) 3D distribution of trapped brine and scCO$_2$ in the model at various times during imbibition with an inlet velocity of 0.03 m/s. Colours are the same as before. Flow is shown from left to right.

The sample was saturated with brine and $scCO_2$, as shown in Figure 4.6(a) at the start of the imbibition simulation. In Figure 4.6(a), the blue colour represents the brine and other colours (red, yellow and light green) represent $scCO_2$ within pore spaces. The value of $scCO_2$ saturation was about 0.70.

Figure 4.6(b) describes the situation of fluids ($scCO_2$ and brine) at the middle of the imbibition process (simulation time = 10 s). It is clear that the brine displaced more $scCO_2$ towards the outlet than that shown in Figure 4.6(a); and gathered at or near the inlet (more blue coloured region than before). The value of $scCO_2$ saturation, in this case, was observed to be about 0.097. Thus, there was a decrease in $scCO_2$ saturation. This decreasing trend is believed to be due to the loss of internal connectivity, and an increase in the level of fragmentation of $scCO_2$ into disconnected clusters (Schlüter et al., 2016). The fluid ($scCO_2$ and brine) displacement at this stage was dominated by snap-off as brine displaced $scCO_2$. Eventually, a portion of upward-moving $scCO_2$ was trapped as residual, immobile droplets, which were surrounded by brine droplets (Qi et al., 2009). This situation is an indication of the value of the capillary pressure drop (after the threshold pressure), which can be observed in Figure 4.7(d).

Figure 4.6(c) shows the distribution of brine and $scCO_2$ within pore spaces after completion of the imbibition process (simulation time = 25 s). The value of residual $scCO_2$ saturation, in this case, was observed to be about 0.05 (represented by light green and yellow colours).

4.2.4. Simulation of the imbibition process (set 2)

Figure 4.7(a-c) shows the fluid ($scCO_2$-brine) distribution within the pore spaces of the Ottawa F42 Sand Pack during imbibition (inlet brine velocity = 0.035 m/s) for set 2. In these figures, colour codes are the same as explained earlier for the imbibition process. The flow is shown from left to right.

| (a) | (b) | (c) |
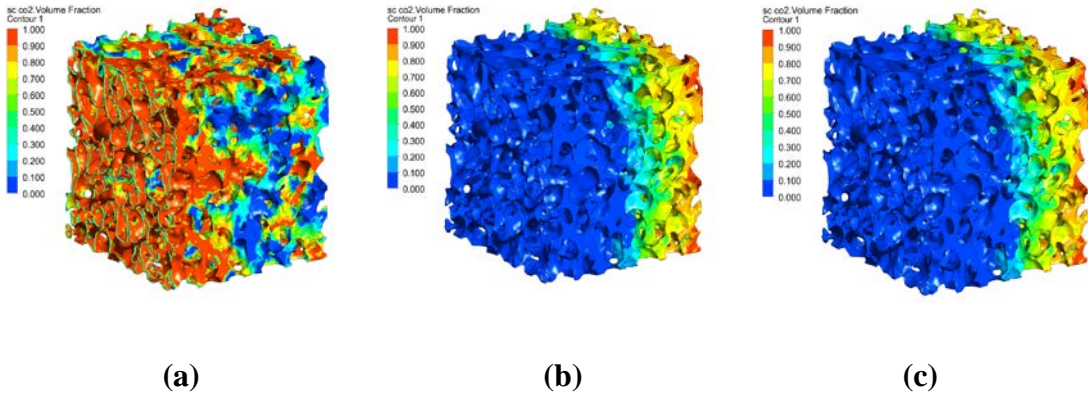
Figure 4.7: (a-c) 3D distribution of trapped brine and $scCO_2$ in the model at various simulation times (zero, 10 and 25 simulation seconds respectively) during

imbibition with an inlet velocity of 0.035 m/s. Colours are the same as before. Flow is shown from left to right.

Like the set 1 imbibition process, the Ottawa F42 Sand Pack was saturated with brine and $scCO_2$ before the commencement of the imbibition simulation, as shown in Figure 4.7(a). The value of brine saturation, in this case, was about 0.227.

Figure 4.7(b) shows the $scCO_2$- brine distribution at a simulation time of 10 s. From the figure, it can be observed that the brine displaced more $scCO_2$ towards the outlet than that shown in Figure 4.7(a); and gathered at or near the inlet (more blue coloured region than before).

Figure 4.7(c) shows the distribution of brine and $scCO_2$ within pore spaces after completion of the imbibition process (simulation time = 25 s). The value of residual brine saturation was about 0.9485.

Figure 4.7(d) describes the pressure drop variations at various times during the imbibition simulation for sets 1 and 2.
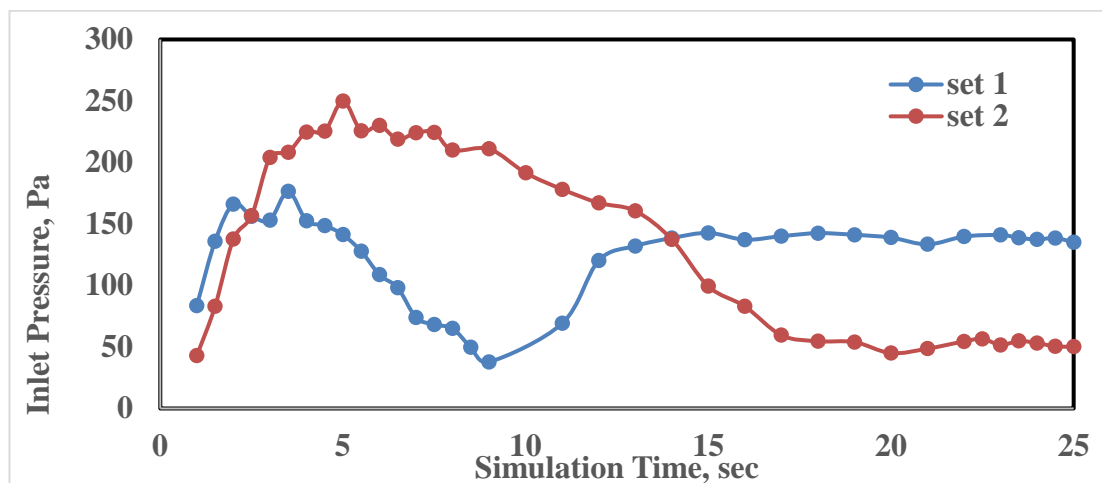
Figure 4.7(d): Variation in pressure drop vs simulation time during imbibition processes for sets 1 and 2.

In Figure 4.7(d) blue colour denotes the set 1 imbibition process. The pressure drop is observed to be 84 Pa when at a simulation time of approximately 1 s. After this, the pressure increases gradually as brine advances forward within the pore spaces. At a simulation time of approximately 5 s, the highest pressure drop was observed (176 Pa), and then it commenced to decline again. This highest pressure is the threshold pressure

89

(as described before) of the imbibition process. After 17 s, the pressure drop appeared to be almost constant, indicating that the system reached a steady state. At the end of the imbibition process (25 s), the pressure drop was about 150 Pa (at a steady-state condition).

In Figure 4.7(d), red colour denotes the set 2 imbibition process. The observed pressure was 43 Pa at approximately 1 s, and the threshold pressure drop was about 250 Pa. After 17 s, the pressure drop appeared almost constant, indicating that the system reached a steady state. Finally, at the end of the imbibition process (25 s), the pressure was observed to be 50 Pa.

If both imbibition processes are compared between sets, it can be seen that the pressure drop decreased with decreases in the contact angle (set 1 $\theta = 45°$ and set 2 $\theta = 30°$) during the middle of the simulation (around 3–14 s). This situation resulted in frontal advancement of brine invasion, which is relatively flat and resulted in a little trapping of $scCO_2$ (Blunt, 1998).

However, for the other simulation time spans (0–2 s and 15–25 s), the pressure drop pattern was completely reversed.

As F42 Sand Pack is highly permeable, less trapped $scCO_2$ made the sample (Ottawa F42 Sand Pack) less favourable for effective $scCO_2$ storage. However, the initial $scCO_2$ saturation also depends on the inlet flow rate.

4.3. *Prediction of fluid relative permeability for a scCO₂-brine system*

The prediction of $scCO_2$ and brine relative permeability is very important for an efficient CCS system, as these parameters influence CO_2 migration, distribution, dissolution and trapping of $scCO_2$ in the reservoir (Busch & Müller, 2011). In this regard, numerical simulations (for drainage and imbibition processes) were conducted on the micro-pores of the Ottawa F42 Sand Pack for a $scCO_2$-brine system. The objective was to investigate the influence of the inlet fluid flow rate on fluid relative permeability and $scCO_2$ capillary pressure. In this regard, a numerical model was created in a similar way as described in Section 4.1.1 for Ottawa F42 Sand Pack. To estimate inlet fluid flow rates for drainage and imbibition processes, capillary numbers were chosen that were greater than 10^{-6}. Moreover, different contact angles were

chosen for the imbibition processes. In this work, set 1 describes a drainage $scCO_2$ velocity = 0.026 m/s with a contact angle of 5°, while set 2 describes a drainage $scCO_2$ velocity = 0.035 m/s with the same contact angle. For the simulation of imbibition processes, the set 1 brine velocity = 0.03 m/s with a contact angle of 45° and the set 2 brine velocity = 0.035 m/s with a contact angle of 30°.

Following the workflow discussed earlier, the $scCO_2$ and brine relative permeability was predicted using the start-point and end-point saturation values obtained from the simulation results shown in Table 4.2 and the analytical models presented earlier in Section 4.1.2. Sample model calculations are provided in Appendix A to demonstrate how the values were calculated.

Table 4.2: Relative permeability results for set 1 and 2 of the numerical simulations.

Fluid injection velocity, m/s	Fluids		Saturation (v/v) at the start	Saturation (v/v) at the end	Brine Relative Permeability		Super-critical CO_2 Relative Permeability	
					Start	End	Start	End
0.026 (set 1)	Drainage (at 5°)	Brine	1.00	0.300	1.0000 (Corey)	0.0033 (Corey)	0.00 (Corey)	0.550 (Corey)
		scCO$_2$	0.00	0.700				
0.030 (set 1)	Imbibition (at 45°)	Brine	0.30	0.950	0.0033 (Land)	0.8000 (Land)	0.58 (Land)	0.003 (Land)
		scCO$_2$	0.70	0.050				
0.035 (set 2)	Drainage (at 5°)	Brine	1.00	0.230	1.000 (Corey)	0.0004 (Corey)	0.00 (Corey)	0.722 (Corey)
		scCO$_2$	0.00	0.740				
0.035 (set 2)	Imbibition (at 30°)	Brine	0.23	0.950	0.0004 (Land)	0.8730 (Land)	0.74 (Land)	0.001 (Land)
		scCO$_2$	0.74	0.052				

4.3.1. Prediction of fluid relative permeability for drainage processes

Figure 4.8 shows the estimated brine and $scCO_2$ relative permeability results during simulation of drainage processes for set 1 and set 2.
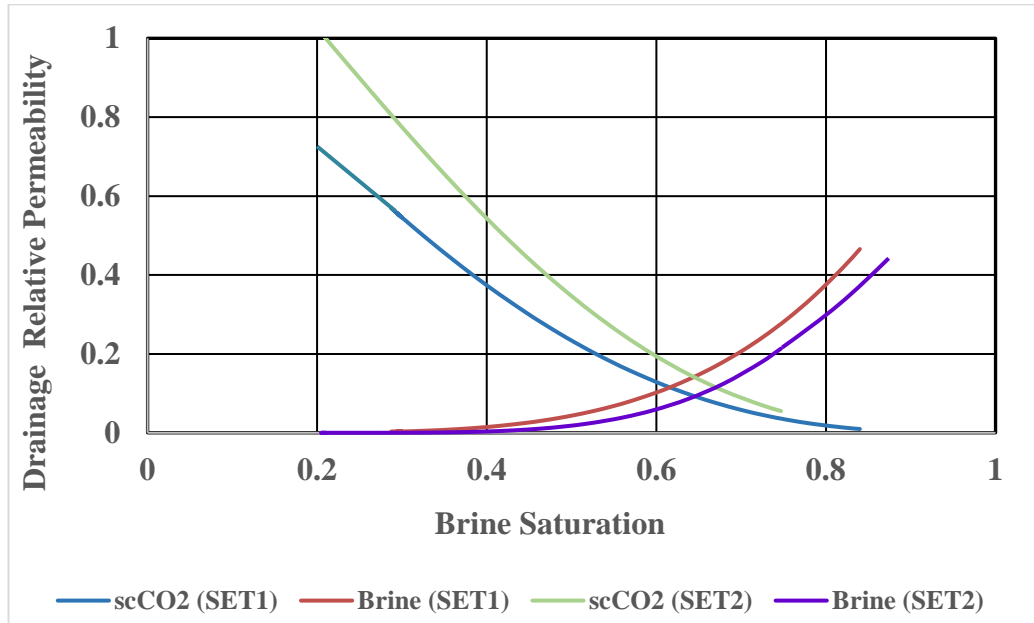
Figure 4.8: Corey drainage relative permeability as a function of brine saturation with scCO₂ inlet velocities of 0.026 m/s (set 1) and 0.035 m/s (set 2).

The end-point brine relative permeability values obtained from the numerical drainage simulation were about 0.00327 and 0.0004 for sets 1 and 2, respectively, whereas the corresponding end-point $scCO_2$ relative permeability values were 0.55 and 0.77, respectively (as shown in Table 4.2). The greater end-point values of $scCO_2$ relative permeability revealed that the brine occupied the smaller pores and had less influence on $scCO_2$ flow. It can be assumed that after a certain time period, the relative permeability of $scCO_2$ will approach unity when the relative permeability to brine is restricted (close to zero).

This situation can also be understood if both drainage processes are compared with each other in terms of brine relative permeability. Then it can be observed from Figure 4.8 that the relative permeability to brine decreases sharply for a small reduction in brine saturation (0.6 to 0.8). This situation occurred as $scCO_2$ filled up and moved through the larger pores or throats. The presence of $scCO_2$ in these larger pores or throats showed considerable interference to the flow of fluid within the pore spaces of

the Ottawa F42 Sand Pack (Abeci et al., 1992). This behaviour suggests that inlet brine flow may influence relative permeability to scCO$_2$ and brine during drainage cycles.

4.3.2. Prediction of fluid relative permeability values for imbibition processes

Imbibition fluid relative permeability values were predicted via simulation (Table 4.2) and the analytical model described in Section 4.1.2 for sets 1 and 2. The results are shown in Figure 4.9.
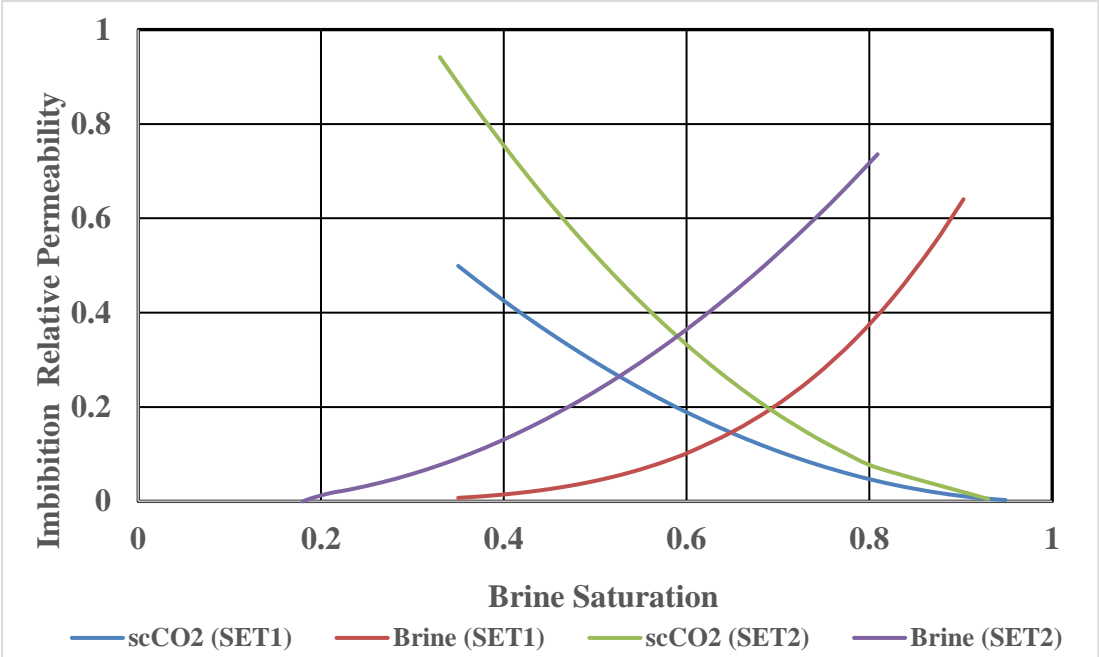
Figure 4.9: Land imbibition relative permeability vs brine saturation with inlet brine velocities of 0.031076 m/s (set 1) and 0.035 m/s (set 2).

In Figure 4.9, it can be observed that for the same saturation (0.25–0.75), imbibition relative permeability to scCO$_2$ was higher for set 2 than set 1. Similar to the drainage cycle simulations, relative permeability to scCO$_2$ (for sets 1 and 2) was higher than that of brine, which can be observed from Figure 4.9.

If the set 1 and set 2 imbibition cycles are compared, it appears that a decrease in the contact angle (set 1 θ = 45° and set 2 θ = 30°) results in an increase in the snap-off mechanism for fluid flow through the pore spaces of the Ottawa F42 Sand Pack. This small increase in the snap-off, in turn, is believed to be responsible for the increase in scCO$_2$ residual saturation (0.05 for set 1 and 0.0515 for set 2). However, at low residual scCO$_2$ saturations, imbibition proceeded within the pore spaces of the Ottawa F42

Sand Pack by cooperative pore filling with little snap-off and capillary trapping due to its high porosity (Pentland et al., 2010). This low residual $scCO_2$ saturation leads to poor $scCO_2$ storage efficiencies, which may make the Ottawa F42 Sand Pack unfavourable for CCS.

5. Chapter 5: Numerical Simulation for Berea Sandstone

This chapter presents and discusses supercritical CO_2-brine (scCO_2-brine) distribution, and uses numerical simulations to predict the relative permeability and capillary pressures found in the pore spaces of Berea sandstone.

Background

In the previous chapter (Chapter 4), pore-scale numerical simulations pertaining to the prediction of scCO_2-brine distribution, relative permeability and scCO_2 capillary pressure in Ottawa F42 Sand Pack were presented. The characteristics of a subsurface geological storage or reservoir system are often different from the view point of geological settings, depositional environments, or similar rock formations. In this regard, the work is extended to study different reservoir rocks and, accordingly, Berea sandstone was used for this simulation study to simulate drainage and imbibition processes under various conditions. As mentioned in Chapter 4, an oil-brine system was considered to validate the numerical model due to the unavailability of data for scCO_2-brine systems. Hence, the numerical model can be used analogously for a scCO_2-brine system.

The analytical models presented in Chapter 4 (Section 4.1.2) are used for the prediction of capillary pressure and relative permeability.

5.1. *Description of the Numerical Model*

Similar to Ottawa Sand Pack 42 (as discussed in Chapter 4), the Berea sandstone was modelled using the commercial image processing software AVIZO. It was used to separate the network of pore spaces in an actual formation. A surface mesh was first generated in the model, which was then converted into a volume mesh using the ANSYS ICEM CFD processor, as shown in Figures 5.1 and 5.2. The generated volume mesh was used in ANSYS CFX to perform numerical simulations of drainage and imbibition processes.
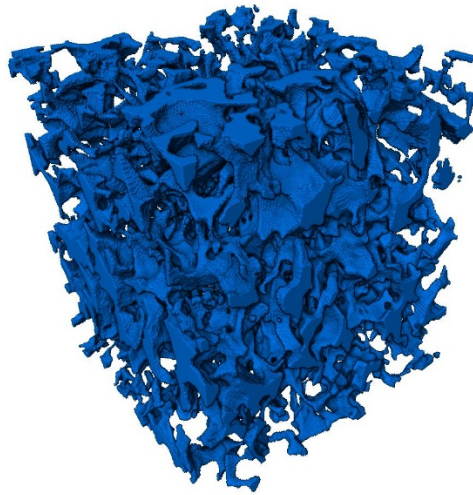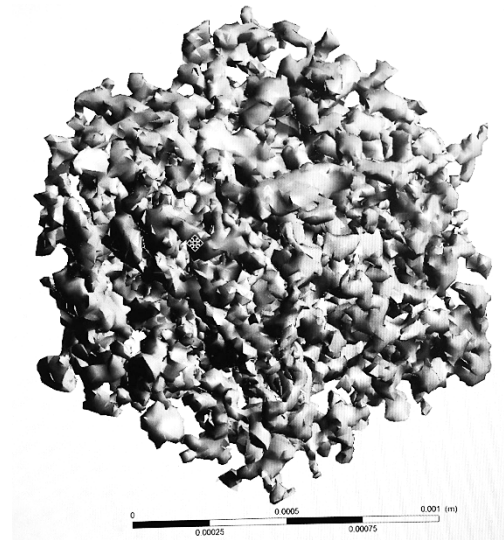
Figure 5.1   **Figure 5.2**

Figure 5.1: Digital volume mesh of the numerical model created based upon Berea sandstone (left); and Figure 5.2: Enlarged view of the volume mesh (right).

The numerical simulation was run under transient conditions for 40 s in 0.01 s time steps, with recordings made every 0.25 s. The CFX Command Language (CCL) was used, which is quite similar to that presented in Appendix B (for further information). In Appendix B, the CCL was used for a $scCO_2$-brine system in the Ottawa F42 Sand Pack.

The model was considered as a fluid domain and all fluids are continuous with a reference pressure of zero. The gravity effects in the X and Z directions were neglected. The gravitational acceleration in the negative Y direction ($-Y$) was considered to be 9.81 m/s^2, and the domain motion was assumed to be stationary with respect to the reference frame.

The inlet flow rate and contact angle for the simulation of the drainage process were 0.026 m/s and $\theta = 45°$, respectively. For simulation of the imbibition process, 0.03 m/s and $\theta = 85°$ were used. These inlet fluid velocities were calculated from the corresponding capillary numbers (2.5×10^{-4} and 7.0×10^{-4}). For drainage process, viscosity of $scCO_2$ was used to calculate capillary number. For imbibition process, viscosity of brine was used to calculate capillary number. For both processes, surface of $scCO_2$-brine was considered to be remained same. The drainage/imbibition process is considered to be completed when the value of observed pressure drop becomes

stable for successive number of simulation times. . After completion of the drainage and imbibition processes, the fluid saturation and pressure drop were observed, and the oil and brine relative permeability, and oil capillary pressure values were estimated using the analytical models described in Chapter 4.

Berea sandstone is typically used as a standard reservoir rock in much petroleum engineering core research, especially in core flooding and for the analysis of various petro-physical properties, mainly due to its ready availability. It is primarily composed of quartz and small amounts of feldspar, dolomite and clays (Øren et al., 2003). The porosity and permeability of Berea sandstone are 0.23 and 1.1 mD, respectively (Øren et al., 2003). The oil viscosity and oil-brine surface tension considered in this study were 5.04×10^{-4} Pa and 51.64×10^{-3} N/m, respectively.

The various saturations described above were obtained by numerical simulation of the oil-brine system (Table 5.1).

Table 5.1: Various saturation values obtained by simulation

Saturation	Value obtained from simulation
Connate brine saturation, S_{wc}	0.15
Maximum residual oil saturation, $S_{or,max}$	0.805
Initial brine saturation, S_{wi}	0.15
Initial oil saturation, S_{oi}	0.85
Residual oil saturation, S_{or}	0.13

The normalized trapped oil saturation ($Sot*$) was calculated using the analytical model following the process described in Chapter 4.

5.1.1. Model Validation

Following the same methodology described in Chapter 4, the numerical simulation results were compared with those of published works that used different approaches.

Talabi et al. (2008) conducted pore-scale numerical modelling for Berea sandstone using the maximum ball algorithm (MBA) for the prediction of fluid relative permeability and capillary pressure. The MBA algorithm identifies pore bodies and pore throats and establishes their respective volumes and connectivity based on

fundamental concepts of mathematical morphology (Silin & Patzek, 2003). Talabi et al. (2008) showed that fluid relative permeability and capillary pressure are affected by rock type, mainly the coordination number of the pores, the pore size distribution, and wettability. Valvatne et al. (2004) predicted wettability variation within an oil/water transition zone. They also used a pore-network model with conventional reservoir-scale simulations to predict the relative permeability and capillary pressure. Dong et al. (2009) also conducted numerical modelling to predict fluid relative permeability using the MBA method.

The drainage and imbibition relative permeabilities for oil-brine systems were obtained from the works of Talabi et al. (2008), Valvatne et al. (2004), Dong et al. (2009) and the current study, and are presented as functions of brine saturation (S_w) in Figure 5.3 and Figure 5.4, respectively.
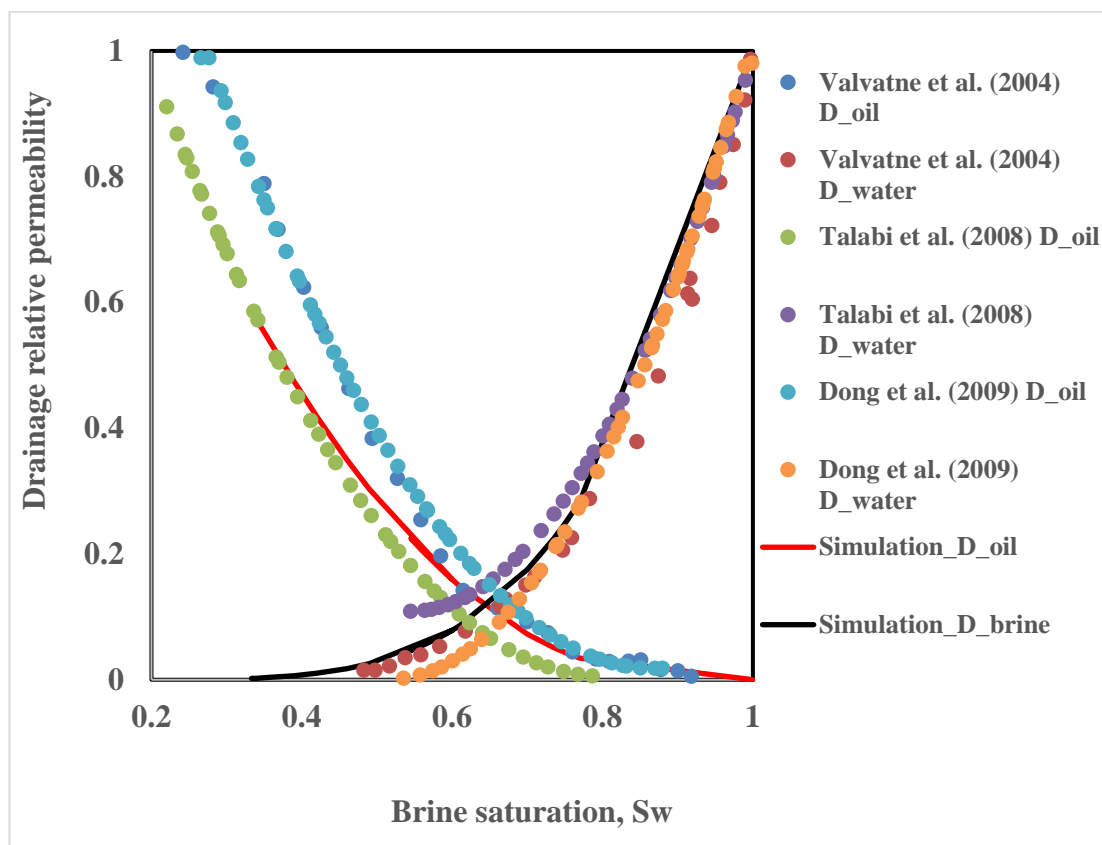
Figure 5.3: Comparison of predicted drainage relative permeability.

It can be seen from Figure 5.3 that the drainage oil relative permeability predicted by the current study is generally in close agreement with other works (Talabi et al., 2008;

Valvatne et al., 2004; Dong et al., 2009). However, the results obtained by the current study appear to under-predict the relative permeability at low brine saturations ($S_w <$ 0.5) compared to Dong et al. (2009) and Valvatne et al. (2004); and over-predict compared to Talabi et al. (2008). However, the drainage brine relative permeability predicted by simulation appears to be in reasonably good agreement with the other results, especially for brine saturations > 0.5.
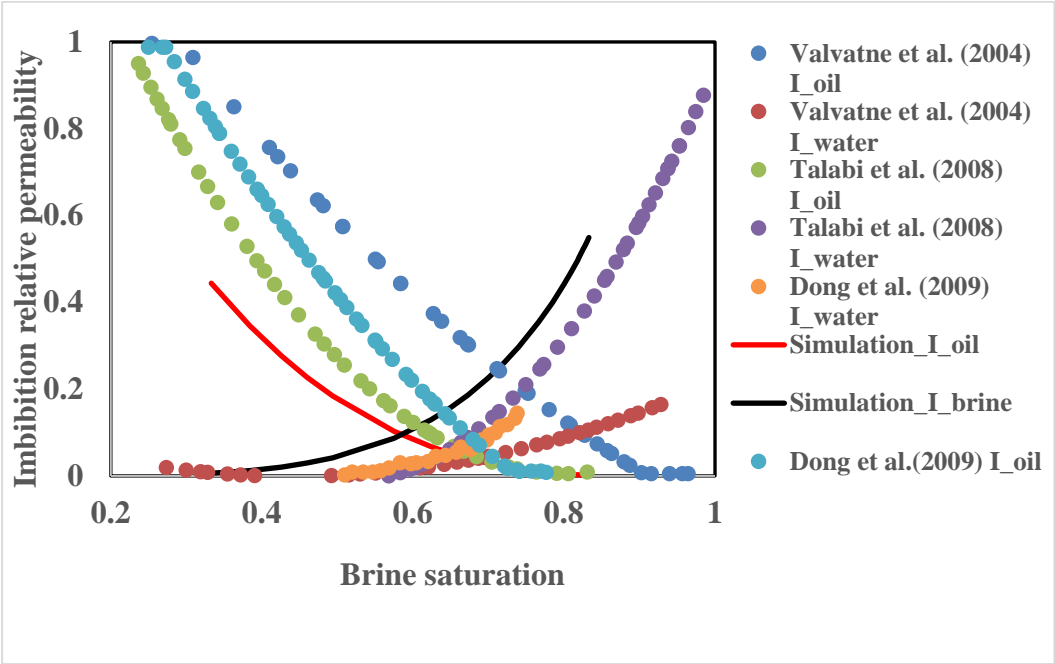
Figure 5.4: Comparison of predicted imbibition relative permeability.

The oil and brine relative permeabilities for imbibition processes obtained from simulation studies and other works (Dong et al., 2009; Valvatne et al. 2004; Talabi et al., 2008) were plotted as a function of the brine situation. The imbibition oil relative permeability appears to be underestimated by the simulation compared to the others' approaches. This situation indicates more snap-off trapping oil within the pore spaces of Berea sandstone. From Figure 5.4, it can also be observed that the imbibition brine relative permeability appears to be slightly over-estimated as compared to the other approaches. Such anomalies occur due to the wide range of contact angles and surface tensions considered by the other studies. As different authors have used different ranges of contact angles and surface tensions, the surface tension considered in thesis work for numerical simulation was taken from Pentland et al. (2011), as explained in section 4.1.4.2. The reference of this particular surface tension value is different other than the 3 (three) published references presented in the Figure 5.4.
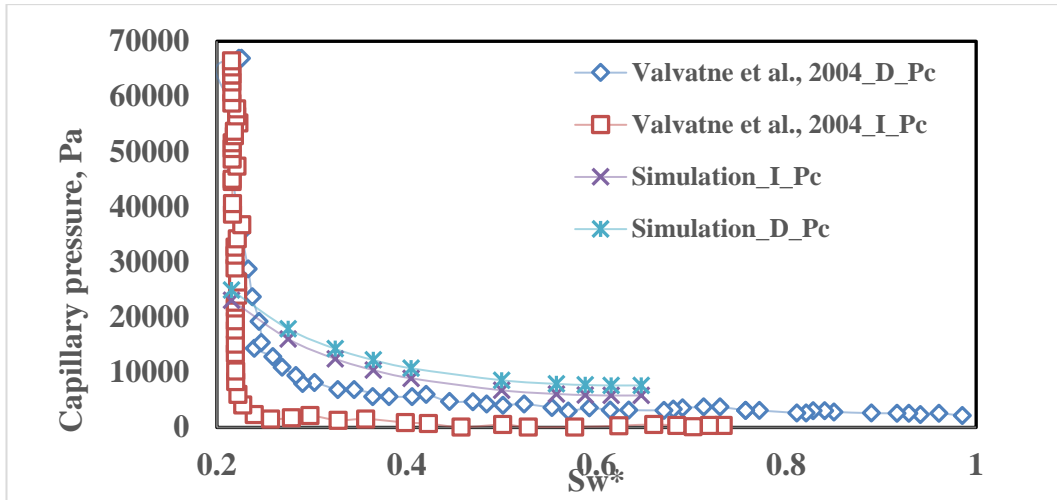
Figure 5.5: Comparison of drainage and imbibition oil capillary pressures.

The drainage and imbibition oil capillary pressures are shown in Figure 5.5. The simulated imbibition oil capillary pressure shows reasonably good agreement with the results of Valvatne et al. (2004). The drainage oil capillary pressure shows some anomalies, though the predicted results follow the same trend. However, the range of predicted oil and relative permeabilities for both drainage and imbibition processes, and the capillary pressure for Berea sandstone, were in close proximity or consistent with those of various other studies, as presented in Tables 5.2 and 5.3.

Table 5.2: Fluid relative permeability reported in various references for Berea sandstone.

Fluid pair	References	Oil/water saturation range	Oil relative permeability		Gas/water relative permeability	
Kerosene-helium	Richardson et al. (1952)	0.50-1.0 (oil)	0.0-0.4		0.0-1.0	
Oil-water	Valvatne et al. (2004)	0.25-1.0 (water)	0.0-1.0 (drainage)		0.25-1.0 (drainage)	
Oil-water	Jackson et al. (2003)	0.24-1.0 (water)	0.0-1.0 (drainage)	0.0-1.0 (imbibition)	0.24-1.0 (drainage)	0.0-0.15 (imbibition)
Oil-water	Talabi et al. (2008)	0.20-1.0 (water)	0.0-1.0 (drainage)	0.0-1.0 (imbibition)	0.0-1.0 (drainage)	0.0-1.0 (imbibition)
Oil-water	Valvatne et al. (2005)	0.25-1.0	0.0-1.0 (drainage	0.0-1.0 (imbibition)	0.0-0.8 (drainage)	0.0-1.0 (imbibition)
Oil-water	Dong et al. (2009)	0.25-1.0	0.0-1.0 (drainage	0.0-1.0 (imbibition)	0.0-0.8 (drainage)	0.0-0.2 (imbibition)

Table 5.3: The capillary pressure reported in various references for Berea sandstone

Fluid pair	References	Porosity, Ø	Permeability, K (mD)	Capillary pressure range, Pa	
N_2-water (Hg-injection technique for Drainage system)	Li and Horne (2006)	0.234	1200	689-6.9e^7	
Kerosene-helium	Richardson et al. (1952)	0.177	107	5516-12411	
Oil-water	Jackson et al. (2003)	Network model used		400-65000 (drainage)	0-65000 (imbibition)
Oil-water	Anderson et al. (1987)	-	184	2400-40000 (drainage)	
Oil-water	Valvatne et al. (2005)	Network model used		3500-70000 (drainage	0-70000 (imbibition)

5.2. *Simulation of a supercritical CO₂-brine system for Berea sandstone*

After validation, the numerical model described in Section 5.1 was used to simulate a supercritical CO_2-brine (scCO_2-brine) system for Berea sandstone. Two different sets of inlet fluid flow rates were used during simulation of drainage and imbibition processes. All capillary numbers considered were greater than 10^{-6}, which is below the critical value (the observed value of the critical capillary number for Berea sandstone is greater than the range 10^{-5} to 10^{-4}), to ensure capillary-dominated fluid distribution within the pore spaces (Al-Menhali et al., 2015).

The inlet fluid flow rates and boundary conditions were similar to those used for the Ottawa F42 Sand Pack, as described in Chapter 4 and Section 5.1.

The simulation results for a scCO_2-brine system undergoing drainage and imbibition processes are presented and discussed in this section. The fluid saturations for each flow sequence were observed respectively with the aid of ANSYS CFD-Post. Then, the fluid relative permeability values were calculated for all cases.

5.2.1. Results and Discussion

5.2.1.1. Simulation of scCO₂-brine system

Numerical simulations of drainage and imbibition processes for the scCO_2-brine system were carried out for two different inlet (or injection) rates. Two sets were

considered based on these injection rates. The injection rates for set 1 were 0.026 for drainage and 0.03 m/s for imbibition, whereas the injection rate for set 2 was 0.035 m/s for both drainage and imbibition. A contact angle of 5° was considered for both sets. Fluid saturation at various simulation times was observed and used to estimate the brine and $scCO_2$ relative permeability values.

For each set, a uniform $scCO_2$ injection or inlet velocity was used at the inlet of the numerical model (Berea sandstone) for the drainage process. All the other faces except the inlet and outlet of the model were assumed to be impermeable, which was achieved by applying no-slip wall boundary conditions. Initially, the model was considered to be saturated with brine before the start of $scCO_2$ injection. Moreover, all simulations were run with a time-step size of 0.01 s in order to reduce computation time and achieve faster convergence. The simulation of drainage processes was run with a contact angle of 5° (for both sets). The imbibition simulation processes were repeated for contact angles of 45° and 30°, respectively (for sets 1 and 2). The pressure drop for each flow sequence was reported accordingly. The properties of the fluids used and the boundary conditions applied at the inlet of the numerical model are presented in Table 5.4.

Table 5.4. Properties of scCO₂ and brine and other parameters in the scCO₂-brine system simulation.

Fluid	ρ (kg/m^3)	μ (Pa.s)	Surface tension, σ (Nm^{-1})
scCO$_2$	469	0.000021	0.036
Brine	1070.7	0.001193	

5.2.1.2.   Prediction of relative permeability for the scCO₂-brine system

The start- and end-point brine and $scCO_2$ relative permeability values for the drainage and imbibition processes for both sets were predicted using the Corey and Land models described in Chapter 4 and are presented in Table 5.5. The predicted scCO2 and brine relative permeability values presented in Table 5.5 are compared with similar published results. The predicted values are in good agreement with the published results of Richardson et al. (1952); Valvatne et al. (2004); Jackson et al. (2003); Talabi et al. (2008); Valvatne et al. (2005); and Dong et al. (2009).

From Table 5.5, it is also clear that the increase in the value of inlet brine velocity (during imbibition), resulted in an increase in $scCO_2$ relative permeability and residual saturation of $scCO_2$ for set 2 ($\theta = 30°$) if compared with set 1 ($\theta = 45°$). This may be due to the higher inlet velocity and lower contact angle considered in set 2.

Table 5.5: Relative permeability results for numerical simulation sets 1 & 2.

Fluid inlet or injection velocity (m/s)	Fluid	Start saturation (v/v)	End saturation (v/v)	Brine Relative Permeability		scCO₂ Relative Permeability	
				start	end	start	end
0.026 (set 1 drainage)	Brine	1.0	0.284	0.515 (Corey)	0.00097 (Corey)	0.0066 (Corey)	0.692 (Corey)
	scCO₂	0.0	0.716				
0.03 (set 1 imbibition)	Brine	0.284	0.84	0.0028 (Land)	0.576 (Land)	0.554 (Land)	0.0092 (Land)
	scCO₂	0.716	0.16				
0.035 (set 2 drainage)	Brine	1.0	0.27	0.487 (Corey)	0.0004 (Corey)	0.0082 (Corey)	0.723 (Corey)
	scCO₂	0.0	0.73				
0.035 (set 2 imbibition)	Brine	0.27	0.86	0.0031 (Land)	0.67 (Land)	0.54 (Land)	0.000134 (Land)
	scCO₂	0.73	0.14				

The predicted brine and $scCO_2$ relative permeability values were analysed and compared with respect to a number of similar published works in order to gain a better understanding and interpretation of the results.

Soroush et al. (2013) conducted relative permeability measurements on Berea sandstone in order to investigate the effects of aquifer influx and injection rates on the imbibition process. They also observed wettability behaviour for CO_2 storage in aquifers. The results showed that relative permeability values were sensitive to flow rate and wettability. Krevor et al. (2012) performed core-flooding experiments to investigate residual trapping of CO_2 in the Berea sandstone at subsurface conditions. Moreover, they discussed the applications of reservoir-scale residual trapping curves through simulation. Al-Menhali et al. (2015) measured eight different capillary pressure characteristic curves on Berea sandstone under various conditions of ionic strength, pressure and temperature. Also, a benchmark measurement was performed for an N_2-water system for a strongly water-wet condition. Pini et al. (2013) measured relative permeability and capillary pressure characteristics for three different fluid sets (gaseous CO_2/water, gaseous N_2/water and $scCO_2$/brine). They observed these three fluid sets to yield the same drainage relative permeability curves. Furthermore, they

performed MICP tests, and Brooks-Corey (BC) models were used to describe the capillary pressure. Perrin et al. (2009) conducted steady-state laboratory experiments and numerical simulations over a range of fluid flow rates on Berea sandstone. Their objectives were to improve the understanding of multiphase fluid flow and trapping in CO_2-brine systems.

Figures 5.6 and 5.7 show the fluid relative permeability values for $scCO_2$ and brine under drainage and imbibition processes according to the present study compared with existing ones. The $scCO_2$ and brine relative permeability data for Berea sandstone obtained from various studies are also presented in Table 5.6. It is worth mentioning that the results of the present simulations are based on the inlet (or injection) velocity of $scCO_2$, whereas the inlet velocities used in other published works are not known. From Figures 5.6 and 5.7, it can be observed that the predicted results are very consistent with other works. For instance, the predicted brine and $scCO_2$ relative permeability for drainage appear to be close matches to those observed by Soroush et al. (2013) for set 1 (i.e. inlet velocity of 0.026 m/s). Similarly, the predicted brine and $scCO_2$ relative permeability for imbibition appear close matches to those reported by Perrin et al. (2013) for set 2 (i.e. inlet velocity of 0.035 m/s). Although the predicted brine relative permeability for both imbibition and drainage processes are quite close to those of other published works, the $scCO_2$ relative permeability showed some level of discrepancy. The level of discrepancy appeared to be sensitive to inlet or injection velocity, as shown in Figures 5.6 and 5.7. This observation is consistent with what was observed by Soroush et al. (2013), as discussed earlier.

Table 5.6: Brine and scCO₂ relative permeability data obtained from various published works (for drainage and imbibition processes).

Fluid pair	Reference	Brine saturation range	Porosity	Permeability, mD	scCO₂ relative permeability		Brine relative permeability	
LB method (steady-state)	Ramstad et al. (2012)	0.50-1.0 (wetting phase)	-	1000	0.0-0.95 (non-wetting phase, drainage)	0.0-0.97 (non-wetting phase, drainage)	0.5-0.9 (wetting phase, drainage)	0.0-0.30 (wetting phase, drainage)
CO_2-water	Shi et al. (2011)	0.45-1.0 (water)	0.187	330	0.0-1.0 (CO_2)		0.0-1.0	
CO_2-brine	Soroush et al. (2013)	0.2-1.0 (brine)	0.36	2000	0.0-0.75		0.0-0.3	
N_2-water	Pinni & Benson (2013)	0.40-1.0	0.188	340	0.05-1.0 (drainage)		-	
CO_2-water					0.10-1.0 (drainage)			
ScCO_2-brine					0.0-1.0 (drainage)			
CO_2-brine	Perrin et al. (2009)	0.40-1.0	-	-	0.0-0.8		0.0-0.5 (brine)	
CO_2-brine	Al-Menhali et al. (2015)	0.47-1.0	-	-	0.0-0.38 (drainage)	0.0-0.16 (imbibition)	0.0-0.48 (drainage)	0.0-0.06 (imbibition)
CO_2-water					0.0-0.15 (drainage)	0.0-0.15 (imbibition)	0.0-0.18 (drainage)	-
scCO₂-brine	Akbarabadi et al. (2013)	0.50-1.0	0.212	612	0.0-0.15 (drainage)	0.0-0.24 (imbibition)	0.0-0.50 (drainage)	0.0-0.50 (imbibition)
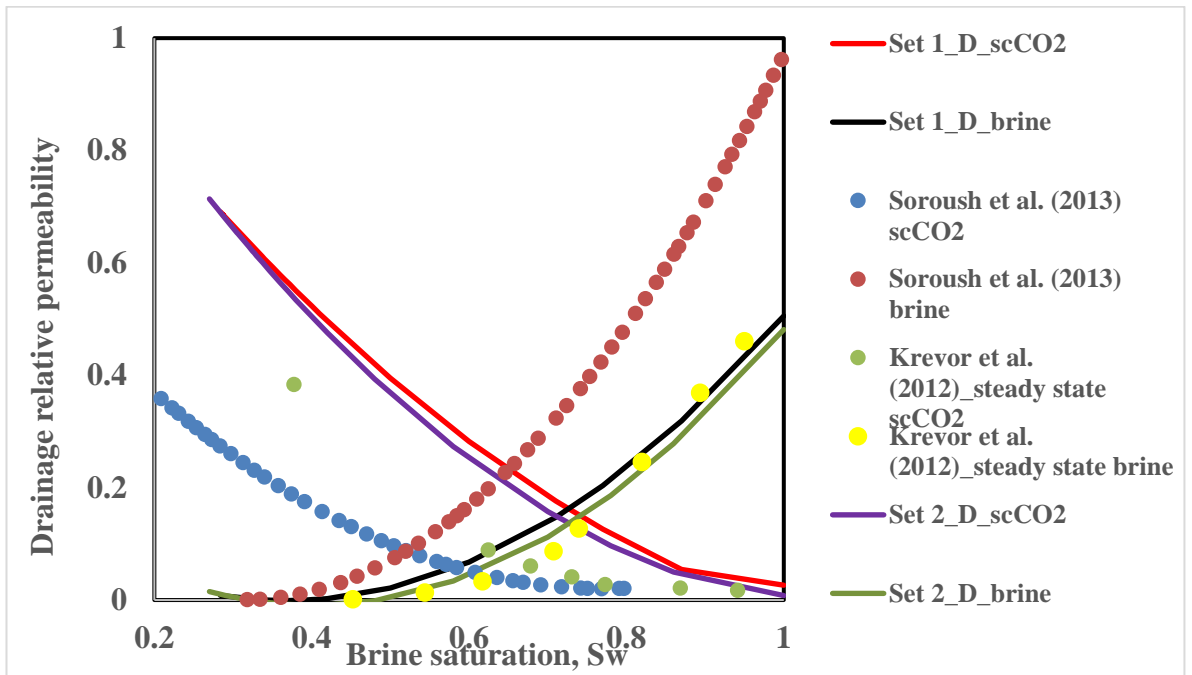
Figure 5.6: Comparison of predicted fluid drainage relative permeability with data from Soroush et al. (2013) and Krevor et al. (2012).
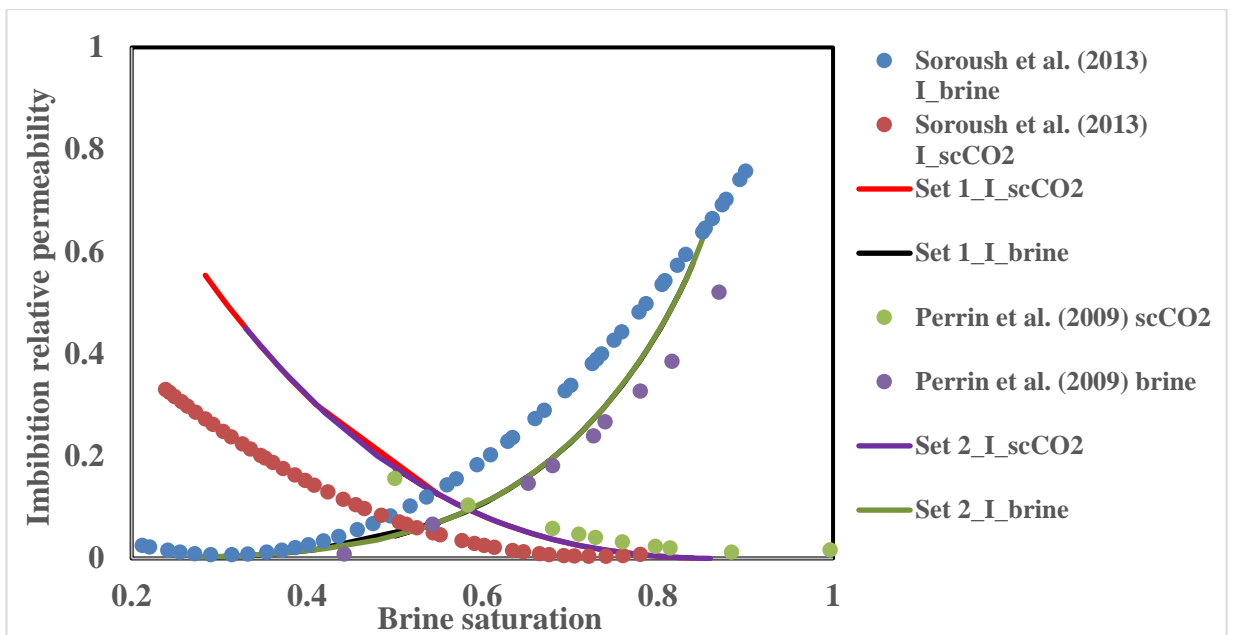
Figure 5.7: Comparison of predicted fluid imbibition relative permeability with data from Soroush et al. (2013) and Perrin et al. (2009).

In Figures 5.6 and 5.7, it can be seen that in every displacement cycle, the value of brine saturation did not decrease below 20%. This situation and the corresponding relative permeability are natural for a CO_2-brine system (Bachu & Bennion, 2008).

As can be seen in Figure 5.6, the predicted relative permeability curves for both fluids (scCO$_2$ and brine) intersect above the 50% saturation mark, characterising the establishment of a drainage process (Al-Menhali et al., 2015). Also, for Figure 5.6, for drainage processes, the set 1 scCO$_2$ relative permeability curve is steeper than that of set 2. This situation indicates the influence of different displacement rates (for set 1, scCO$_2$ velocity = 0.026 m/s and for set 2, scCO$_2$ velocity = 0.035 m/s) during the drainage processes. Displacement time at the higher displacement rate (set 2) was shorter than that at the lower displacement rate (set 1), which resulted in a very short time period for the snap-off mechanism. In other words, higher scCO$_2$ velocity provided a suppressing tendency for snap-off and trapping, something that was also observed by Nguyen et al. (2006).

From Table 5.6, the end-point drainage brine relative permeability are about 0.00097 and 0.0004 for set 1 and 2, respectively. Also, the end-point scCO$_2$ drainage relative permeability are about 0.692 and 0.723 for set 1 and 2, accordingly. The value of drainage relative permeability to scCO$_2$ (for sets 1 and 2) are within the expected range of 0.7–1.0 (Levine et al., 2013). During the imbibition process, the fraction of connected scCO$_2$ decreases and, at the same time, the fraction of the disconnected scCO$_2$ increases (Armstrong et al., 2014). This decrease in saturation along with a loss of internal connectivity resulted in a decrease in scCO$_2$ relative permeability. Consequently, the brine relative permeability has increased (as seen in Table 5.6). As a higher inlet flow rate was used in set 2 than set 1, the end-point imbibition scCO$_2$ relative permeability for set 1 was greater by a factor of about 9.0 (from 0.00092 to 0.00134). Moreover, the end-point imbibition relative permeability to brine was greater in set 2 (0.67) than in set 1 (0.576). Finally, it was observed that, for a given brine saturation, imbibition relative permeability was greater than its corresponding drainage value. This can be explained through certain pore-level displacement physics that are responsible for the re-distribution of brine and scCO$_2$ between cycles (Pini et al., 2013).

From Figures 5.6 and 5.7, it is clear that the drainage and imbibition fluid relative permeability curves have almost same range of brine saturation values (0.2–1.0 for drainage and 0.2–0.8 for imbibition). The predicted values of fluid relative permeability were observed to be quite similar (0.0–0.77). This is an indication of the reproducibility of the predicted numerical results.

5.2.1.3. Prediction of supercritical CO_2 capillary pressure

The fluid capillary pressure values were predicted using simulated fluid saturation and relative permeability values and the correlations proposed by Babchin et al. (2014). The predicted $scCO_2$ capillary pressures for sets 1 and 2 are presented in Table 5.7.

Table 5.7: $scCO_2$ capillary pressures predicted via simulation for sets 1 and 2.

Fluid injection velocity, m/s	$scCO_2$ Capillary pressure (Pa)	
	lowest	highest
0.026 (set 1 drainage)	38587	226231
0.03(set 1 imbibition)	36765	224409
0.035 (set 2 drainage)	46821	261378
0.035 (set 2 imbibition)	44998	259556

The predicted results were then analysed and compared with to a number of similar published works in order to gain a better understanding and interpretation. A comparison of capillary pressures for Berea sandstone reported by different researchers is presented in Table 5.8.

Table 5.8: Comparison of capillary pressures from the current study and others.

Fluid pair	Reference	Porosity, Ø	Permeability, K (mD)	Capillary pressure range, Pa
Air-brine	Tokunaga and Wan (2013)	-	-	0-8000
$ScCO_2$-brine				0-2500
CO_2-brine (Utsira formation, Canada, which has similar properties as Berea)	Soroush et al. (2013)	0.2-1.0 (brine)	0.36	0-20000
CO_2-brine	Al-Mehnali et al. (2015)	0.21	212	5000-100000
CO_2-brine	Li et al. (2015)	0.212	612	0-140000
CO_2-brine	Li X. (2015)	0.21	159	0-50000 (drainage) 0-34000 (imbibition)

A comparison of the predicted $scCO_2$ capillary pressures for different drainage and imbibition processes with those reported in the literature is presented in Figure 5.8.
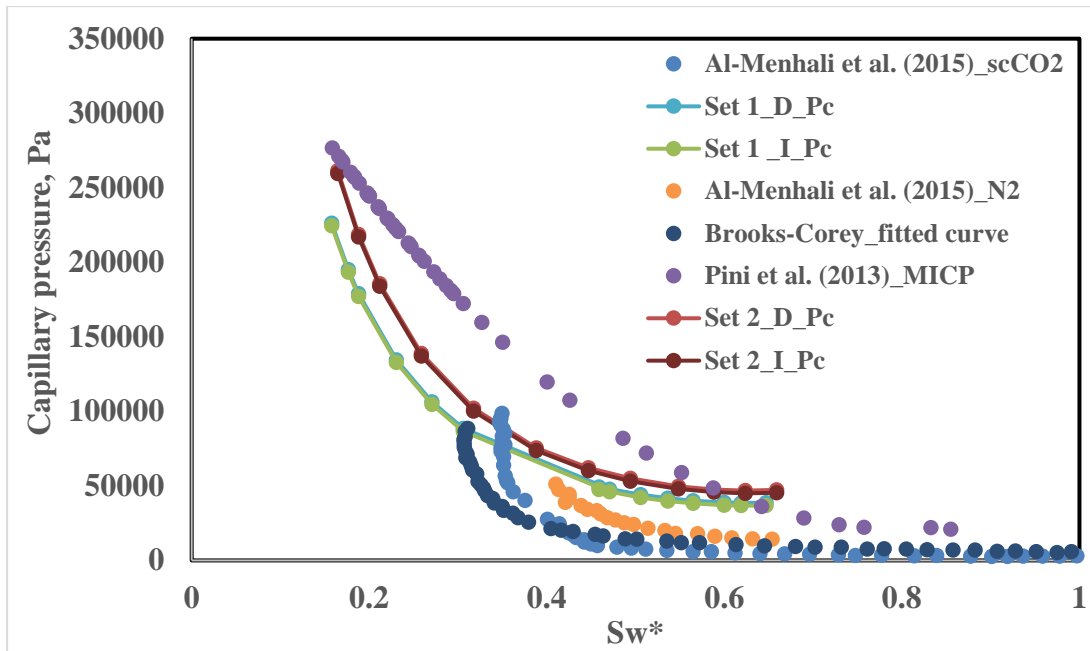
Figure 5.8: Comparison of predicted scCO₂ capillary pressure data with that of published works for drainage (D) and imbibition (I) processes.

At the beginning, when the capillary pressure is zero, brine was continuous. When the drainage process started, the saturation of brine started to decrease. As the brine saturation decreased, some portions of the brine phase disconnected from the bulk phase. In the course of time, when the external capillary pressure became too high, the remaining brine phase was disconnected (Anderson, 1987). This situation made the capillary pressure curve almost vertical, as depicted clearly in Figure 5.8.

During the imbibition process, the scCO₂ saturation decreased and scCO₂ gradually disconnected from the bulk phase (Anderson, 1987). This led to a rise in the capillary pressure until the curve was almost vertical, which can be observed in Figure 5.8.

As can be seen in Figure 5.8, the capillary pressure predicted via simulation for the drainage and imbibition processes was within the range reported by Pini et al. (2013) of 0–300,000 Pa. In addition, the predicted capillary pressure appears to be in very good agreement with the results presented by Krause et al. (2011), who used the TOUGH2 simulator for their study. They predicted capillary pressure within the range of 100–10,000,000 Pa for a CO₂-brine system in Berea sandstone. The predicted capillary pressures for the drainage processes (sets 1 and 2) in the current study were within the range reported by Pini and Benson (2013; 0–300000 Pa) based on mercury

injection capillary pressure (MICP) experiments. Hence, the range of predicted capillary pressures is consistent with reported data (Table 5.8).

5.2.1.4. Influence of inlet flow velocity and direction

A $scCO_2$ inlet velocity of 0.0017 m/s was in the numerical model of Berea sandstone drainage. This velocity was determined from the capillary number of 1.0×10^{-6}. The simulation of the drainage process was run with a contact angle of 45°. The simulation was terminated when the brine was drained by $scCO_2$ and the system reached a steady state. This phase distribution was used as an initial boundary condition for the imbibition processes. The imbibition processes were then simulated in two opposite directions with a contact angle of 85°. A brine injection velocity of 0.0003 m/s was used during the imbibition and reverse imbibition processes. This velocity was calculated from a capillary number of 1.0×10^{-5}. After completion of the simulation of imbibition processes, $scCO_2$ and brine relative permeability, and capillary pressure, were predicted using the models (Corey and Land models) discussed in Chapter 4.

The brine and $scCO_2$ relative permeability results for the drainage, imbibition and reverse imbibition processes are presented in Figures 5.9 and 5.10 for inlet velocities of 0.0017 m/s ($scCO_2$) and 0.0003 m/s (brine), respectively.
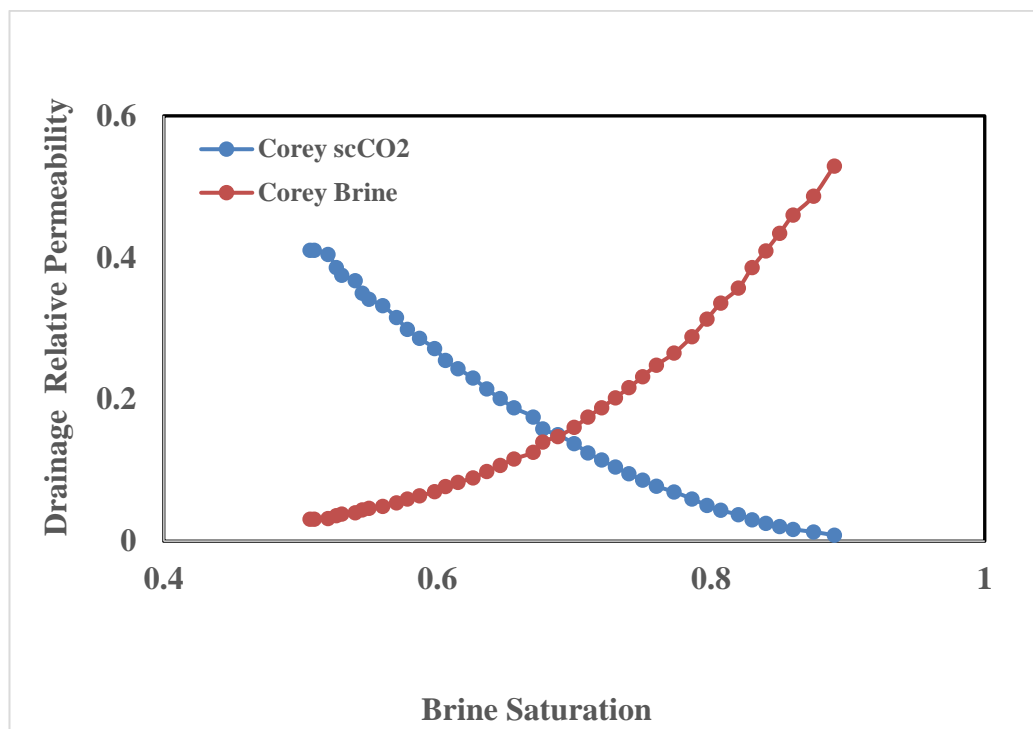
Figure 5.9: Drainage relative permeability vs brine saturation with an inlet $scCO_2$ velocity of 0.0017 m/s.
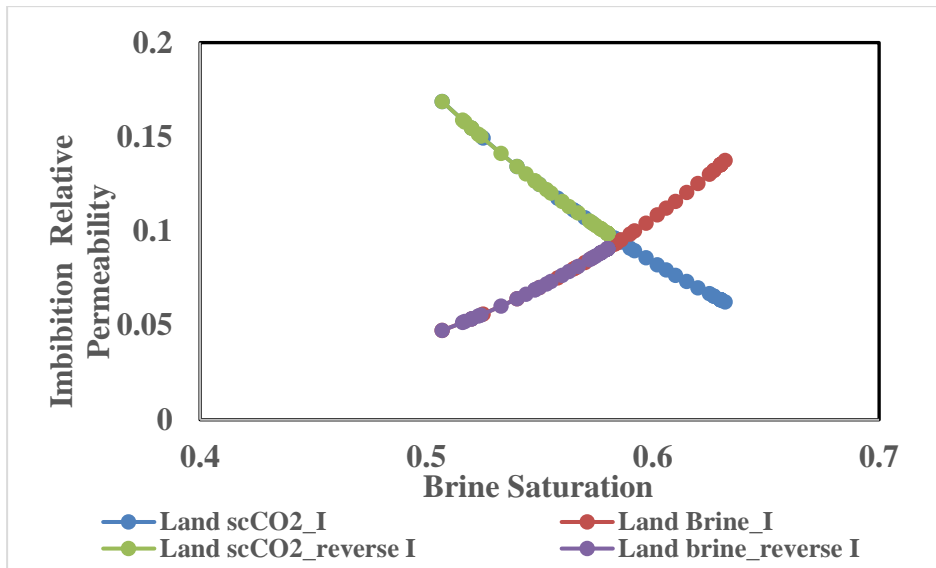
Figure 5.10: Imbibition relative permeability vs brine saturation for an inlet brine velocity of 0.0003 m/s for both flow directions.

While the relative permeability curves for the drainage process follow a normal trend as viewed in Figure 5.9, some changes can be observed due to changes in the inlet fluid flow direction (imbibition and reverse imbibition), as shown in Figure 5.10. The end-point fluid relative permeability values during reverse imbibition are lower than those during imbibition. Such behaviour is termed the *counter imbibition cycle*, which appears to be more typical for a weakly wetted system. For the imbibition cycle, the end-point value of $scCO_2$ relative permeability is in the range of 0.8 to 1 (Levine et al., 2011). Thus, a low value of relative permeability makes the counter-imbibition cycle ineffective.

No visible change was observed due to change in the inlet brine flow during the simulation of the imbibition process, which may be due to the small differences in inlet flow rates (0.0003 m/s for imbibition). The numerical results ($scCO_2$ capillary pressure) for the imbibition and reverse imbibition processes coincide with each other. Future work could investigate different brine flow rates to observe the effects of changes to inlet brine flow during imbibition.

The pore-scale numerical simulation was conducted utilizing a CFD-based simulator, ANSYS CFX, to simulate two-phase flow behaviour of supercritical carbon dioxide ($scCO_2$) and brine within the micropores of Berea sandstone. Emphasis was given on the prediction of two-phase flow parameters, fluid ($scCO_2$ and brine) relative

permeability and capillary pressure during drainage and imbibition. Micro-CT images of Berea sandstone were processed by the AVIZO image processor to capture the actual topography of the rock pore spaces (and network). Successful drainage and imbibition simulations were completed, and the saturations of brine and $scCO_2$ were obtained from the numerical model, which were then used to predict the said flow parameters using analytical models. The numerical model was successfully validated with various experimental and numerical works. The model was then used to perform a simulation of the $scCO_2$-brine system, predict the said two-phase flow parameters, and investigate $scCO_2$-brine flow behaviour and fluid distribution, and the influence of $scCO_2$ injection or inlet flow behaviour. The predicted capillary pressures were compared with those reported in the literature. It is demonstrated that the simulated results are in good agreement with those obtained via laboratory experiments and other approaches. The outcome of this study appears to be very promising, suggesting that CFD-based pore-scale simulation can be an alternative tool for predicting two-phase flow behaviour. This approach can be extended to larger-scale simulation studies.

Pore-scale numerical simulation will be the future of the industry, as this approach is relatively cheap and less time-consuming than laboratory experiments. It also provides the flexibility to conduct experiments with varying boundary conditions, and explore their impacts on the relative permeability outcomes. The key conclusions pertaining to this simulation study are summarized below:

- The trend of $scCO_2$ relative permeability as a function of brine saturation was observed to be sensitive to $scCO_2$ inlet (or injection velocity) and the direction of flow.
- The end-point $scCO_2$ relative permeability during reverse imbibition was lower than that during imbibition.
- Such behaviour is termed as the *counter imbibition cycle*, which appears to be typical for a weakly wetted system.
- A visible change was observed due to changes in the inlet brine flow during simulation of the imbibition process (Section 5.2.1). An increase in the inlet brine velocity appears to increase the saturation of $scCO_2$.
- Predicted capillary pressures were in good agreement with the literature which, in turn, proves the applicability of the proposed numerical model.

6. Chapter 6: Investigation of CO_2 trapping efficiency and sensitivity studies

Chapters 4 and 5 comprehensively discussed the numerical simulation and validation of models of two types of micro-porous rock: Ottawa F42 Sand Pack and Berea sandstone. This chapter discusses the sensitivity studies that were performed to investigate the influence of wettability and direction on $scCO_2$ trapping, and the capillary trapping efficiency of the $scCO_2$-brine imbibition process at the pore scale. Bentheimer sandstone is used to investigate capillary trapping efficiency. Part of this chapter is based on a SPE paper (SPE-192105-MS) recently presented at the SPE Asia Pacific Oil & Gas Conference and Exhibition, which was held from 23–25 October 2018 in Brisbane, Australia.

6.1. Background

The wetting properties of various reservoir rocks strongly influence the efficiency and security of carbon dioxide stored in deep saline aquifers. As discussed in Chapter 1, one of the main objectives of this PhD study is to investigate the trapping efficiency of $scCO_2$ in geological porous media. In this respect, this chapter focuses on the pore-scale displacement mechanism of $scCO_2$ under different wetting conditions and quantifies the effects of wettability and flow direction on $scCO_2$ trapping.

Al-Futaisi and Patzek (2003) conducted pore-scale numerical experiments on Bentheimer sandstone to calculate the relative permeability of non-aqueous phase liquid (NAPL) and described the spatial distribution of NAPL clusters. They also investigated the influence of wettability alternation on relative permeability and capillary pressure. Ramstad et al. (2010) conducted numerical simulations on the micro-pores in Bentheimer sandstone by Lattice Boltzmann Method (LBM). They computed drainage capillary pressure curves, which appeared to match well with their experimental results. However, their work under-predicted non-wetting-phase relative permeability at high wetting-phase saturation values. Ramstad et al. (2012) demonstrated a precise study of relative permeability based on micro-CT images of Bentheimer and Berea sandstones using LBM. Herring et al. (2013) conducted pore-scale experiments on Bentheimer sandstone to investigate the effect of initial non-wetting fluid topology on total non-wetting phase saturation (after imbibition). They found that a higher initial non-wetting connectivity state resulted in decreased non-

wetting phase capillary trapping in Bentheimer sandstone. Herring, et al. (2014) performed primary drainage experiments on Bentheimer sandstone and also quantified the volume and topology of $scCO_2$ in its micro-pores. Andrew et al. (2014) showed that the residual trapping method can be utilized to trap CO_2 for an effective carbon capture and storage (CCS) in different geological rock samples. They analysed pore-scale images of three carbonates and two sandstones including, Bentheimer. Peska et al. (2015) studied Bentheimer sandstone's mineral and physical properties through various methods (qualitative analysis, statistical 2D/3D reconstructions, laboratory methods, and stereological measurements). They focused on the impact of mineral composition on the petro-physical qualities and block-scale homogeneity of Bentheimer sandstone. Aghaei and Piri (2015) presented a new dynamic model to study various flow processes at the pore level in Bentheimer and Berea sandstones. They studied low interfacial tension (IFT) and high-viscosity two-phase flow processes through this new model and investigated the influence of high capillary numbers on residual oil saturation and relative permeability values. Krevor et al. (2015) reviewed the Intergovernmental Panel on Climate Change's (IPCC) special report on CCS and confirmed that trapped CO_2 saturation values will be at least 10% and, more typically, 30% of the pore volume of the geological rock sample in water-wet systems. Saenger et al. (2016) determined apparent hydraulic transport properties and effective elastic properties for Bentheimer sandstone through high-resolution three-dimensional X-ray microscopy. Moreover, they found that the porosity of Bentheimer sandstone is 22%.

It is clear from the above review that much research has been done on Bentheimer sandstone, especially to calculate its relative permeability, capillary pressure and residual saturation. However, only a few studies have been conducted from the CCS point of view. It is of great interest to understand the mechanism of CO_2 trapping and after-effects in the reservoir, for which detailed investigations are required. Nowadays, various CCS methods are applied to reduce environmental pollution due to CO_2 emissions. Good prediction of the CCS process within reservoirs requires an intensive understanding of wettability along with other properties, as wettability influences the shape of the capillary pressure and relative permeability curves and can alter the CO_2 trapping efficiency. In this view, this study considered Bentheimer sandstone for numerical modelling and simulation to better understand the mechanism of $scCO_2$

trapping during imbibition for different contact angles. The effects on CO_2 trapping efficiency were investigated during imbibition by changing the direction of brine flow at the inlet and varying the contact angles. This chapter focuses on increasing understanding of the CO_2 distribution footprint, and the effects of wetting properties and brine flow direction with $scCO_2$ injection during the imbibition process.

6.1.1. Description of the Numerical Model

Similar to Ottawa Sand Pack 42 and Berea sandstone, Bentheimer sandstone images were processed to separate the pore spaces using AVIZO, which was then used to create surface and volume meshes and a numerical model using ANSYS ICEMCFD. The created numerical model was then used with the CFD-based simulator ANSYSCFX. Figure 6.1 shows the pore spaces of the Bentheimer sandstone while Figure 6.2 shows the volume mesh used for numerical simulation.
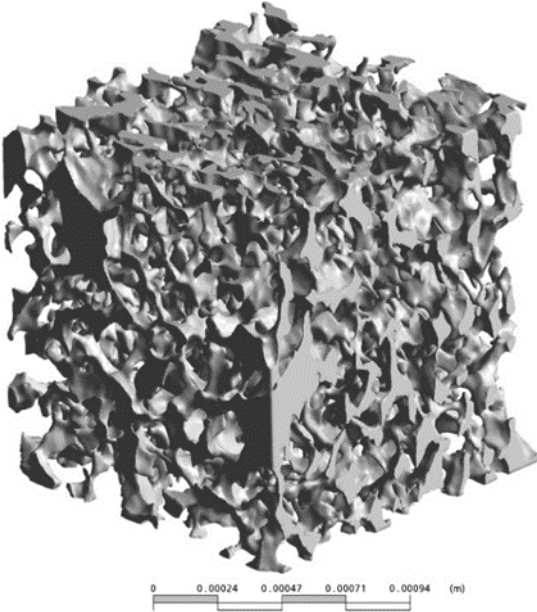
Figure 6.1: Pore spaces of Bentheimer sandstone processed by AVIZO.

| 0 | 0.00024 | 0.00047 | 0.00071 | 0.00094 | (m) |
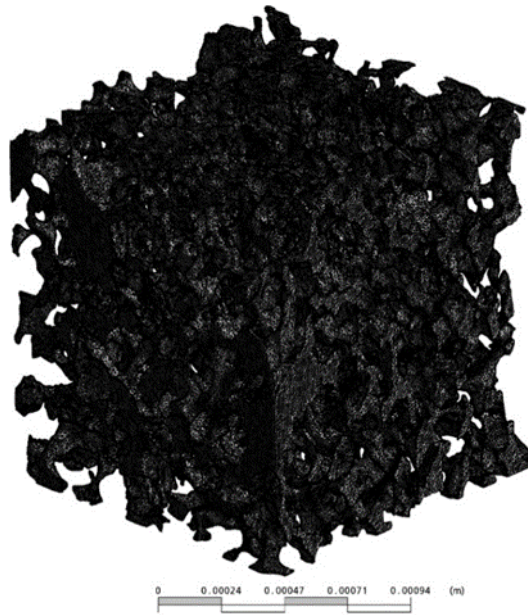
Figure 6.2: Numerical model showing the volume mesh of Bentheimer sandstone.

As per the previous model, ANSYSCFX was used to solve full transient Navier-Stokes equations following the Eulerian-Eulerian multiphase flow approach. A free surface flow model (Brackbill et al., 1992; Ahmed & Iglauer, 2012) was used for the interphase momentum transfer to calculate the pressure gradient at the interface between the two phases and to track the position of the interface accurately (Jahan et al., 2016). The role of surface tension was incorporated as a continuum surface force in the free surface flow model. The value of surface tension considered in this study is 0.036 N/m, which is considered typical for CCS systems (Chalbaud et al., 2009).

For the first imbibition process, the initial saturation of $scCO_2$ was obtained from the drainage process. For this, the Bentheimer sample was saturated with brine. The $scCO_2$ was injected (as inlet velocity) and the pressure was monitored. The injection of $scCO_2$ ceased when the pressure appeared to be constant and the phase distribution returned to the initial condition used for the imbibition process.

The inlet boundary condition for the imbibition processes was specified with a uniform $scCO_2$ velocity of 0.026 m/s, which was calculated based on a capillary number of 1.5×10^{-3}. The outlet boundary condition was set opposite to the inlet with a zero relative pressure, so the pressure predicted at the inlet was equal to the pressure drop between the sample inlet and outlet. All the other faces of the Bentheimer sandstone were

assumed to be impermeable. This condition was achieved by applying no-slip wall boundary conditions. The convergence criterion was set to 10^{-5}. All simulations were run with a time-step size of 0.01 s based on a Courant number. The Courant number expresses the stability or variation of the flow. Table 6.1 shows the porosity and absolute permeability values used, while Table 6.2 shows the fluid properties considered in the simulation.

Table 6.1: Porosity and permeability values used in the model.

Permeability, K (Darcy)	Method of porosity determination	Porosity, Ø
1.6 from Peksa, Wolf, and Zitha (2015)	From AVIZO	0.222
1.9 from Andrew, Bijeljic and Blunt (2014)	From Peksa, Wolf, and Zitha (2015)	0.24
	From Saenger et al. (2016)	0.22

Table 6.2: Fluid properties considered in the simulation model.

Fluid	Density ρ (kg/m³)	Viscosity μ (Pa.s)	Surface tension σ (Nm^{-1})
scCO$_2$	469	0.000021	0.036
Brine	1071	0.001193	

6.1.2. Estimation of normalized residual and trapped scCO$_2$ saturation (S_{ot}*) for Bentheimer sandstone

The numerical results obtained during the simulation of imbibition and reverse imbibition (opposite direction) processes for different contact angles are presented in Table 6.3. The results appear to be quite interesting. The residual scCO$_2$ saturation for reverse imbibition processes was higher (more than double) that for the imbibition processes (Table 6.3). However, the normalized trapped scCO$_2$ saturation for reverse imbibition processes was lower than that obtained for imbibition. The model, including the process of calculating residual scCO$_2$ saturation and normalized trapped scCO$_2$ saturation, is similar to that for Ottawa F42 Sand Pack (provided in Appendix C). The normalized total residual saturation of scCO$_2$ is defined as the sum of the normalized free scCO$_2$ saturation (S$_o$F*); and the normalized trapped scCO$_2$ saturation (S$_o$t*; Land, 1968). Land (1968) suggested that the maximum value of S$_o$t* will be achieved if S$_o$F* is equal to zero. Figure 6.3 was constructed by following Land's assumption and represents normalized trapped scCO$_2$ saturation (S$_o$t*) vs initial scCO$_2$ saturation for

various imbibition processes. A sample calculation showing the process of calculation for S_ot* (as shown in Figure 6.3 and Table 6.3) is provided in Appendix C.

Table 6.3: Numerical simulation results at the end of various imbibition processes.

Imbibition cycles	Residual scCO$_2$ saturation (after simulation for 40 s)	Normalized trapped scCO$_2$ saturation (S_ot*)
Imbibition at 100°	0.12	0.11
Imbibition at 110°	0.14	0.112
Reverse imbibition at 100°	0.28	0.04
Reverse imbibition at 110°	0.26	0.04

It is clear from Figure 6.3 that the reverse imbibition processes had almost the same trend as that presented by Land. It is to be noted that in Land's work, the value of coefficient C was 5. However, the value of C in this work is considered to be 5.57. The correlation used to calculate Land's coefficient C, including a sample calculation, is provided in Appendix C. Moreover, both reverse imbibition processes resulted in lower values of normalized trapped scCO$_2$ saturation as compared to imbibition processes (for contact angles of 100° and 110°), which is consistent with the results presented in Table 6.3. Therefore, the low value of normalized trapped scCO$_2$ saturation (in reverse imbibition) reveals a higher amount of normalized free scCO$_2$ saturation, which is not preferable for an effective CCS system.
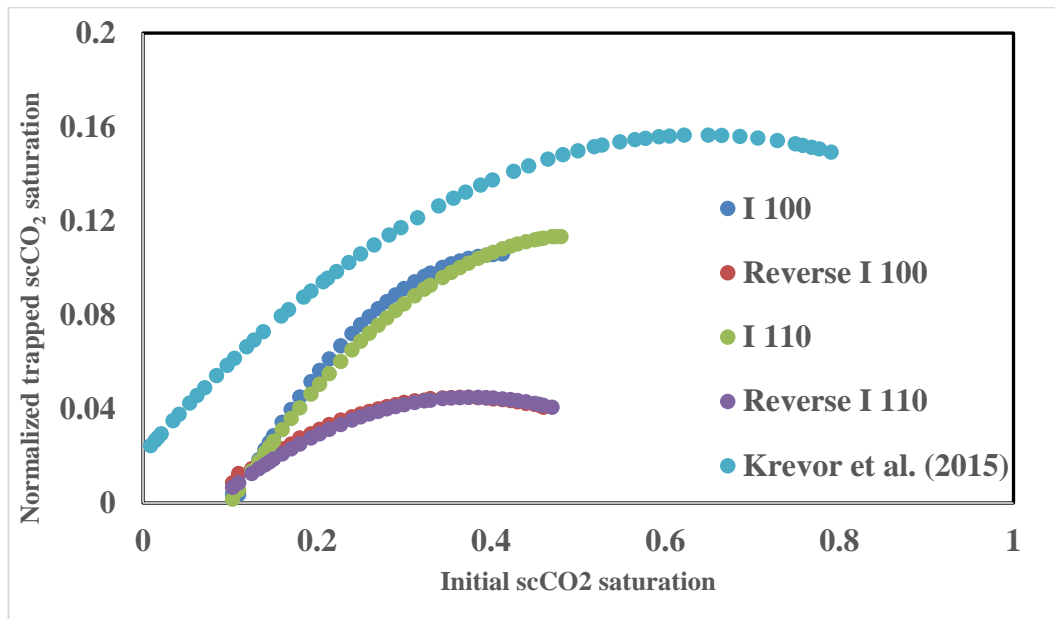
Figure 6.3: For various imbibition processes, normalized trapped scCO$_2$ saturation (S_ot^*) is plotted as a function of initial supercritical CO$_2$ saturation.

Figure 6.4 shows the variation in pressure drop as a function of simulation time for various imbibition processes. For all imbibition processes, the first point represents the threshold pressure, which is the least pressure at which brine starts to invade the Bentheimer sandstone. This threshold pressure is dependent on the curvature of the pore walls and the mineralogy of the solid surfaces of the rock sample (Blunt, 1998). Both reverse imbibition processes showed gradual and steady increases until they reached the highest values (3,759 Pa and 3,443 Pa for contact angles of 100° and 110°, respectively). However, the imbibition processes showed quite fluctuating increases until they reached the highest pressure drop values (2,848 Pa and 3,000 Pa for contact angles of 100° and 110°, respectively). For all imbibition processes, after 20 s, pressure drop values appeared to be almost equal, which indicates that the processes reached steady-state conditions.
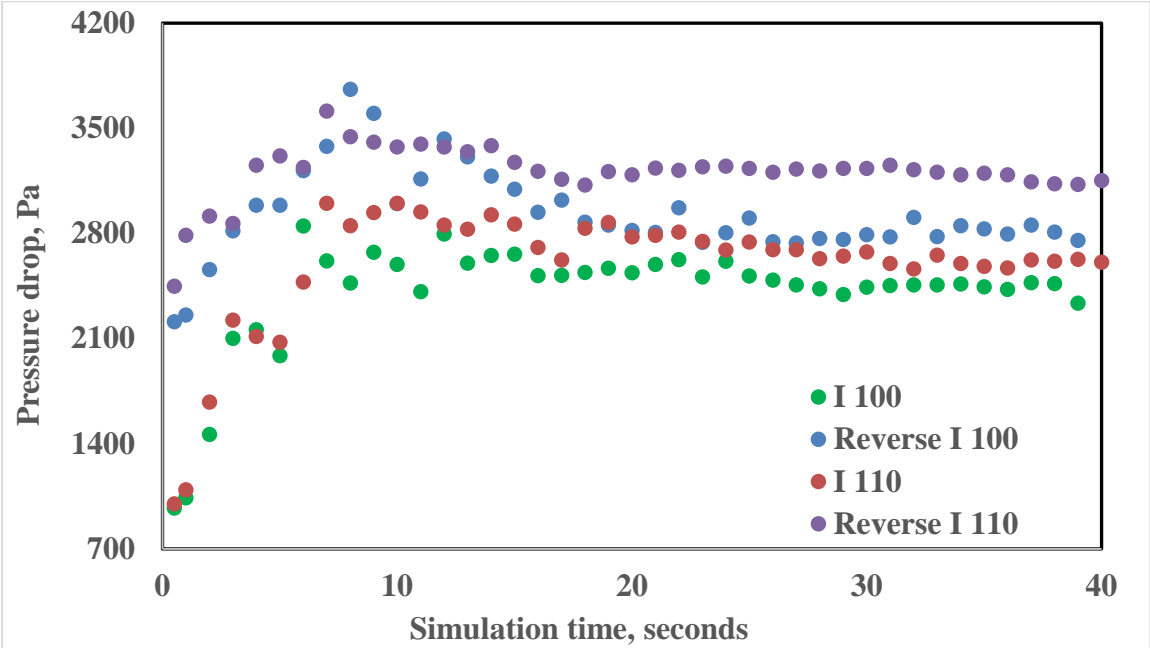
Figure 6.4: Variation in pressure drop as a function of simulation time for various imbibition processes.

Analysis of the results discussed above shows that, although residual $scCO_2$ saturation increased in the reverse imbibition processes, the amount of normalized trapped $scCO_2$ decreased compared to in the imbibition processes. Therefore, trapped $scCO_2$ is one of the important parameters for determining the trapping efficiency of a CCS system. Variations in pressure drop were observed for different imbibition processes and the

results were found to be consistent with the general pressure drop pattern during imbibition. This method of two-phase flow analysis is cost-effective and takes less time than traditional laboratory-based experiments. Hence, it can be considered a good tool for assessing reservoirs and the effectiveness and economics of CCS systems.

6.2. *Sensitivity study in Ottawa F42 Sand Pack*

The results of the numerical simulations in this research can be used to predict fluid flow performance within reservoirs. In turn, flow performance is a strong function of fluid saturation and, thus, relative permeability. Interpretation of relative permeability and capillary pressure (which can be evaluated from estimated fluid saturation and relative permeability values) is essential for an effective and efficient CCS system within a reservoir. In this regard, some sensitivity studies will greatly assist.

The objectives of this sensitivity study are:

- To investigate $scCO_2$ fractional flow and normalized trapped $scCO_2$ saturation, and evaluate $scCO_2$ trapping capacity within the pore spaces of Ottawa F42 Sand Pack under different flow conditions (sets 1 and 2).
- To build an interactive procedure that can be used to predict the performance of the different flow conditions (by varying flow rates or petro-physical properties).
- To analyse and compare the results with those of published studies.

This section discusses the evaluation of $scCO_2$ trapping capacity for Ottawa F42 Sand Pack based on similar numerical studies, following the approaches discussed in Section 6.1 and Appendix C. The factors influencing the performance of trapping capacity in Ottawa F42 Sand Pack are also elaborated. The study was carried out based on two sets of input data, which are shown in Table 6.4.

Table 6.4 Input data considered in each set.

Variable	Set 1	Set 2
Inlet velocity (m/s)	0.026 (drainage), 0.03 (imbibition	0.035 (drainage and imbibition)
Contact angle (degree)	5° (drainage), 45° (imbibition	5° (drainage), 30° (imbibition)
Porosity	0.035	
Permeability, Darcy	42	

6.2.1. Fractional flow of scCO₂

The estimated $scCO_2$ and brine relative permeability values determine by numerical simulation were used to determine the fractional flow of $scCO_2$ (f_{scCO_2}) using Equation 6.1:

$$f_{scCO_2} = \frac{\frac{k_{scCO2}}{\mu_{scCO2}}}{\frac{k_{scCO2}}{\mu_{scCO2}} + \frac{k_{brine}}{\mu_{brine}}} \tag{6.1}$$

Where,

k_{rscCO_2} = scCO₂ relative permeability

μ_{scCO2} = scCO₂ viscosity, Pa.s

k_{brine} = brine relative permeability

μ_{brine} = brine viscosity, Pa.s.

The estimated scCO₂ fractional flow, f_{scCO_2}, as a function of sCO₂ saturation is plotted in Figure 6.5 for set 1 (brine inlet velocity = 0.03 m/s), and set 2 (brine inlet velocity = 0.035 m/s) during imbibition.

As the mobility ratio, $\frac{\frac{k_{brine}}{\mu_{brine}}}{\frac{k_{scCO2}}{\mu_{scCO2}}}$, is very low, at 0.00023, for the scCO₂-brine system, the corresponding efficiency of the imbibition processes is very high. This resulted in no inflection point (no S-shape) in the fractional flow curve, as shown in Figure 6.5.
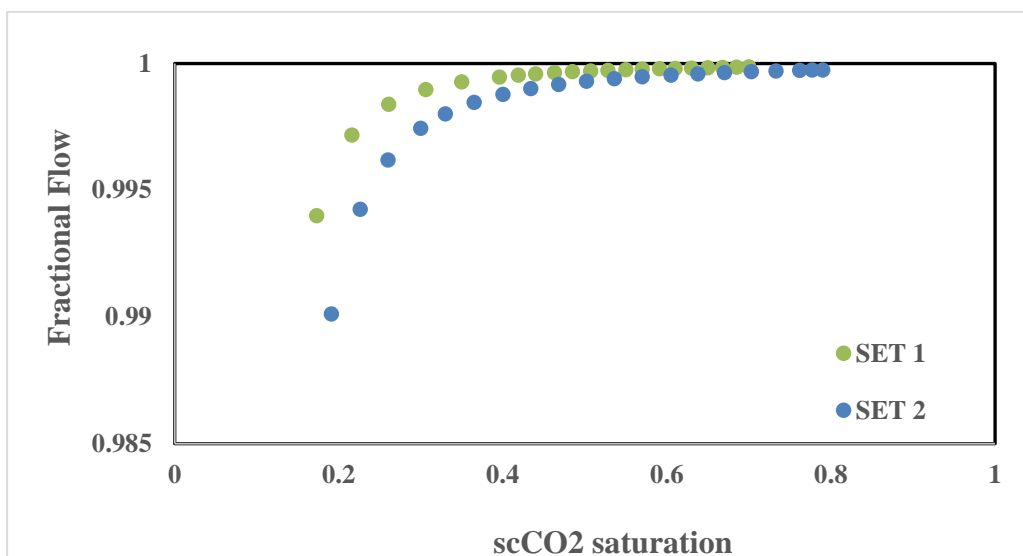
Figure 6.5: Fractional flow of scCO₂ as a function of scCO₂ saturation in Ottawa F42 Sand Pack.

As seen in Figure 6.5, the range of values for fractional flow vary from 0.99 to 1.0, which implies that more than 99% of the $scCO_2$ within the pore spaces of the Ottawa F42 Sand Pack were displaced by brine. This situation makes Ottawa F42 Sand Pack less favourable for use as an effective CCS system.

6.2.2. Normalized trapped $scCO_2$ saturation

The normalized trapped $scCO_2$ saturation in Ottawa Sand Pack 42 was estimated via simulation and the approaches described in Appendix A, and plotted as a function of initial $scCO_2$ saturation in Figure 6.6 for set 1 (brine inlet velocity = 0.03 m/s), and set 2 (brine inlet velocity = 0.035 m/s).
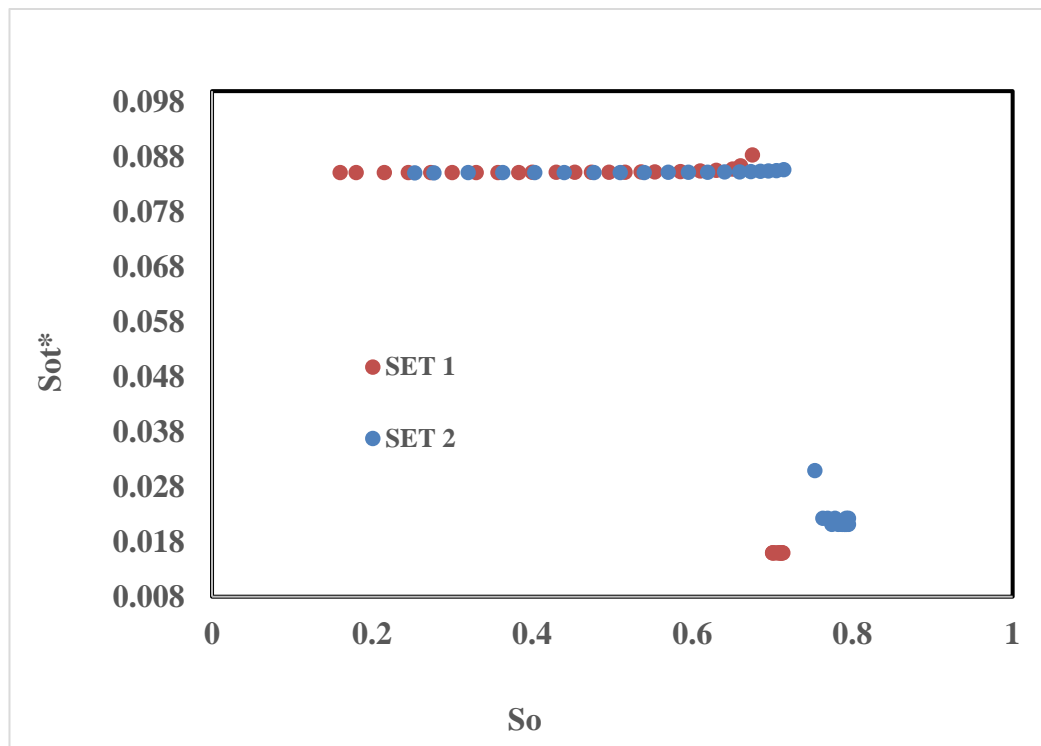
Figure 6.6: Normalized trapped $scCO_2$ saturation (S_{ot}^*) as a function of initial $scCO_2$ saturation for Ottawa F42 Sand Pack.

The normalized trapped $scCO_2$ saturation values presented in Figure 6.6 can be explained by the four trapping mechanisms (explained in Chapter 2) that act at different rates simultaneously. During the drainage and imbibition stages, capillary forces help displace CO_2 and various proportions of CO_2 are trapped within the pore spaces. The amount of trapped $scCO_2$ within the pore spaces is dependent on several factors (for instance, relative amounts of dissolved and free CO_2, the structure of the

pore network of the reservoir rocks, initial CO_2 saturation, CO_2 dissolution into nearby brine, contact angle between $scCO_2$ and brine, and inlet fluid flow rate).

These factors make the evaluation of the CO_2 storage capacity (obtained from trapped $scCO_2$ saturation) very complex. However, for the Ottawa F42 Sand Pack, which is a highly porous material, the normalized trapped $scCO_2$ saturation values were similar for both sets. This is clear from Figure 6.6, which reveals that changes in the inlet brine flow rate (a parameter for sensitivity analysis for this chapter) has no significant effect on normalized trapped $scCO_2$ saturation within the pore spaces of Ottawa F42 Sand Pack.

6.2.3. Evaluation of scCO₂ capillary trapping capacity

Supercritical CO_2 ($scCO_2$) capillary trapping capacity (C_{trap}) is defined as the product of porosity and the residual saturation of $scCO_2$. It is a useful measure of the amount of $scCO_2$ stored securely per unit rock volume within a porous geological system (reservoirs). It is dependent on the initial $scCO_2$ saturation and the rock characteristics (i.e. porosity and permeability; Iglauer et al., 2009). However, the $scCO_2$ capillary trapping capacity of Ottawa Sand Pack was estimated from simulation results following the approaches described in Appendix C (Equation C.2). The results are presented in Table 6.4 for set 1 (brine inlet velocity = 0.03 m/s, contact angle = 45°), and set 2 (brine inlet velocity = 0.035 m/s, contact angle = 30°).

Table 6.5: Supercritical CO₂ capillary trapping capacity

Porosity	Set	Residual scCO₂ saturation	scCO₂ capillary trapping capacity (C_{trap}), %
0.354 (from literature)	Set 1 (v=0.03 m/s, θ=45°)	0.05	1.77
0.28 (from Avizo)			1.40
0.354 (from literature)	Set 2 (v=0.035 m/s, θ =30°)	0.0515	1.82
0.28 (from Avizo)			1.44

Like trapped $scCO_2$ saturation within the pore spaces of geological rocks, the $scCO_2$ capillary trapping capacity (C_{trap}) depends on the inlet or injection velocity, wettability (contact angle), residual $scCO_2$ saturation and the characteristics of the rock (for example, porosity and permeability), as can be seen in Table 6.5. For set 1 (brine inlet

velocity = 0.03 m/s, contact angle = 45°), the estimated capillary trapping capacity is about 1.77%, whereas for set 2 (brine inlet velocity = 0.035 m/s, contact angle = 30°), the capillary trapping capacity is estimated to be 1.82%, which suggests that a decrease in contact angle with a higher brine inlet velocity during imbibition increases the capillary trapping capacity. The trapping capacity also depends on the rock characteristics (i.e. porosity and permeability). As expected, the higher porosity (0.035) and permeability (±42 Darcy) result in higher capillary trapping capacity for any injection velocity (Table 6.5).

6.3. Sensitivity study in Berea sandstone

In this section, a sensitivity analysis of Berea sandstone is presented. Two graphs are presented: $scCO_2$ fractional flow vs $scCO_2$ saturation, and normalized trapped $scCO_2$ saturation vs initial $scCO_2$ saturation. Also, $scCO_2$ trapping capacity values are presented for different flow sequences.

6.3.1. Fractional flow of $scCO_2$

Fluid relative permeability values estimated by numerical simulation were used to determine $scCO_2$ fractional flow for Berea sandstone. The estimated $scCO_2$ fractional flow is plotted as a function of initial $scCO_2$ saturation in Figure 6.7 for the two sets (set 1: brine inlet velocity = 0.03 m/s at θ = 45°; set 2: brine inlet velocity = 0.035 m/s at θ = 30°), imbibition at 85° (brine inlet velocity = 0.0003 m/s), and counter-imbibition at 85° (brine inlet velocity = 0.0003 m/s) during imbibition.
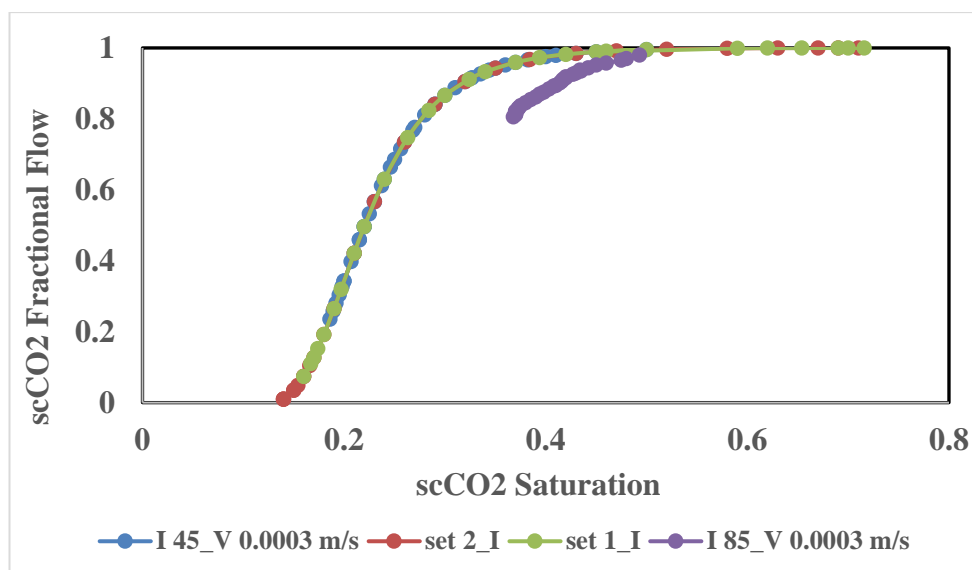
Figure 6.7: $scCO_2$ fractional flow vs $scCO_2$ saturation for Berea sandstone.

In Figure 6.7, the steep slope indicates there was a sharp rise for set 1 and 2 (Qi et al., 2008). This rise was due to the movement of brine. In other words, this situation indicates rapid trapping of $scCO_2$. Furthermore, imbibition at 85° showed a less steep curve than the other three, but this distribution (imbibition at 85°) cycle gave the highest amount of trapped $scCO_2$, which can be seen in Table 6.6. It means that this particular imbibition cycle will be more favourable than the other three in terms of CCS efficiency. Table 6.6 provides the porosity and permeability values (Talabi, 2008).

If the $scCO_2$ fractional flow values from Figure 6.7 are compared with fractional flow values from the literature (Krevor et al., 2012; Table 6.7), it can be observed that the counter-imbibition cycle results are quite close to those of published work.

Table 6.6: Fractional flow of scCO₂ for Berea sandstone.

Flow sequences	Fractional flow of scCO₂ (at the end of imbibition)	Porosity	Permeability, K (mD)
Set 1 (imbibition at 45°)	0.07 (scCO₂ saturation=0.16)		
Set 2 (imbibition at 30°)	0.01 (scCO₂ saturation=0.14)	0.196	1286
Imbibition at 85°	0.24 (scCO₂ saturation=0.19)		
Counter imbibition at 85°	0.81 (scCO₂ saturation=0.37)		

Table 6.7: Berea sandstone data from Krevor et al. (2012).

Fractional flow	CO₂ saturation	Porosity	Absolute permeability, K (mD)
0.1	0.04		
0.3	0.09		
0.5	0.12	0.221	914
0.7	0.20		
0.9	0.26		

6.3.2. Normalized trapped scCO₂ saturation

In this section, Figure 6.8 represented normalized trapped $scCO_2$ saturation vs initial $scCO_2$ saturation for different flow sequences (the same sequences which were presented in the previous section) for Berea sandstone. Table 6.8 shows various $scCO_2$ saturation values for different imbibition cycles.
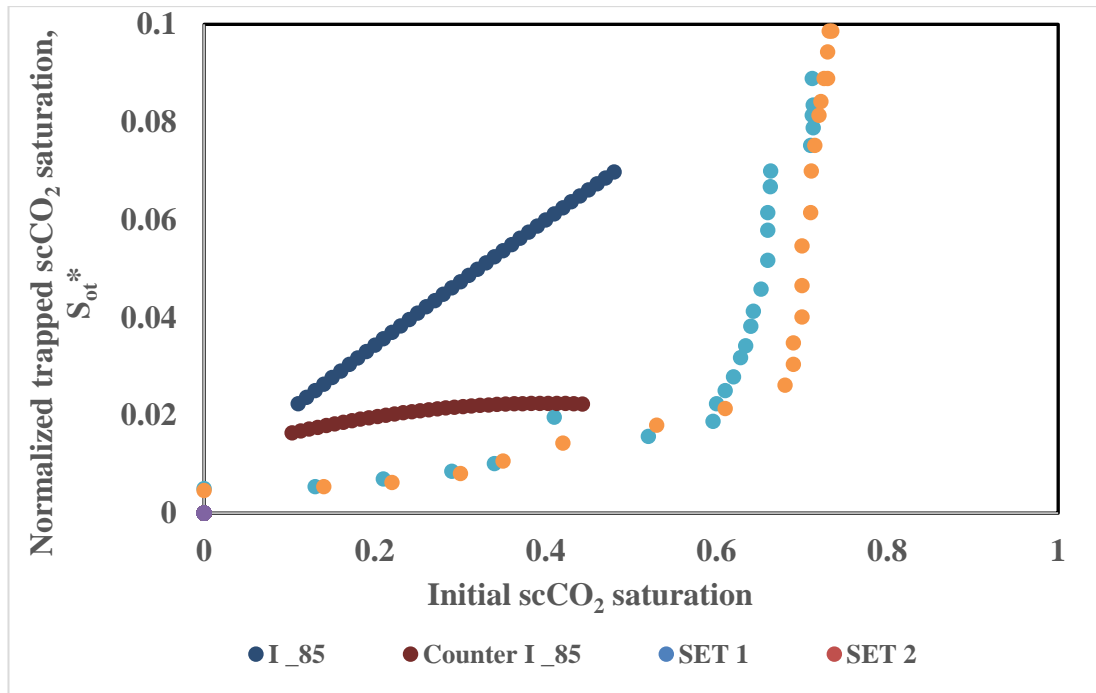
Figure 6.8: Normalized trapped scCO₂ saturation vs initial scCO₂ saturation for Berea sandstone.

In Figure 6.8, the counter-imbibition curve is less steep than the concurrent imbibition curve. As the fluid relative permeability values are lower in the counter-imbibition cycle than the imbibition cycle, this low value contributes to lower CO_2 storage capacities (Levine et al., 2011). Moreover, it can be easily observed that, for the counter-imbibition cycle, values of normalized trapped scCO₂ were almost the same for different scCO₂ values. This reveals that the counter-current imbibition cycle is less favourable than the concurrent cycle.

In Figure 6.8, the set 2 imbibition cycle provided the best scenario of all regarding scCO₂ trapping. A small increase in brine velocity (from 0.03 m/s to 0.035 m/s) was used in this cycle, which likely added to this high value. This condition confirms that the inlet brine flow has a considerable effect on the normalized trapped scCO₂ saturation. However, imbibition at 85° showed a sharp rise in normalized trapped scCO₂ than counter-imbibition at 85°. However, this range of normalized trapped scCO₂ saturation values was limited to within 0.0–0.48. This situation shows the necessity of running these imbibition cycles for longer periods to investigate whether there will be an increase in normalized trapped scCO₂ over time. This may become a subject of future research.

Table 6.8: Numerical simulation results at the end of various imbibition processes.

Imbibition cycle	Residual scCO$_2$ saturation	Normalized trapped scCO$_2$ saturation (S_0t^*)
Imbibition at 45° (set 1)	0.71	0.07
Imbibition at 30° (set 2)	0.74	0.01
Imbibition at 5°	0.48	0.24
Reverse imbibition at 85°	0.44	0.81

From Table 6.8, it can be seen that the set 2 imbibition process provided the highest residual scCO$_2$ saturation. However, counter-imbibition provided the highest normalized trapped scCO$_2$ saturation with the lowest residual scCO$_2$ saturation. This explanation was provided through a calculation process that was stated before. The calculation processes of residual scCO$_2$ saturation and normalized trapped scCO$_2$ saturation are provided in Appendixes A and C. As explained before, the normalized total residual scCO$_2$ saturation is defined as the sum of normalized free scCO$_2$ saturation (S_{oF}^*) and normalized trapped scCO$_2$ saturation (S_{ot*}; Land, 1968). Land (1968) suggested that the maximum amount of Sot^* will be achieved if S_{oF}^* is equal to zero. Figure 6.8 was constructed by following Land's assumption.

6.3.3. Evaluation of scCO$_2$ capillary trapping capacity

In this section, Table 6.9 provides various scCO$_2$ capillary trapping capacity values for various flow sequences (set 1: brine inlet velocity = 0.03 m/s at θ = 45°; set 2: brine inlet velocity = 0.035 m/s at θ = 30°; imbibition at 85° with brine inlet velocity = 0.0003 m/s; and counter-imbibition at 85° with brine inlet velocity = 0.0003 m/s).

Table 6.9: Supercritical CO$_2$ capillary trapping capacity

Porosity	Number of sets	scCO$_2$ residual saturation	scCO$_2$ capillary trapping capacity (C_{trap}), %
0.23 [from Øren et al. (2003)]	Set 1	0.16	3.70
0.154 (from Avizo)			2.50
0.23 [from Øren et al. (2003)]	Set 2	0.14	3.20
0.154 (from Avizo)			2.20
0.23 [from Øren et al. (2003)]	Imbibition at 85°	0.37	8.50
0.154 (from Avizo)			5.68
0.23 [from Øren et al. (2003)]	Counter imbibition 85°	0.42	9.66
0.154 (from Avizo)			6.50

In Table 6.9, it can be seen that by using the porosity values from Øren et al. (2003), for set 1, the calculated capillary trapping capacity is about 3.7%. For set 2, the value of capillary trapping capacity is about 3.2%. These values infer that the decrease in the contact angle from set 1 to set 2 (from 45° to 30°) during imbibition resulted in a decrease in $scCO_2$ residual saturation. This decrease was followed by a decrease in the capillary trapping capacity (Blunt, 1998).

If porosity values from Avizo are considered, then the predicted $scCO_2$ trapping capacity is less than those predicted with the porosity values from Øren et al. (2003).

Table 6.9 shows the highest $scCO_2$ capillary trapping capacity, which was achieved for the counter-imbibition cycle at 85°. However, from Figure 6.8, it can be seen that the counter-imbibition cycle at 85° provided less normalized trapped $scCO_2$ than that from the imbibition cycle at 85°.

The imbibition cycle at 85° appears to provide the best effective $scCO_2$ capillary trapping capacity of all (8.5%), which can be observed from Table 6.9. This value is optimal for effective CO_2 storage for porosity = 0.20 (Wulling et al., 2009). So, an increase in the contact angle and decrease in flow rate can result in higher $scCO_2$ capillary trapping capacity, which may be a good subject for future numerical and experimental works on Berea sandstone.

7. Chapter 7: Conclusion, and recommendation

7.1. Conclusions

This research work conducted scCO$_2$-brine numerical simulations of the micro-pores of Ottawa F42 Sand Pack, Berea sandstone and Bentheimer sandstone for various drainage and imbibition processes. Micro-CT images of various reservoir rocks were used to extract details of the pore networks. Image processing software (AVIZO) and various modules of a CFD simulator (ANSYS) were utilized for this purpose. One of the main purposes of this study was to understand scCO$_2$-brine flow patterns within these geological samples via numerical simulation. Then, those numerical models were utilized to predict various rock and fluid properties (fluid relative permeability, scCO$_2$ capillary pressure, etc.). After these stages, numerical results were discussed regarding the effect of inlet brine flow rate (during imbibition cycles) and wettability (in terms of contact angles) on fluid relative permeability, scCO$_2$ capillary pressure and scCO$_2$ capillary trapping capacity to aid the design of cost-effective CCS systems. Thus, a workflow involving image segmentation, volume mesh generation, assignment of contact angles and simulations of pore spaces of sand pack (Ottawa F42 Sand Pack) and sandstones (Berea and Bentheimer) are presented in this work.

• A series of numerical simulations of the micro-pores of Ottawa F42 Sand Pack and Berea sandstone were performed for drainage and imbibition cycles to establish a simple set of benchmark results for validation of the numerical modelling of an oil-brine system. Afterwards, the models were used to predict fluid relative permeability, scCO$_2$ capillary pressure and scCO$_2$ capillary trapping capacity in a scCO$_2$-brine system. Estimation of these quantities are hardly possible without having the simulations results from imbibition processes. Moreover, the effect of the inlet brine flow rate on fluid relative permeability and scCO$_2$ capillary pressure were not assessed without the imbibition processes. Thus, the numerical simulation studies serve as valuable steps towards the development of models that can predict various properties of more complex reservoir rocks with scCO$_2$-brine systems, for which direct experimental data is unavailable.

1) Fluid relative permeability was calculated by using end-point fluid saturations (calculated by numerical simulation) and compared with other numerical and experimental results. The results agreed well with those of similar published work. In this work, it was observed that an increase in the inlet fluid flow rate resulted in a very small increase in fluid relative permeability.

2) Based on the estimated fluid relative permeability values, an approach was presented to determine $scCO_2$ capillary pressure in the Ottawa F42 Sand Pack. Moreover, the effect of the inlet fluid flow rate on $scCO_2$ pressure was observed. As predicted, the capillary pressures at various inlet fluid flow rates were quite close to each other.

3) As the Ottawa F42 Sand Pack is highly porous (porosity = 0.035, permeability = 42 Darcy), change in the inlet fluid flow rate had an insignificant effect on fluid saturation values.

4) For $scCO_2$ fractional flow sensitivity studies within the pore spaces of the Ottawa F42 Sand Pack, the estimated $scCO_2$ fractional flow curves exhibited no inflection points. Also, the Ottawa F42 Sand pack is unfavourable for CCS because it's very high values of $scCO_2$ fractional flow (0.99–1.0) indicate that most $scCO_2$ is displaced by brine.

5) The $scCO_2$ capillary trapping capacity (which is dependent on the residual $scCO_2$ saturation) of the Ottawa F42 Sand Pack is quite low (1.77 %) at an initial inlet brine flow velocity of 0.03 m/s (for set 1). When the flow rate was increased slightly (to 0.035 m/s, set 2), the capillary trapping capacity increased to 1.82%. This explains that increases in flow rate increase capillary trapping capacity. However, this was not clearly observed in this work. Thus, low residual $scCO_2$ saturation led to poor capillary trapping efficiency. Such low residual $scCO_2$ saturation may occur due to very efficient and quick displacement of $scCO_2$ by brine or low levels of normalized trapped $scCO_2$ saturation during imbibition, which can be assigned to the interfacial tension of the $scCO_2$-brine system. This, in turn, made the snap-off trapping mechanism less important as a principal trapping mechanism during drainage and imbibition cycles.

6) Then, the numerical study was extended to predict the effect of the inlet brine flow rate on fluid relative permeability and $scCO_2$ capillary pressure during simulation of imbibition. No remarkable change was observed due to changes

in the inlet brine flow rate during these simulations. Much higher inlet brine flow rates may be used to investigate such change, which could be a subject of future work.

7) The normalized trapped $scCO_2$ residual saturation, $scCO_2$ fractional flow and $scCO_2$ capillary trapping capacity were predicted with the help of fluid residual saturation values obtained from numerical simulation studies. Counter-imbibition at $85°$ provided the highest normalized trapped $scCO_2$ saturation with the lowest residual $scCO_2$ saturation. In terms of $scCO_2$ capillary trapping capacity, the results showed that decreases in flow rate and increases in contact angle may increase $scCO_2$ capillary trapping capacity.

8) For Bentheimer sandstone, it was observed that the residual $scCO_2$ saturation in counter-imbibition processes was higher (more than double) that for imbibition processes. However, the normalized trapped $scCO_2$ saturation for counter-imbibition processes was lower than that for imbibition processes. This situation shows that a higher normalized free $scCO_2$ saturation is not preferable for CCS systems. Changes in contact angle and inlet fluid flow rates may change this observation, which is a subject for future numerical experiments.

9) Similar to the Ottawa F42 Sand pack experiments, the relationship between threshold pressure and pressure drop as a function of simulation time during various imbibition processes within the pore spaces of Bentheimer sandstone was determined. Both counter-imbibition processes revealed a steady rise, and imbibition processes revealed a quite fluctuating rise until the highest pressure drop was reached.

7.2. *Significance of this study*

In summary, the pore-scale multiphase simulation model developed in this thesis provides a strong basis for understanding two-phase ($scCO_2$-brine) fluid distribution, the role of inlet fluid flow rate and estimation of various parameters, such fluid relative permeability $scCO_2$ capillary pressure, capillary trapping capacity, etc., of geological porous media. Also, direct simulation of micro-pores provided results for various Darcy-scale properties (residual saturation and relative permeability) with a low computational cost compared to existing approaches.

This simulation model was used to develop a new model for the assessment of $scCO_2$ capillary pressure via pore-scale CFD-based numerical simulation. In this work, $scCO_2$ capillary pressure was predicted by using fluid relative permeability, which was estimated using modelled fluid saturation values for Berea sandstone. As there is very little data available in the literature (both experimental and numerical) regarding $scCO_2$-brine systems in Ottawa F42 Sand Pack, this work has opened a new window in this regard ($scCO_2$ capillary pressure determination). Furthermore, this study highlighted the importance of pore-scale multiphase simulation models, which can provide a strong basis for explaining various parameters at low expense and time cost compared to laboratory-based experiments. The outcome of this study also provides an insightful framework for the assessment of $scCO_2$ in CCS systems via numerical simulation.

7.3. *Recommendation for future work*

In this study, $scCO_2$ capillary pressure was obtained from fluid relative permeability values estimated by numerical simulation. The predictions of fluid relative permeability matched with previous experimental and numerical works, but there are still many unanswered questions concerning the most reliable measurement techniques, appropriate measurements of analogue conditions, and the best fluids for $scCO_2$-brine systems. Fluid relative permeability is a major factor determining the fate and transport of trapped CO_2 in a CCS project. However, due to the very low viscosity of CO_2 compared to brine, $scCO_2$-brine is much more capillary-dominated. This unique property of CO_2 results in two challenges: 1) reliable fluid relative permeability measurements must be ensured and 2) the influence of fluid properties on $scCO_2$-brine flow behaviour must be determined. The following suggestions may improve the effectiveness of the proposed model in a broader respect and provide new directions for solving those challenges through further research.

1. In future, this model can be extended to predict brine capillary pressures for $scCO_2$-brine systems. Also, the numerical model can be utilized to predict relative permeability and capillary pressure curves with the help of other empirical equations.

2. Brine saturations at different salinities can be applied through this model. Then, this model can be extended to a range of conditions with various pressures and

temperatures to allow the systematic study of relative permeability curves during imbibition.

3. The proposed numerical model was established for a $scCO_2$-brine system and can now be expanded to a three-phase system. Then, the influence of interfacial tension and viscosity on fluid relative permeability can be investigated for different fluids/phases.

4. Moreover, this study can be extended to work with intermediate-wet and oil-wet media, and other formations (such as carbonates, etc.).

5. Finally, this model may be utilized to study and compare various methods of enhanced oil recovery (EOR).

References

Abaci, S., Edwards, J. S., & Whittaker, B. N. (1992). Relative permeability measurements for two phase flow in unconsolidated sands. *Mine Water and the Environment*, *11*(2), 11-26.

Aghaei, A., & Piri, M. (2015). Direct pore-to-core up-scaling of displacement processes: Dynamic pore network modelling and experimentation. *Journal of Hydrology*, *522*, 488-509.

Ahmed, S., Iglauer, S. (2012). Brine permeability predictions for sand packs and sandstones using Navier-Stokes equations and three-dimensional micro-tomography images of pore spaces. *9th International Conference on CFD in the Minerals and Process Industries,* Melbourne, Australia.

Akbarabadi, M., & Piri, M. (2013). Relative permeability hysteresis and capillary trapping characteristics of supercritical CO_2/brine systems: An experimental study at reservoir conditions. *Advances in Water Resources*, *52*, 190-206.

Al Mansoori, S. K., Itsekiri, E., Iglauer, S., Pentland, C. H., Bijeljic, B., & Blunt, M. J. (2010). Measurements of non-wetting phase trapping applied to carbon dioxide storage. *International Journal of Greenhouse Gas Control*, *4*(2), 283-288.

Al-Futaisi, A., & Patzek, T. W. (2003). Impact of wettability alteration on two-phase flow characteristics of sandstones: A quasi-static description. *Water Resources Research*, *39*(2).

Al-Menhali, A., Niu, B., & Krevor, S. (2015). Capillarity and wetting of carbon dioxide and brine during drainage in Berea sandstone at reservoir conditions. *Water Resources Research*, *51*(10), 7895-7914.

Anderson, W. G. (1986). Wettability literature survey-part 3: The effects of wettability on the electrical properties of porous media. Journal of Petroleum Technology, 38(12), 1-371.

Anderson, W. G. (1987). Wettability literature survey-part 6: The effects of wettability on waterflooding. *Journal of Petroleum Technology*, *39*(12), 1-605.

Andrew, M., Bijeljic, B., & Blunt, M. J. (2014). Pore-by-pore capillary pressure measurements using X-ray microtomography at reservoir conditions: Curvature, snap-off, and remobilization of residual CO2. Water Resources Research, 50(11), 8760-8774.

Ansys, C. F. X. (2006). Release 11.0. ANSYS CFX-Solver Theory Guide, ANSYS.

Ansys, C. F. X. (2009). ANSYS CFX-solver modelling guide. South pointe, Canonsburg, USA.

ANSYS, C. INC., 2012. ANSYS ICEM CFD.

Armstrong, R. T., Georgiadis, A., Ott, H., Klemin, D., & Berg, S. (2014). Critical capillary number: Desaturation studied with fast X-ray computed microtomography. *Geophysical Research Letters*, *41*(1), 55-60.

Arrufat, T., Bondino, I., Zaleski, S., Lagree, B., & Keskes, N. (2014, November). Developments on relative permeability computation in 3D rock images. In Abu Dhabi International Petroleum Exhibition and Conference. Society of Petroleum Engineers.

Avizo Software User's Guide. (2018). Retrieved from https://www.fei.com/software/avizo-user-guide/

Babchin, A. J., & Faybishenko, B. (2014). On the capillary pressure function in porous media based on relative permeabilities of two immiscible fluids. *Colloids and Surfaces A: Physicochemical and Engineering Aspects*, *462*, 225-230.

Bachu, S. (2013). Drainage and imbibition CO2/brine relative permeability curves at in situ conditions for sandstone formations in western Canada. Energy Procedia, 37, 4428-4436.

Bachu, S., & Bennion, B. (2008). Effects of in-situ conditions on relative permeability characteristics of CO_2-brine systems. *Environmental Geology*, *54*(8), 1707-1722.

Balashov, V. N., Guthrie, G. D., Hakala, J. A., Lopano, C. L., Rimstidt, J. D., & Brantley, S. L. (2013). Predictive modeling of CO_2 sequestration in deep saline sandstone reservoirs: Impacts of geochemical kinetics. *Applied Geochemistry*, *30*, 41-56.

Bartley, J. T., & Ruth, D. W. (2001). Experimental investigation of unsteady-state relative permeability in sand-packs. In *Society of Core Analysis Conference* (Vol. 22, pp. 1-14).

Bear, J. (2013). Dynamics of fluids in porous media. Courier Corporation.

Bennion, B., & Bachu, S. (2008). Drainage and imbibition relative permeability relationships for supercritical CO_2/brine and H_2S/brine systems in intergranular sandstone, carbonate, shale, and anhydrite rocks. *SPE Reservoir Evaluation & Engineering*, *11*(03), 487-496.

Benson, S., Pini, R., Reynolds, C., & Krevor, S. (n.d.). Global CCS Institute targeted report No. 2 relative permeability analyses to describe multi-phase flow in CO_2 storage reservoirs.

Blunt, M. J. (1997). Effects of heterogeneity and wetting on relative permeability using pore level modeling. SPE Journal, 2(01), 70-87.

Blunt, M. J. (1998). Physically-based network modeling of multiphase flow in intermediate-wet porous media. *Journal of Petroleum Science and Engineering*, *20*(3-4), 117-125.

Blunt, M. J. (2001). Flow in porous media: Pore-network models and multiphase flow. Current Opinion in Colloid & Interface Science, 6(3), 197-207.

Blunt, M. (2017). Multiphase Flow in Permeable Media: A Pore-Scale Perspective. Cambridge: Cambridge University Press. doi:10.1017/9781316145098.

Blunt, M. J., Bijeljic, B., Dong, H., Gharbi, O., Iglauer, S., Mostaghimi, P. & Pentland, C. (2013). Pore-scale imaging and modelling. Advances in Water Resources, 51, 197-216.

Blunt, M. J., Jackson, M. D., Piri, M., & Valvatne, P. H. (2002). Detailed physics, predictive capabilities and macroscopic consequences for pore-network models of multiphase flow. *Advances in Water Resources*, *25*(8-12), 1069-1089.

Blunt, M., King, M. J., & Scher, H. (1992). Simulation and theory of two-phase flow in porous media. Physical Review A, 46(12), 7680.

Brackbill, J. U., Kothe, D. B., & Zemach, C. (1992). A continuum method for modelling surface tension. *Journal of Computational Physics*, *100*(2), 335-354.

Bravo, M. C., Araujo, M., & Lago, M. E. (2007). Pore network modeling of two-phase flow in a liquid-(disconnected) gas system. *Physica A: Statistical Mechanics and its Applications*, *375*(1), 1-17.

Burnside, N. M., & Naylor, M. (2014). Review and implications of relative permeability of CO2/brine systems and residual trapping of CO2. International Journal of Greenhouse Gas Control, 23, 1-11.

Busch, A., & Müller, N. (2011). Determining CO_2/brine relative permeability and capillary threshold pressures for reservoir rocks and caprocks: Recommendations for development of standard laboratory protocols. *Energy Procedia*, *4*, 6053-6060.

Calabrese, M., Masserano, F., & Blunt, M. J. (2005, January). Simulation of physical-chemical processes during carbon dioxide sequestration in geological structures. In SPE Annual Technical Conference and Exhibition. Society of Petroleum Engineers.

Carroll, S. A., Keating, E., Mansoor, K., Dai, Z., Sun, Y., Trainor-Guitton, W. & Bacon, D. (2014). Key factors for determining groundwater impacts due to leakage from geologic carbon sequestration reservoirs. International Journal of Greenhouse Gas Control, 29, 153-168.

Chadwick, R. A. (2014). Offshore CO2 storage: Sleipner natural gas field beneath the North Sea. In Geological Storage of Carbon Dioxide (CO2) (pp. 227-253e).

Chalbaud, C., Robin, M., Lombard, J. M., Martin, F., Egermann, P., & Bertin, H. (2009). Interfacial tension measurements and wettability evaluation for geological CO2 storage. *Advances in Water Resources*, *32*(1), 98-109.

Chatzis, I., & Dullien, F. A. (1977). Modelling pore structure by 2-d and 3-d networks with application to sandstones. Journal of Canadian Petroleum Technology, 16(01).

Chatzis, I., & Morrow, N. R. (1984). Correlation of capillary number relationships for sandstone. Society of Petroleum Engineers Journal, 24(05), 555-562.

Cieplak, P., Kollman, P., & Lybrand, T. (1990). A new water potential including polarization: Application to gas-phase, liquid, and crystal properties of water. *The Journal of Chemical Physics*, *92*(11), 6755-6760.

Corey, A. T. (1954). The interrelation between gas and oil relative permeabilities. *Producers Monthly*, *19*(1), 38-41.

Dai, Z., Middleton, R., Viswanathan, H., Fessenden-Rahn, J., Bauman, J., Pawar, R., & McPherson, B. (2013). An integrated framework for optimizing CO2 sequestration and enhanced oil recovery. Environmental Science & Technology Letters, 1(1), 49-54.

Das, D. B., & Mirzaei, M. (2013). Experimental measurement of dynamic effect in capillary pressure relationship for two-phase flow in weakly layered porous media. *AIChE Journal*, *59*(5), 1723-1734.

Das, D. B., Gill, B. S., Abidoye, L. K., & Khudaida, K. J. (2014). A numerical study of dynamic capillary pressure effect for supercritical carbon dioxide-water flow in porous domain. *AIChE Journal*, *60*(12), 4266-4278.

Dong, H., & Blunt, M. J. (2009). Pore-network extraction from micro-computerized-tomography images. *Physical Review E*, *80*(3), 036307.

Doughty, C., & Pruess, K. (2004). Modeling supercritical carbon dioxide injection in heterogeneous porous media. Vadose Zone Journal, 3(3), 837-847.

Duan, Z., Sun, R., Zhu, C., & Chou, I. M. (2006). An improved model for the calculation of CO2 solubility in aqueous solutions containing Na^+, K^+, Ca^{2+}, Mg^{2+}, Cl^-, and SO_4^{2-}. *Marine Chemistry*, *98*(2-4), 131-139.

Ennis-King, J. P., & Paterson, L. (2005). Role of convective mixing in the long-term storage of carbon dioxide in deep saline formations. SPE Journal, 10(03), 349-356.

Fatt, I. (1956). The network model of porous media.

Gittins, P., Iglauer, S., Pentland, C. H., Al-Mansoori, S., Al-Sayari, S., Bijeljic, B., & Blunt, M. J. (2010). Nonwetting phase residual saturation in sand packs. *Journal of Porous Media*, *13*(7).

Global CCS Institute. (2018). Retrieved from https://www.globalccsinstitute.com/projects/co2crc-otway-project.

Global, C. C. S. (2011). Institute. The global status of CCS.

Gough, C., Mander, S., & Haszeldine, S. (2010). A roadmap for carbon capture and storage in the UK. International Journal of Greenhouse Gas Control, 4(1), 1-12.

Herring, A. L., Andersson, L., Newell, D. L., Carey, J. W., & Wildenschild, D. (2014). Pore-scale observations of supercritical CO_2 drainage in Bentheimer sandstone by

synchrotron x-ray imaging. *International Journal of Greenhouse Gas Control*, *25*, 93-101.

Herring, A. L., Harper, E. J., Anderson, L., Sheppard, A., Bay, B. K., & Wildenschild, D. (2013). Effect of fluid topology on residual non-wetting phase trapping: Implications for geologic CO_2 sequestration. *Advances in Water Resources*, *62*, 47-58.

Hesse, M. A., & Woods, A. W. (2010). Buoyant dispersal of CO2 during geological storage. Geophysical Research Letters, 37(1).

Holloway, S. (2001). Storage of fossil fuel-derived carbon dioxide beneath the surface of the earth. Annual Review of Energy and the Environment, 26(1), 145-166.

Holmes, D. W., Williams, J. R., Tilke, P., & Leonardi, C. R. (2016). Characterizing flow in oil reservoir rock using SPH: Absolute permeability. Computational Particle Mechanics, 3(2), 141-154.

Iglauer, S., & Muggeridge, A. (2013). The impact of tides on the capillary transition zone. *Transport in Porous Media*, *97*(1), 87-103.

Iglauer, S., & Muggeridge, A. H. (2012). Time dependence of free fall gravity drainage in unconsolidated sand. *Journal of Porous Media*, *15*(8).

Iglauer, S., Wülling, W., Pentland, C. H., Al-Mansoori, S. K., & Blunt, M. J. (2011). Capillary-trapping capacity of sandstones and sand packs. *SPE Journal*, *16*(04), 778-783.

IPCC Special Report on Global Warming of 1.5°C on 8th October, 2018 in Incheon, Republic of Korea (https://www.ipcc.ch/pdf/session48/pr_181008_P48_spm_en.pdf).

Jackson, M. D., Valvatne, P. H., & Blunt, M. J. (2003). Prediction of wettability variation and its impact on flow using pore-to reservoir-scale simulations. *Journal of Petroleum Science and Engineering*, *39*(3-4), 231-246.

Jackson, M. D., Valvatne, P. H., & Blunt, M. J. (2005). Prediction of wettability variation within an oil/water transition zone and its impact on production. SPE Journal, 10(02), 185-195.

Jahan, F., Hossain, M. M., Ahmed, S., & Iglauer, S. (2017, April). Investigating Impact of Various Properties on Relative Permeability and Non-Wetting Phase Fractional

Flow in Brine/Oil System in Water-Wet Reservoir Rock by Numerical Simulation. SPE Western Regional Meeting, 23-27 April, Bakersfield, California (SPE-185744-MS)

Jahan, F., Hossain, M., Ahmed, S., Iglauer, S. (2016). Numerical modelling for the prediction of residual CO_2 trapping in water-wet geological porous media. *SPE Asia Pacific Oil & Gas Conference and Exhibition*, Perth, Australia.

Jakobsen, J. P., Tangen, G., Nordbø, Ø. & Mølnvik, M. J. (2008). Methodology for CO2 chain analysis. International Journal of Greenhouse Gas Control, 2(4), 439-447.

Juanes, R., Spiteri, E. J., Orr, F. M., & Blunt, M. J. (2006). Impact of relative permeability hysteresis on geological CO2 storage. Water Resources Research, 42(12).

Jung, J., & Hu, J. W. (2016). Impact of pressure and brine salinity on capillary pressure-water saturation relations in geological CO2 sequestration. *Advances in Condensed Matter Physics Volume 2016, Article ID 5603739, 11 pages, http://dx.doi.org/10.1155/2016/5603739*

Kalam, M. Z. (2012). Digital rock physics for fast and accurate special core analysis in carbonates. In *New Technologies in the Oil and Gas Industry*. InTech Open, DOI: 10.5772/52949

Kawanishi, T., Hayashi, Y., Roberts, P. V., & Blunt, M. J. (1998). Fluid-fluid interfacial area during two and three phase fluid displacement in porous media: A network model study. *IAHS Publication (International Association of Hydrological Sciences)*, (250), 89-95.

Kheshgi, H., de Coninck, H., & Kessels, J. (2012). Carbon dioxide capture and storage: Seven years after the IPCC special report. *Mitigation and Adaptation Strategies for Global Change*, *17*(6), 563-567.

Khudaida, K. J., & Das, D. B. (2014). A numerical study of capillary pressure–saturation relationship for supercritical carbon dioxide (CO_2) injection in deep saline aquifer. *Chemical Engineering Research and Design*, *92*(12), 3017-3030.

Kim, Y., Wan, J., Kneafsey, T. J., & Tokunaga, T. K. (2012). Dewetting of silica surfaces upon reactions with supercritical CO_2 and brine: Pore-scale studies in micromodels. *Environmental Science & Technology*, *46*(7), 4228-4235.

Krause, M. H., Perrin, J. C., & Benson, S. M. (2011). Modelling permeability distributions in a sandstone core for history matching core-flood experiments. *SPE Journal*, *16*(04), 768-777.

Krause, M., Krevor, S., & Benson, S. M. (2013). A procedure for the accurate determination of sub-core scale permeability distributions with error quantification. Transport in Porous Media, 98(3), 565-588.

Krevor, S. C., Pini, R., Zuo, L., & Benson, S. M. (2012). Relative permeability and trapping of CO_2 and water in sandstone rocks at reservoir conditions. *Water Resources Research*, *48*(2).

Krevor, S., Blunt, M. J., Benson, S. M., Pentland, C. H., Reynolds, C., Al-Menhali, A., & Niu, B. (2015). Capillary trapping for geologic carbon dioxide storage–From pore scale physics to field scale implications. *International Journal of Greenhouse Gas Control*, *40*, 221-237.

Lake, L. W., & Venuto, P. B. (1990). A niche for enhanced oil recovery in the 1990s. Oil & Gas Journal, 88(17), 62-67.

Land, C. S. (1968). Calculation of imbibition relative permeability for two-and three-phase flow from rock properties. *Society of Petroleum Engineers Journal*, *8*(02), 149-156.

Lenormand, R., & Zarcone, C. (1984, January). Role of roughness and edges during imbibition in square capillaries. In *SPE Annual Technical Conference and Exhibition*. Society of Petroleum Engineers.

Lenormand, R., Touboul, E., & Zarcone, C. (1988). Numerical models and experiments on immiscible displacements in porous media. Journal of Fluid Mechanics, 189, 165-187.

Leverett, M. (1941). Capillary behaviour in porous solids. Transactions of the AIME, 142(01), 152-169.

Levine, J. S., Goldberg, D. S., Lackner, K. S., Matter, J. M., Supp, M. G., & Ramakrishnan, T. S. (2013). Relative permeability experiments of carbon dioxide displacing brine and their implications for carbon sequestration. *Environmental Science & Technology*, *48*(1), 811-818.

Levine, J. S., Matter, J. M., Goldberg, D. S., Lackner, K. S., Supp, M. G., & Ramakrishnan, T. S. (2011). Two phase brine-CO_2 flow experiments in synthetic and natural media. *Energy Procedia*, *4*, 4347-4353.

Li, K., & Horne, R. N. (2006). Comparison of methods to calculate relative permeability from capillary pressure in consolidated water-wet porous media. *Water Resources Research*, *42*(6).

Li, L., Peters, C. A., & Celia, M. A. (2006). Upscaling geochemical reaction rates using pore-scale network modelling. *Advances in Water Resources*, *29*(9), 1351-1370.

Li, X., Akbarabadi, M., Karpyn, Z. T., Piri, M., & Bazilevskaya, E. (2015). Experimental investigation of carbon dioxide trapping due to capillary retention in saline aquifers. *Geofluids*, *15*(4), 563-576.

Li, Xinqian, (2013). Experimental investigation of Carbon dioxide trapping due to capillary retention in deep saline aquifer (Doctoral dissertation). Retrieved from https://etda.libraries.psu.edu/files/final_submissions/8728.

MacMinn, C. W., Neufeld, J. A., Hesse, M. A., & Huppert, H. E. (2012). Spreading and convective dissolution of carbon dioxide in vertically confined, horizontal aquifers. *Water Resources Research*, *48*(11).

Meakin, P., & Tartakovsky, A. M. (2009). Modelling and simulation of pore-scale multiphase fluid flow and reactive transport in fractured and porous media. Reviews of Geophysics, 47(3).

Michael, K., Golab, A., Shulakova, V., Ennis-King, J., Allinson, G., Sharma, S., & Aiken, T. (2010). Geological storage of CO2 in saline aquifers—a review of the experience from existing storage operations. International Journal of Greenhouse Gas Control, 4(4), 659-667.

Mirzaei, M., & Das, D. B. (2013). Experimental investigation of hysteretic dynamic effect in capillary pressure–saturation relationship for two-phase flow in porous media. *AIChE Journal*, *59*(10), 3958-3974.

Müller, N. (2011). Supercritical CO2-brine relative permeability experiments in reservoir rocks—literature review and recommendations. Transport in Porous Media, 87(2), 367-383.

Naar, J., Wygal, R. J., & Henderson, J. H. (1962). Imbibition relative permeability in unconsolidated porous media. *Society of Petroleum Engineers Journal*, *2*(01), 13-17.

Narsilio, G. A., Buzzi, O., Fityus, S., Yun, T. S., & Smith, D. W. (2009). Upscaling of Navier–Stokes equations in porous media: Theoretical, numerical and experimental approach. *Computers and Geotechnics*, *36*(7), 1200-1206.

Niu, B., Al-Menhali, A., & Krevor, S. C. (2015). The impact of reservoir conditions on the residual trapping of carbon dioxide in Berea sandstone. Water Resources Research, 51(4), 2009-2029.

Nordbotten, J. M., Celia, M. A., & Bachu, S. (2005). Injection and storage of CO_2 in deep saline aquifers: Analytical solution for CO_2 plume evolution during injection. *Transport in Porous media*, *58*(3), 339-360.

Obi, E. O. I., & Blunt, M. J. (2006). Streamline-based simulation of carbon dioxide storage in a North Sea aquifer. Water Resources Research, 42(3).

Øren, P. E., & Bakke, S. (2003). Reconstruction of Berea sandstone and pore-scale modelling of wettability effects. *Journal of Petroleum Science and Engineering*, *39*(3-4), 177-199.

Orr Jr, F. M., & Silva, M. K. (1987). Effect of oil composition on minimum miscibility pressure-part 2: Correlation. SPE Reservoir Engineering, 2(04), 479-491.

Parliament of Australia. (2018). Retrieved from https://www.aph.gov.au/About_Parliament/Parliamentary_Departments/Parliamentary_Library/Browse_by_Topic/ClimateChangeold/responses/mitigation/emissions/renewable.

Patankar, S. (1980). *Numerical heat transfer and fluid flow*. CRC press, U.S.A.

Peksa, A. E., Wolf, K. H. A., & Zitha, P. L. (2015). Bentheimer sandstone revisited for experimental purposes. *Marine and Petroleum Geology*, *67*, 701-719.

Pentland, C. H., El-Maghraby, R., Georgiadis, A., Iglauer, S., & Blunt, M. J. (2011). Immiscible displacements and capillary trapping in CO2 storage. *Energy Procedia*, *4*, 4969-4976.

Pentland, C. H., El-Maghraby, R., Iglauer, S., & Blunt, M. J. (2011). Measurements of the capillary trapping of super-critical carbon dioxide in Berea sandstone. *Geophysical Research Letters*, *38*(6).

Pentland, C. H., Itsekiri, E., Al-Mansoori, S., Iglauer, S., Bijeljic, B., & Blunt, M. J. (2010). Measurement of nonwetting-phase trapping in sandpacks. *SPE Journal*, *15*(02), 274-281.

Perrin, J. C., Falta, R. W., Krevor, S., Zuo, L., Ellison, K., & Benson, S. M. (2011). Laboratory experiments on core-scale behavior of CO2 exolved from CO2-saturated brine. Energy Procedia, 4, 3210-3215.

Perrin, J. C., Krause, M., Kuo, C. W., Miljkovic, L., Charoba, E., & Benson, S. M. (2009). Core-scale experimental study of relative permeability properties of CO_2 and brine in reservoir rocks. *Energy Procedia*, *1*(1), 3515-3522.

Piller, M., Casagrande, D., Schena, G., & Santini, M. (2014). Pore-scale simulation of laminar flow through porous media. In *Journal of Physics: Conference Series* (Vol. 501, No. 1, p. 012010). IOP Publishing. DOI: 10.1088/1742-6596/501/1/012010

Pini, R., & Benson, S. M. (2013). Simultaneous determination of capillary pressure and relative permeability curves from core-flooding experiments with various fluid pairs. *Water Resources Research*, *49*(6), 3516-3530.

Pini, R., Krevor, S. C., & Benson, S. M. (2012). Capillary pressure and heterogeneity for the CO2/water system in sandstone rocks at reservoir conditions. Advances in Water Resources, 38, 48-59.

Plug, W. J., & Bruining, J. (2007). Capillary pressure for the sand–CO_2–water system under various pressure conditions: Application to CO_2 sequestration. *Advances in Water Resources*, *30*(11), 2339-2353.

Pruess, K., Xu, T., Apps, J., & Garcia, J. (2001, January). Numerical modelling of aquifer disposal of CO2. In SPE/EPA/DOE Exploration and Production Environmental Conference. Society of Petroleum Engineers.

Qi, R., LaForce, T. C., & Blunt, M. J. (2009). Design of carbon dioxide storage in aquifers. International Journal of Greenhouse Gas Control, 3(2), 195-205.

Raeini, A. Q., Bijeljic, B., & Blunt, M. J. (2014). Numerical modelling of sub-pore scale events in two-phase flow through porous media. *Transport in Porous Media*, *101*(2), 191-213.

Raeini, A. Q., Bijeljic, B., & Blunt, M. J. (2015). Modelling capillary trapping using finite-volume simulation of two-phase flow directly on micro-CT images. Advances in Water Resources, 83, 102-110.

Raeini, A. Q., Blunt, M. J., & Bijeljic, B. (2012). Modelling two-phase flow in porous media at the pore scale using the volume-of-fluid method. Journal of Computational Physics, 231(17), 5653-5668.

Raeini, A. Q., Blunt, M. J., & Bijeljic, B. (2014). Direct simulations of two-phase flow on micro-CT images of porous media and upscaling of pore-scale forces. Advances in Water Resources, 74, 116-126.

Ramstad, T., Idowu, N., Nardi, C., & Øren, P. E. (2012). Relative permeability calculations from two-phase flow simulations directly on digital images of porous rocks. *Transport in Porous Media*, *94*(2), 487-504.

Ramstad, T., Øren, P. E., & Bakke, S. (2010). Simulation of two-phase flow in reservoir rocks using a lattice Boltzmann method. *SPE Journal*, *15*(04), 917-927.

Riaz, A., Hesse, M., Tchelepi, H. A., & Orr, F. M. (2006). Onset of convection in a gravitationally unstable diffusive boundary layer in porous media. Journal of Fluid Mechanics, 548, 87-111.

Richardson, J. G., Kerver, J. K., Hafford, J. A., & Osoba, J. S. (1952). Laboratory determination of relative permeability. *Journal of Petroleum Technology*, *4*(08), 187-196.

Riddiford, F. A., Tourqui, A., Bishop, C. D., Taylor, B., & Smith, M. (2003). -A Cleaner Development: The in Salah Gas Project, Algeria. In Greenhouse Gas Control Technologies-6th International Conference (pp. 595-600).

Riepe, L., Suhaimi, M. H., Kumar, M., & Knackstedt, M. A. (2011, January). Application of high resolution micro-CT-imaging and pore network modeling (PNM) for the petrophysical characterization of tight gas reservoirs: A case history from a

deep clastic tight gas reservoir in Oman. In SPE Middle East Unconventional Gas Conference and Exhibition. Society of Petroleum Engineers.

Roof, J. G. (1970). Snap-off of oil droplets in water-wet pores. *Society of Petroleum Engineers Journal*, *10*(01), 85-90.

Rubin, E., & De Coninck, H. (2005). IPCC special report on carbon dioxide capture and storage. UK: Cambridge University Press. TNO (2004): Cost Curves for CO2 Storage, Part, 2.

Ruspini, L. C., Farokhpoor, R., & Øren, P. E. (2017). Pore-scale modeling of capillary trapping in water-wet porous media: A new cooperative pore-body filling model. *Advances in Water Resources*, *108*, 1-14.

Saeedi, A., Rezaee, R., Evans, B., & Clennell, B. (2011). Multiphase flow behaviour during CO2 geo-sequestration: Emphasis on the effect of cyclic CO2-brine flooding. Journal of Petroleum Science and Engineering, 79(3-4), 65-85.

Saenger, E. H., Lebedev, M., Uribe, D., Osorno, M., Vialle, S., Duda, M., & Steeb, H. (2016). Analysis of high-resolution X-ray computed tomography images of Bentheim sandstone under elevated confining pressures. *Geophysical Prospecting*, *64*(4), 848-859.

Saripalli, K. P., McGrail, B. P., White, M. D., & Saripalli, P. (2000). Modeling the sequestration of CO2 in deep geological formations. Laboratory Directed Research and Development Annual Report-Fiscal Year, 233.

Schlüter, S., Berg, S., Rücker, M., Armstrong, R. T., Vogel, H. J., Hilfer, R., & Wildenschild, D. (2016). Pore-scale displacement mechanisms as a source of hysteresis for two-phase flow in porous media. *Water Resources Research*, *52*(3), 2194-2205.

Shi, J. Q., Xue, Z., & Durucan, S. (2011). Supercritical CO_2 core flooding and imbibition in Tako sandstone—Influence of sub-core scale heterogeneity. *International Journal of Greenhouse Gas Control*, *5*(1), 75-87.

Shi, J.-Q., Xue, Z., & Durucan, S. (2011). Supercritical CO_2 core flooding and imbibition in Berea sandstone—CT imaging and numerical simulation. Energy Procedia, 4, 5001-5008. doi:https://doi.org/10.1016/j.egypro.2011.02.471

Silin, D. B., Jin, G., & Patzek, T. W. (2003, January). Robust determination of the pore space morphology in sedimentary rocks. In *SPE Annual Technical Conference and Exhibition*. Society of Petroleum Engineers.

Soroush, M., Wessel-Berg, D., & Kleppe, J. (2013, April). Effects of wetting behaviour on residual trapping in CO_2-brine systems. In *SPE Western Regional & AAPG Pacific Section Meeting 2013 Joint Technical Conference*. Society of Petroleum Engineers.

Soroush, M., Wessel-Berg, D., Torsaeter, O., & Kleppe, J. (2013). Investigating impact of flow rate and wettability on residual trapping in CO2 storage in saline aquifers through relative permeability experiments. Energy and Environment Research, 3(2), 53.

Spiteri, E. J., Juanes, R., Blunt, M. J., & Orr, F. M. (2008). A new model of trapping and relative permeability hysteresis for all wettability characteristics. SPE Journal, 13(03), 277-288.

Spiteri, E., Juanes, R., Blunt, M. J., & Orr, F. M. (2005, January). Relative-permeability hysteresis: Trapping models and application to geological CO2 sequestration. In SPE Annual Technical Conference and Exhibition. Society of Petroleum Engineers.

Standing, M. B. (1975). Notes on relative permeability relationships. *Lecture Notes, Trondheim, Norway*.

Succi, S., Foti, E., & Higuera, F. (1989). Three-dimensional flows in complex geometries with the lattice Boltzmann method. EPL (Europhysics Letters), 10(5), 433.

Suekane, T., & Nguyen, H. T. (2013). Relation between the initial and residual gas saturations of gases trapped by capillarity in natural sandstones. *Journal of Fluid Science and Technology*, *8*(3), 322-336.

Suekane, T., & Ushita, H. (2011). Effect of buoyancy on pore-scale characteristics of two-phase flow in porous media. In Computed Tomography-Special Applications. InTech Open, DOI: 10.5772/23279.

Suekane, T., Nobuso, T., Hirai, S., & Kiyota, M. (2008). Geological storage of carbon dioxide by residual gas and solubility trapping. *International Journal of Greenhouse Gas Control*, *2*(1), 58-64.

Suekane, T., Zhou, N., Hosokawa, T., & Matsumoto, T. (2010). Direct observation of trapped gas bubbles by capillarity in sandy porous media. Transport in Porous Media, 82(1), 111-122.

Taber, J. J., Martin, F. D., & Seright, R. S. (1997). EOR screening criteria revisited-Part 1: Introduction to screening criteria and enhanced recovery field projects. SPE Reservoir Engineering, 12(03), 189-198.

Talabi, O. A. (2008). Pore-scale simulation of NMR response in porous media.

Talabi, O. A. (2008). Pore-scale simulation of NMR response in porous media.

Talabi, O. A., Alsayari, S., Blunt, M. J., Dong, H., & Zhao, X. (2008, January). Predictive pore scale modelling: From 3D images to multiphase flow simulations. In *SPE Annual Technical Conference and Exhibition*. Society of Petroleum Engineers.

The Paris Agreement on Climate Change. (2017). Retrieved from https://www.nrdc.org/sites/default/files/paris-agreement-climate-change-2017-ib.pdf.

Tokunaga, T. K., Wan, J., Jung, J. W., Kim, T. W., Kim, Y., & Dong, W. (2013). Capillary pressure and saturation relations for supercritical CO_2 and brine in sand: High-pressure Pc (Sw) controller/meter measurements and capillary scaling predictions. *Water Resources Research*, *49*(8), 4566-4579.

UK Government Web Archieve. (2018). Retrieved from https://www.nationalarchives.gov.uk/webarchive/

Valvatne, P. H., Piri, M., Lopez, X., & Blunt, M. J. (2005). Predictive pore-scale modelling of single and multiphase flow. In *Upscaling Multiphase Flow in Porous Media* (pp. 23-41). Springer, Dordrecht.

Versteeg, H. K., & Malalasekera, W. (1995). Computational fluid dynamics. *The finite volume method*, Pearson, Prentice Hall, Newyork.

Violeau, D., & Rogers, B. D. (2016). Smoothed particle hydrodynamics (SPH) for free-surface flows: Past, present and future. Journal of Hydraulic Research, 54(1), 1-26.

Voormeij, D. A., & Simandl, G. J. (2004). Geological, ocean, and mineral CO_2 sequestration options: A technical review. *Geoscience Canada*, *31*(1).

Weibull, W. (1951). Wide applicability. *Journal of Applied Mechanics*, *103*(730), 293-297.

Weibull, W. (2013). *Fatigue testing and analysis of results*. Pergamon Press Ltd, Oxford, London, UK

Wildenschild, D., Armstrong, R. T., Herring, A. L., Young, I. M., & Carey, J. W. (2011). Exploring capillary trapping efficiency as a function of interfacial tension, viscosity, and flow rate. Energy Procedia, 4, 4945-4952.

Wildenschild, D., Hopmans, J. W., & Simunek, J. (2001). Flow rate dependence of soil hydraulic characteristics. *Soil Science Society of America Journal*, *65*(1), 35-48.

Wulling, W., Pentland, C. H., Al Mansoori, S. K., & Blunt, M. J. (2009, January). Capillary trapping capacity of rocks and sandpacks. In *EUROPEC/EAGE Conference and Exhibition*. Society of Petroleum Engineers.

Xu, T., Apps, J. A., & Pruess, K. (2003). Reactive geochemical transport simulation to study mineral trapping for CO2 disposal in deep arenaceous formations. Journal of Geophysical Research: Solid Earth, 108(B2).

Yang, H., Xu, Z., Fan, M., Gupta, R., Slimane, R. B., Bland, A. E., & Wright, I. (2008). Progress in carbon dioxide separation and capture: A review. *Journal of Environmental Sciences*, *20*(1), 14-27.

Zaretskiy, Y., Geiger, S., Sorbie, K., & Förster, M. (2010). Efficient flow and transport simulations in reconstructed 3D pore geometries. *Advances in Water Resources*, *33*(12), 1508-1516.

Zhang, C., Oostrom, M., Wietsma, T. W., Grate, J. W., & Warner, M. G. (2011). Influence of viscous and capillary forces on immiscible fluid displacement: Pore-scale experimental study in a water-wet micromodel demonstrating viscous and capillary fingering. Energy & Fuels, 25(8), 3493-3505.

Zhang, W., Li, Y., Xu, T., Cheng, H., Zheng, Y., & Xiong, P. (2009). Long-term variations of CO_2 trapped in different mechanisms in deep saline formations: A case

study of the Songliao Basin, China. *International Journal of Greenhouse Gas Control*, *3*(2), 161-180.

Zhou, N., Hosokawa, T., Suekane, T., & Wang, Q. W. (2011). Experimental study of capillary trapping on the pore scale for various sandstone cores. Energy Procedia, 4, 5017-5023.

Appendix A

Calculation of fluid (scCO₂-brine) relative permeability values for drainage and imbibition processes (for set 1) for the Ottawa F42 Sand Pack.

As described in Chapter 4 (for an oil-brine system), similar fluid relative permeability equations are used to predict fluid relative permeability in a scCO2-brine system within the micropores of Ottawa F42 Sand Pack.

A. Prediction of Drainage Relative Permeability

Sample calculation of drainage fluid relative permeability (for set 1):

S_w = 0.785 (when simulation time = 1 s)

S_{wc} = 0.08 (from simulation)

$S_w{}^*$ = 0.766

$$K_{rw} = (S_w^*)^4 (4.1) \tag{1.1}$$

$$K_{nrw} = (1 - S_w^*)^2 [1 - (S_w^*)^2] \tag{1.2}$$

From the above equations,

K_{rw} = 0.35

K_{nrw} = 0.0225

B. Prediction of Imbibition Relative Permeability

B.1 scCO₂ relative permeability prediction

As for the oil-brine system (described in Chapter 4), the following equations are used to predict imbibition scCO₂ relative permeability.

$$K_{or} = K_r^o \, S_{0,F}^{*2} \left[1 - \left(1 - S_{o,F}^* \right)^{\frac{2+\lambda}{\lambda}} \right] \tag{2}$$

$$K_r^o = 1.31 - 2.62 \, S_{wc} + 1.1 (S_{wc})^2 \tag{3}$$

Where K_r^o = scCO$_2$ relative permeability at connate brine saturation

$$= 1.31 - 2.62\ S_{wc} + 1.1(S_{wc})^2 \quad [S_{wc} = 0.16, \text{ from simulation}]$$

$$= 0.92$$

So,F* = No

λ = pore-size distribution factor, which is the slope of a plot of log 1/Pc vs log Sw*.

B.2 Brine relative permeability prediction

Brine relative permeability can be found from Equation 4 (Land et al., 1968). This is the same equation as used to predict fluid relative permeability values for the oil-brine system in Chapter 4.

$$K_{rw} = S_w^{*2}\left[(S_w^* + S_{ot}^*)^2 - \frac{2}{C^2}\left(ln\frac{1-\{(1-S_{or,max}^*)(S_w^*+S_{ot}^*)\}}{1-\{S_{wi}^*(1-S_{or,max}^*)\}} + \frac{1}{1-\{(1-S_{or,max}^*)(S_w^*+S_{ot}^*)\}} - \frac{1}{1-\{S_{wi}^*(1-S_{or,max}^*)\}}\right)\right]$$

(4)

For this equation, normalized trapped scCO$_2$ saturation (S_{ot}*) is estimated first. Then, the other parameters were estimated and inserted in Equation (4) to determine K$_{rw}$. All estimation processes are discussed below.

Normalized trapped scCO$_2$ saturation (Sot*) determination

To determine normalized trapped scCO$_2$ saturation (S_{ot}*), the following equations (Standing, 1975) are used.

$$S_{o,F}^* = 0.5\left[(S_o^* - S_{or}^*) + \sqrt{\{(S_o^* - S_{or}^*)^2 + \frac{4}{C}(S_o^* - S_{or}^*)\}}\right] \tag{5}$$

$$S_{ot}^* = S_0^* - S_{o,F}^* \tag{6}$$

The correlation for Land's trapping coefficient, C, as given by Equation (7):

$$C = \frac{1}{S_{or}^*} - \frac{1}{S_{oi}^*} \qquad (7)$$

The values of normalized $scCO_2$ residual saturation, S_{or}^*, and the normalized $scCO_2$ saturation at various simulation times, S_o^*, in Equation (5) and the normalized free $scCO_2$ saturation at various simulation times, $S_{o,F}^*$, are determined from the numerical simulation results for drainage and imbibition processes after the system reaches a steady state, which is determined to occur when the pressure drop appears to be constant. The corresponding initial and residual fluid saturations (S_{wi}, S_{oi} and S_{or}) are then directly obtained from the simulation.

The various saturations described above, obtained from the numerical simulation of Ottawa F42 Sand Pack (for a $scCO_2$-brine system), are provided below in Table A.

Table A: Various saturation values obtained from simulation

Saturation	Value obtained from simulation
Connate brine saturation, S_{wc}	0.08
Maximum residual $scCO_2$ saturation, $S_{or,max}$	0.017
Initial brine saturation, S_{wi}	0.08
Initial $scCO_2$ saturation, S_{oi}	0.92
Residual $scCO_2$ saturation, S_{or}	0.008

The process of calculating normalized trapped $scCO_2$ saturation (Sot^*) is provided below through a sample calculation for an imbibition process with a simulation time of 1.0 s to demonstrate how the imbibition fluid relative permeability values were obtained.

Sample calculation for Land's trapping coefficient, C

Based on the data as obtained from the simulation (Table A),

$$S_{or}^* = \frac{S_{or}}{1\text{-}S_{wc}} = \frac{0.008}{1-0.08} = 0.0087$$

$$S_{oi}^* = \frac{S_{oi}}{1\text{-}S_{wc}} = \frac{0.92}{1\text{-}0.08} = 1.0$$

Therefore, from Equation (7), C = 114.

Sample calculation for normalized $scCO_2$ trapped saturation, S_{ot}

For an imbibition process with a simulation time of 10 s and inlet brine velocity = 0.03 m/s, the scCO$_2$ saturation, S$_o$ obtained from simulation = 0.306, which yields S$_o$* = $\frac{S_o}{1-S_o}$ = 0.3326

Inserting S$_o$* = 0.3326 and S$_{or}$* = 0.008 (as determined earlier) in Equation (5) yields S$_{o,F}$* = 0.247.

Therefore, from Equation (6): S$_o$t* = S$_o$* - S$_{o,F}$* = 0.0856

Other parameters of Equation (4) determination

Three parameters, S$_w$*, $S^*_{or,max}$ and S^*_{wi} are estimated in this section.

S$_w$* = Normalized brine saturation at various simulation times

$$= \frac{S_w - S_{wc}}{1 - S_{wc}}$$

Where, S$_w$ = Brine saturation at various simulation times;

$S^*_{or,max}$ = Normalized maximum residual supercritical CO$_2$ saturation

$= 0.017$; and

S^*_{wi} = Normalized initial brine saturation

$$= \frac{Swi}{1 - Swc} = 0.087.$$

So, Land's scCO$_2$ relative permeability, K$_{or}$ = 0.11 [from Equation (3)] and

Land's brine relative permeability, K$_{rw}$ = 0.20 [from Equation (4)].

Calculation of the non-wetting phase (scCO$_2$) capillary pressure for drainage and imbibition (for set 1) for the Ottawa F42 Sand Pack

Non-wetting phase (scCO$_2$) capillary pressure for both flow sequences (drainage and imbibition) can be estimated from Equation (8), which is the same equation used for the oil-brine system (Babchin et al., 2014).

$$P_c = \sigma cos\theta . S_v S_o^* + A \tag{8}$$

The calculation of imbibition $scCO_2$ capillary pressure Pc is provided below through a sample calculation with a simulation time of 10 s. Then, drainage $scCO_2$ capillary pressure is found by adding 1,221 Pa to the imbibition $scCO_2$ capillary pressure. This 1,221 Pa value is a constant, which represents the capillary pressure at the residual saturation point for a drainage process.

Sample calculation for drainage and imbibition $scCO_2$ capillary pressure, P_c:

Given:

Surface tension, $\sigma = 0.036$ N/m;

Contact angle, $\theta = 45°$;

Porosity, $\emptyset = 0.354$; and

Absolute permeability, $K = 42$ Darcy,

When $S_w^* = 0.667$ and

$S_o^* = 0.332$, then

$scCO_2$ relative permeability $= 0.11$;

Brine relative permeability, $K_w = 0.20$;

Imbibition $scCO_2$ capillary pressure $= 3,623$ Pa [from Equation 8]; and

Drainage $scCO_2$ capillary pressure $= 4,844$ Pa.

Appendix B

CFX Command Language for Run

LIBRARY:

 MATERIAL: Brine

  Material Group = User

  Option = Pure Substance

  Thermodynamic State = Liquid

   PROPERTIES:

   Option = General Material

   EQUATION OF STATE:

    Density = 1071 [kg m^-3]

    Molar Mass = 1 [kg mol^-1]

    Option = Value

   END

   SPECIFIC HEAT CAPACITY:

    Option = Value

    Specific Heat Capacity = 4200 [J kg^-1 K^-1]

    Specific Heat Type = Constant Pressure

   END

DYNAMIC VISCOSITY:

   Dynamic Viscosity = 0.001193 [Pa s]

   Option = Value

   END

MATERIAL: scCO$_2$

  Material Group = User

  Option = Pure Substance

  Thermodynamic State = Liquid

  PROPERTIES:

   Option = General Material

   EQUATION OF STATE:

    Density = 469 [kg m^-3]

    Molar Mass = 1.0 [kg kmol^-1]

    Option = Value

   END

   SPECIFIC HEAT CAPACITY:

    Option = Value

    Specific Heat Capacity = 3800 [J kg^-1 K^-1]

    Specific Heat Type = Constant Pressure

   END

DYNAMIC VISCOSITY:

Dynamic Viscosity = 2.1e-05 [Pa s]

Option = Value

END

FLOW: Flow Analysis 1

SOLUTION UNITS:

Angle Units = [rad]

Length Units = [m]

Mass Units = [kg]

Solid Angle Units = [sr]

Temperature Units = [K]

Time Units = [s]

END

ANALYSIS TYPE:

Option = Transient

EXTERNAL SOLVER COUPLING:

Option = None

END

INITIAL TIME:

Option = Automatic with Value

Time = 0 [s]

END

TIME DURATION:

Option = Total Time

Total Time = 25 [s]

END

TIME STEPS:

Option = Timesteps

Timesteps = 0.01 [s]

END

DOMAIN

DOMAIN: Default Domain Modified

Coord Frame = Coord 0

Domain Type = Fluid

Location = Assembly 2

BOUNDARY: Default Domain Modified Default

Boundary Type = WALL

Location = Primitive 2D BE,Primitive 2D BF,Primitive 2D BG,Primitive \

2D BH,Primitive 2D BI,Primitive 2D BJ,Primitive 2D BK,Primitive 2D \

BL,Primitive 2D BM,Primitive 2D BN,Primitive 2D BO,Primitive 2D \

BP,Primitive 2D BQ,Primitive 2D BR,Primitive 2D BS,Primitive 2D \

BT,Primitive 2D BU,Primitive 2D BV,Primitive 2D BW,Primitive 2D \

BX,Primitive 2D BY,Primitive 2D BZ,Primitive 2D CA,Primitive 2D \

CB,Primitive 2D CC,Primitive 2D CD,Primitive 2D CE,Primitive 2D \

CF,Primitive 2D CG,Primitive 2D CH,Primitive 2D CI,Primitive 2D \

CJ,Primitive 2D CK,Primitive 2D CL,Primitive 2D CM,Primitive 2D \

CN,Primitive 2D CO,Primitive 2D CP,Primitive 2D CQ

BOUNDARY CONDITIONS:

MASS AND MOMENTUM:

  Option = No Slip Wall

END

WALL CONTACT MODEL:

  Option = Use Volume Fraction

END

FLUID PAIR: Brine | scCO$_2$

  BOUNDARY CONDITIONS:

    WALL ADHESION:

    Option = Adhesive

    Wall Contact Angle = 5 [degree]

  END

BOUNDARY: inlet

Boundary Type = INLET

Location = BOTTOM

BOUNDARY CONDITIONS:

FLOW REGIME:

  Option = Subsonic

END

MASS AND MOMENTUM:

  Normal Speed = 0.035 [m s^-1]

  Option = Normal Speed

END

FLUID: Brine

 BOUNDARY CONDITIONS:

  VOLUME FRACTION:

   Option = Value

   Volume Fraction = 0

  END

FLUID: scCO$_2$

 BOUNDARY CONDITIONS:

  VOLUME FRACTION:

   Option = Value

   Volume Fraction = 1

  END

BOUNDARY: outlet

Boundary Type = OPENING

Location = TOP

BOUNDARY CONDITIONS:

FLOW REGIME:

Option = Subsonic

END

MASS AND MOMENTUM:

Option = Entrainment

Relative Pressure = 0 [Pa]

END

FLUID: Brine

BOUNDARY CONDITIONS:

VOLUME FRACTION:

Option = Value

Volume Fraction = 1

END

FLUID: scCO$_2$

BOUNDARY CONDITIONS:

VOLUME FRACTION:

Option = Value

Volume Fraction = 0

    END

DOMAIN MODELS:

 BUOYANCY MODEL:

  Option = Non Buoyant

 END

 DOMAIN MOTION:

  Option = Stationary

 END

 MESH DEFORMATION:

  Option = None

 END

 REFERENCE PRESSURE:

  Reference Pressure = 1 [atm]

 END

FLUID DEFINITION: Brine

 Material = Brine

 Option = Material Library

MORPHOLOGY:

  Minimum Volume Fraction = $1.0e^{-6}$

  Option = Continuous Fluid

END

FLUID DEFINITION: scCO$_2$

 Material = scCO2

 Option = Material Library

 MORPHOLOGY:

  Minimum Volume Fraction = $1e^{-o6}$

  Option = Continuous Fluid

 END

 FLUID MODELS:

 COMBUSTION MODEL:

  Option = None

 END

 HEAT TRANSFER MODEL:

  Fluid Temperature = 25 [C]

  Homogeneous Model = Off

  Option = Isothermal

 END

 THERMAL RADIATION MODEL:

  Option = None

END

TURBULENCE MODEL:

Homogeneous Model = False

Option = Laminar

END

FLUID PAIR: Brine | scCO$_2$

Surface Tension Coefficient = 0.036 [N m^-1]

INTERPHASE TRANSFER MODEL:

Option = Free Surface

END

MASS TRANSFER:

Option = None

END

MOMENTUM TRANSFER:

DRAG FORCE:

Drag Coefficient = 0.44

Option = Drag Coefficient

END

SURFACE TENSION MODEL:

Option = Continuum Surface Force

Primary Fluid = Brine

END

MULTIPHASE MODELS:

Homogeneous Model = Off

FREE SURFACE MODEL:

Interface Compression Level = 1

Option = Standard

END

INITIALISATION:

Option = Automatic

FLUID: Brine

INITIAL CONDITIONS:

Velocity Type = Cartesian

CARTESIAN VELOCITY COMPONENTS:

Option = Automatic with Value

U = 0 [m s^-1]

V = 0 [m s^-1]

W = 0 [m s^-1]

END

VOLUME FRACTION:

Option = Automatic with Value

Volume Fraction = 1

END

FLUID: scCO$_2$

INITIAL CONDITIONS:

Velocity Type = Cartesian

CARTESIAN VELOCITY COMPONENTS:

Option = Automatic with Value

U = 0 [m s^-1]

V = 0 [m s^-1]

W = 0 [m s^-1]

END

VOLUME FRACTION:

Option = Automatic with Value

Volume Fraction = 0

END

INITIAL CONDITIONS:

STATIC PRESSURE:

Option = Automatic with Value

Relative Pressure = 0 [Pa]

END

OUTPUT CONTROL:

MONITOR OBJECTS:

MONITOR BALANCES:

Option = Full

END

MONITOR FORCES:

  Option = Full

END

MONITOR PARTICLES:

  Option = Full

END

MONITOR POINT: Inlet Pressure

  Cartesian Coordinates = 0.000906091 [m], 0 [m], 0.000817603 [m]

  Coord Frame = Coord 0

  Option = Cartesian Coordinates

  Output Variables List = Pressure

  MONITOR LOCATION CONTROL:

    Interpolation Type = Nearest Vertex

  END

  POSITION UPDATE FREQUENCY:

    Option = Initial Mesh Only

MONITOR POINT: outlet Br velocity

  Cartesian Coordinates = 0.00103118 [m], 0.00173458 [m], 0.00107962 [m]

  Coord Frame = Coord 0

  Option = Cartesian Coordinates

  Output Variables List = Brine.Velocity

MONITOR LOCATION CONTROL:

Interpolation Type = Nearest Vertex

END

POSITION UPDATE FREQUENCY:

Option = Initial Mesh Only

END

MONITOR POINT: outlet scCO$_2$ velocity

Cartesian Coordinates = 0.00103118 [m], 0.00173458 [m], 0.00107962 [m]

Coord Frame = Coord 0

Option = Cartesian Coordinates

Output Variables List = scCO$_2$.Velocity

MONITOR LOCATION CONTROL:

Interpolation Type = Nearest Vertex

END

POSITION UPDATE FREQUENCY:

Option = Initial Mesh Only

END

MONITOR RESIDUALS:

Option = Full

END

MONITOR TOTALS:

Option = Full

END

RESULTS:

File Compression Level = Default

Option = Standard

END

TRANSIENT RESULTS: Transient Results 1

File Compression Level = Default

Option = Standard

OUTPUT FREQUENCY:

Option = Time Interval

Time Interval = 0.25 [s]

SOLVER CONTROL:

ADVECTION SCHEME:

Option = High Resolution

END

CONVERGENCE CONTROL:

Maximum Number of Coefficient Loops = 3

Minimum Number of Coefficient Loops = 1

Timescale Control = Coefficient Loops

END

CONVERGENCE CRITERIA:

Residual Target = 0.000001

Residual Type = MAX

END

TRANSIENT SCHEME:

Option = Second Order Backward Euler

TIMESTEP INITIALISATION:

Option = Automatic

END

COMMAND FILE:

Results Version = 18.1

Version = 18.1

END

SIMULATION CONTROL:

EXECUTION CONTROL:

EXECUTABLE SELECTION:

Double Precision = No

Large Problem = No

END

INTERPOLATOR STEP CONTROL:

Runtime Priority = Standard

MEMORY CONTROL:

Memory Allocation Factor = 1.0

END

PARALLEL HOST LIBRARY:

HOST DEFINITION: civec6fxgd2s

Remote Host Name = C-IVEC-6FXGD2S

Host Architecture String = winnt-amd64

Installation Root = C:\Program Files\ANSYS Inc\v%v\CFX

END

PARTITIONER STEP CONTROL:

Multidomain Option = Automatic

Runtime Priority = Standard

MEMORY CONTROL:

Memory Allocation Factor = 1.0

END

PARTITION SMOOTHING:

Maximum Partition Smoothing Sweeps = 100

Option = Smooth

END

PARTITIONING TYPE:

MeTiS Type = k-way

Option = MeTiS

Partition Size Rule = Automatic

END

RUN DEFINITION:

Run Mode = Full

Solver Input File = C:\Users\17973050\Documents\Thesis appendix\thesis \

appendix set 2.def

Solver Results File = G:\farjana\thesis appendix set 2_001.res

END

SOLVER STEP CONTROL:

Runtime Priority = Standard

MEMORY CONTROL:

Memory Allocation Factor = 1.0

END

PARALLEL ENVIRONMENT:

Number of Processes = 1

Start Method = Serial

END

Appendix C

To determine normalized trapped supercritical CO_2 (Sot*) saturation as presented in Table 6.3 and Figure 6.3, the correlations proposed by Standing (1975) are used, as given by Equations C1 and C2:

$$S_{o,F}^* = 0.5 \left[(S_o^* - S_{or}^*) + \sqrt{\left\{ (S_o^* - S_{or}^*)^2 + \frac{4}{C} (S_o^* - S_{or}^*) \right\}} \right] \tag{C1}$$

$$S_{ot}^* = S_0^* - S_{o,F}^* \tag{C2}$$

The correlation for Land's trapping coefficient, C, as given by Equation C3:

$$C = \frac{1}{S_{or}^*} - \frac{1}{S_{oi}^*} \tag{C3}$$

Where,

$S_{o,F}^*$ = Normalized scCO$_2$ free saturation at various simulation times;

S_{ot}^* = Normalized trapped scCO$_2$ saturation at various simulation times;

S_{or}^* = Normalized scCO$_2$ residual saturation = $\frac{S_{or}}{1\text{-}S_{wc}}$;

S_{or}^* = Normalized scCO$_2$ initial saturation = $\frac{S_{oi}}{1\text{-}S_{wc}}$;

S_o^* = normalized scCO$_2$ saturation at various simulation times; and

C = Land trapping coefficient.

The values of normalized scCO$_2$ residual saturation, S_{or}^*, and the normalized scCO$_2$ saturation at various simulation times, S_o^* in Equation C1 and the normalized scCO$_2$ free saturation at various simulation times, $S_{o,F}^*$ were determined from the numerical simulation results for drainage and imbibition processes when the system reached a steady state (when the pressure drop appeared to be constant). The corresponding initial and residual fluid saturations (S_{wi}, S_{oi} and S_{or}) are then directly obtained from the simulation.

The various saturations as described above, obtained from the numerical simulation of the sample, are provided below in Table C.

Table C: Various saturation values obtained from simulation

Saturation	Value obtained from simulation
Connate brine saturation, S_{wc}	0.13
Maximum residual scCO$_2$ saturation, $S_{or,max}$	0.81
Initial brine saturation, S_{wi}	0.21
Initial scCO$_2$ saturation, S_{oi}	0.79
scCO$_2$ residual saturation, S_{or}	0.13

The process of calculating normalized trapped scCO$_2$ saturation (Sot*) is provided below through a sample calculation of an imbibition process with a contact angle θ = 110° and simulation time of 30 s to demonstrate how the results presented in Table 6.3 were obtained.

Sample calculation for Land's trapping coefficient, C

Based on the data as obtained from the simulation (Table C):

$$S_{or}^* = \frac{S_{or}}{1\text{-}S_{wc}} = \frac{0.13}{1-0.13} = 0.15$$

$$S_{oi}^* = \frac{S_{oi}}{1\text{-}S_{wc}} = \frac{0.79}{1\text{-}0.13} = 0.91$$

Therefore, from Equation C3, $C = \frac{1}{0.15} - \frac{1}{0.91} = 5.57$

Sample calculation for normalized trapped scCO$_2$ saturation, S$_{ot}$

For imbibition processes with a contact angle θ = 110° and simulation time = 30 s, the scCO$_2$ saturation, S$_o$, obtained from simulation, is 0.14 (Table 6.3), which yields the normalized scCO$_2$ saturation: $S_o^* = \frac{S_o}{1\text{-}S_o} = 0.16$.

Inserting S$_o$* = 0.16 and S$_{or}$* = 0.15 (as determined earlier) in Equation C1 yields, S$_{o,F}$* = 0.048.

Therefore, from Equation C2, S$_{ot}$* = S$_o$* - S$_{o,F}$* = 0.112.

Appendix D

Supercritical CO_2 ($scCO_2$) and brine movement in the *XY* plane within the pore spaces of Ottawa F42 Sand Pack for set 2 (drainage, $scCO_2$ velocity = 0.035 m/s at $\theta = 5°$; and for imbibition, brine velocity = 0.035 m/s at $\theta = 30°$) are presented in this Appendix.
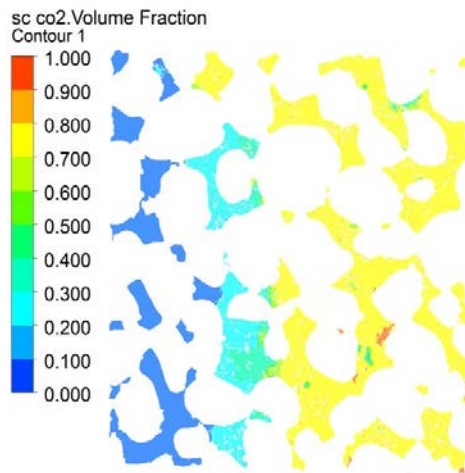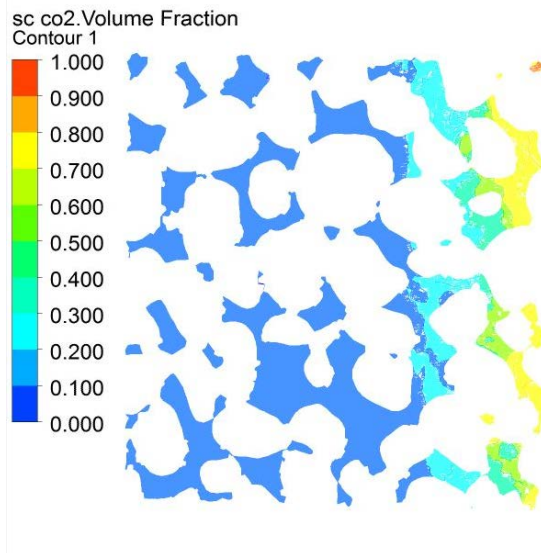
For drainage processes:
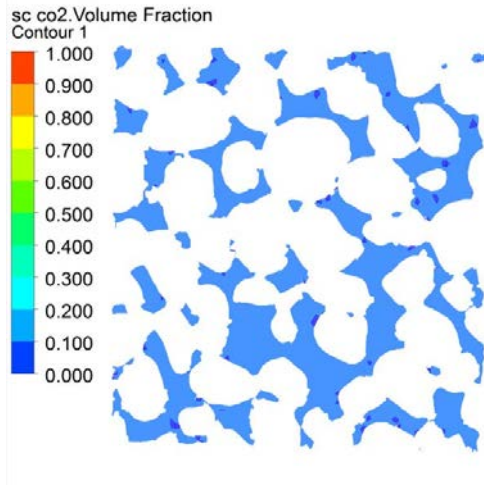
Figure D.1: Plane view at time step 0[s].
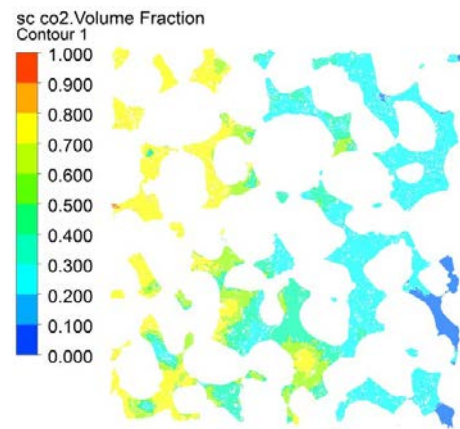
Figure D.2: Plane view at time step 5[s].
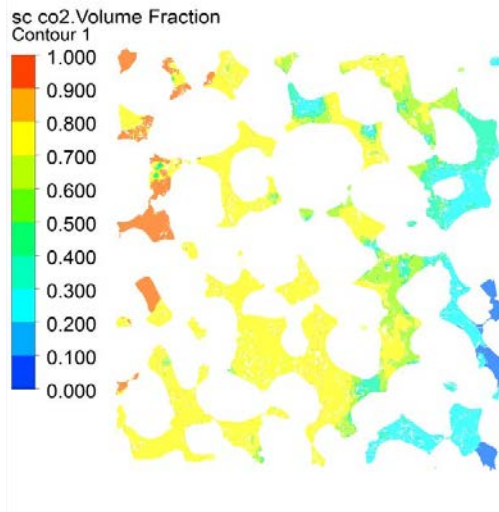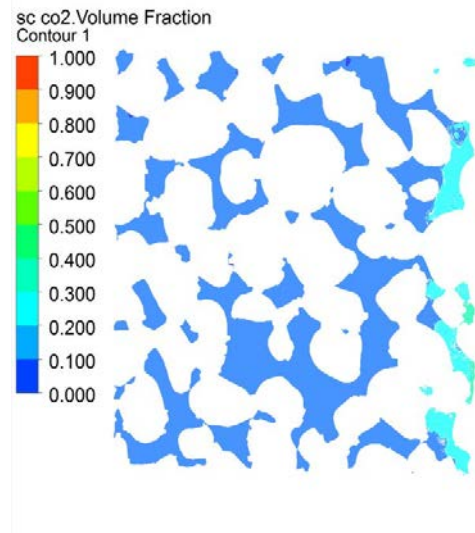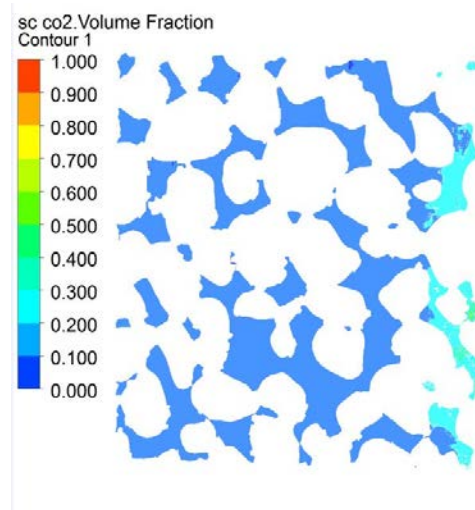

Figure D.3: Plane view at time step 10[s].
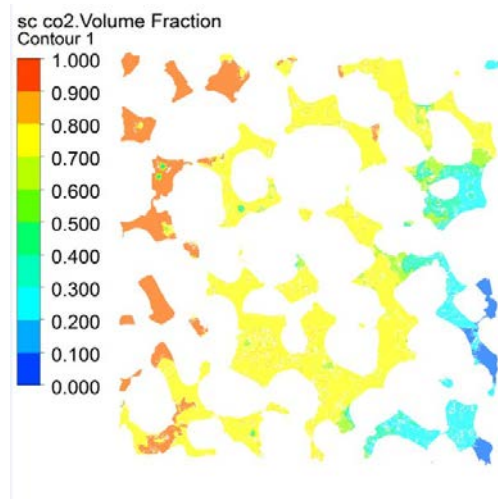
Figure D.4: Plane view at time step 15[s].
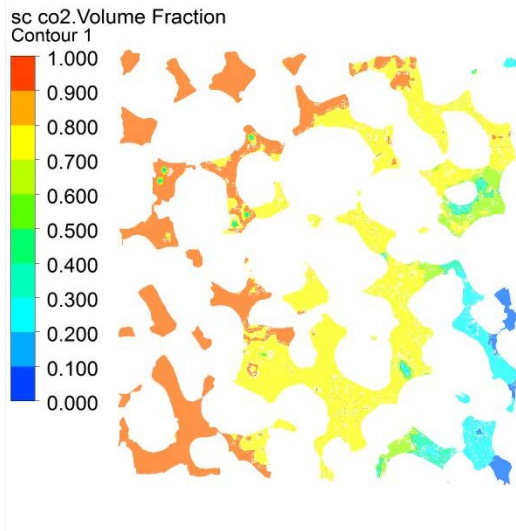
Figure D.5: Plane view at time step 20[s].
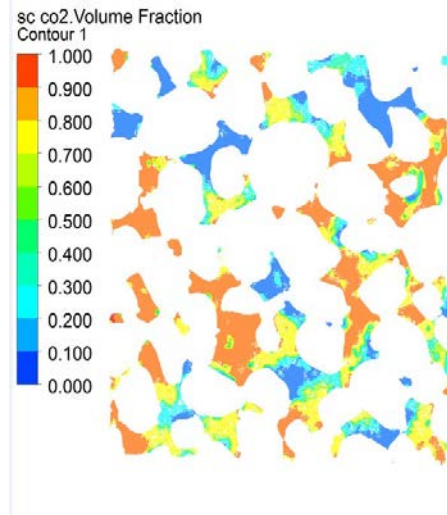
Figure D.6: Plane view at time step 25[s].

For imbibition processes:
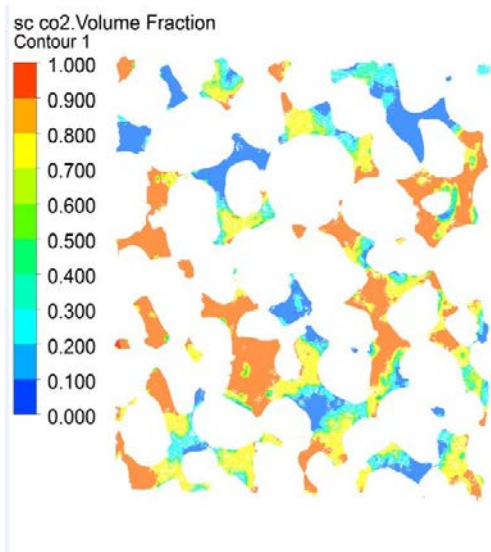
Figure D.7: Plane view at time step 0[s].

Figure D.8: Plane view at time step 5[s].

Figure D.9: Plane view at time step 10[s].

Figure D.10: Plane view at time step 15[s].
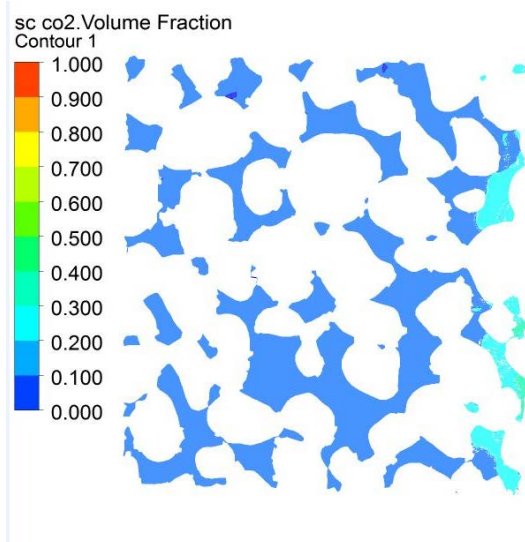
Figure D.11: Plane view at time step 20[s].

Figure D.12: Plane view at time step 25[s].

Appendix E – Copy right

Society of Petroleum Engineers

Calgary • Dallas • Dubai • Houston • Kuala Lumpur • London • Moscow
www.spe.org

November 5, 2018

Dear Farjana.

Please use this email as proof of permission to reuse SPE-182240-MS, SPE-185744- MS and SPE-192105-MS in your thesis. Please follow the terms and conditions of the attached license.

Sincerely,

Barbara Barnett
Retail Sales Coordinator
Society of Petroleum Engineers (SPE)
PO Box 833836
Richardson, TX 75083-3836
Phone: 972-952-1107
Fax: 972-952-9435
Email: bbarnett@spe.org
Website: www.spe.org

Americas Office
222 Palisades Creek Drive • Richardson, Texas 75080-2040 USA • Tel: +1.972.952.9393 • Fax: +1.972.952.9435 • Email: spedal@spe.org

180

STANDARD TERMS AND CONDITIONS FOR REPRODUCTION OF MATERIAL

1. The Society of Petroleum Engineers, Inc. ("SPE") holds the copyright for this material. By clicking "accept" in connection with completing this licensing transaction, you agree that the following terms and conditions apply to this transaction (along with the Billing and Payment terms and conditions established by Copyright Clearance Center, Inc. ("CCC"), at the time that you opened your RightsLink account and that are available at any time at).

2. SPE hereby grants to you a non-exclusive license to use this material. Licenses are for one-time use only with a maximum distribution equal to the number that you identified in the licensing process; any form of republication must be completed within six months from the date hereof (although copies prepared before then may be distributed thereafter); and any electronic posting is limited to the period identified in the licensing process.

3. You may not alter or modify the material in any manner (except that you may use, within the scope of the license granted, one or more excerpts from the copyrighted material, provided that the process of excerpting does not alter the meaning of the material or in any way reflect negatively on SPE or any writer of the material or their employer), nor may you translate the material into another language.

4. Total excerpts from the license material may not exceed thirty percent (30%) of the total text. Not more than five (5) excerpts, figures, tables, or images may be used from any given paper. Multiple permission requests may not be used to exceed these limits.

5. SPE reserves all rights not specifically granted in the combination of (i) the license details provided by you and accepted in the course of this licensing transaction, (ii) these terms and conditions and (iii) CCC's Billing and Payment terms and conditions.

6. While you may exercise the rights licensed immediately upon issuance of the license at the end of the licensing process for the transaction, provided that you have disclosed complete and accurate details of your proposed use, no license is finally effective unless and until full payment is received from you (either by SPE or by CCC) as provided in CCC's Billing and Payment terms and conditions. If full payment is not received on a timely basis, then any license preliminarily granted shall be deemed automatically revoked and shall be void as if never granted. Further, in the event that you breach any of these terms and conditions or any of CCC's Billing and Payment terms and conditions, the license is automatically revoked and shall be void as if never granted. Use of materials as described in a revoked license, as well as any use of the materials beyond the scope of an unrevoked license, may constitute copyright infringement and SPE reserves the right to take any and all action to protect its copyright in the materials

7. You must include the appropriate copyright and permission notice and disclaimer in connection with any reproduction of the licensed material. The copyright information is found on the front page of the paper immediately under the title and author. This statement will then be followed with the disclaimer, "Further reproduction prohibited without permission." Examples:1) Copyright 1990, Society of Petroleum

Engineers Inc. Copyright 1990, SPE. Reproduced with permission of SPE. Further reproduction prohibited without permission.2) Copyright 2010, IADC/SPE Drilling Conference and Exhibition Copyright 2010, IADC/SPE Drilling Conference and Exhibition. Reproduced with permission of SPE. Further reproduction prohibited without permission.3) Copyright 2008, Offshore Technology Conference Copyright 2008, Offshore Technology Conference. Reproduced with permission of OTC. Further reproduction prohibited without permission.4) Copyright 2005, International Petroleum Technology Conference Copyright 2005, International Petroleum Technology Conference. Reproduced with permission of IPTC. Further reproduction prohibited without permission. If for any reason, the copyright on the paper is missing or unclear, please follow Example 1 above, using SPE as the default copyright holder. SPE administers copyright for OTC, IPTC and other joint events on behalf of all parties in those events.

8. SPE makes no representations or warranties with respect to the licensed material and adopts on its own behalf the limitations and disclaimers established by CCC on its behalf in its Billing and Payment terms and conditions for this licensing transaction.

9. You hereby indemnify and agree to hold harmless SPE and CCC, and their respective officers, directors, employees and agents, from and against any and all claims arising out of your use of the licensed material other than as specifically authorized pursuant to this license.

10. This license is personal to you, but may be assigned or transferred by you to a business associate (or to your employer) if you give prompt written notice of the assignment or transfer to SPE. No such assignment or transfer shall relieve you of the obligation to pay the designated license fee on a timely basis (although payment by the identified assignee can fulfill your obligation).

11. This license may not be amended except in a writing signed by both parties (or, in the case of SPE, by CCC on SPE's behalf).

12. SPE hereby objects to any terms contained in any purchase order, acknowledgment, check endorsement or other writing prepared by you, which terms are inconsistent with these terms and conditions or CCC's Billing and Payment terms and conditions. These terms and conditions, together with CCC's Billing and Payment terms and conditions (which are incorporated herein), comprise the entire agreement between you and SPE (and CCC) concerning this licensing transaction. In the event of any conflict between your obligations established by these terms and conditions and those established by CCC's Billing and Payment terms and conditions, these terms and conditions shall control.

13. This Agreement shall be governed and interpreted by the laws of the State of Texas, United States of America. Regardless of the place of performance or otherwise, the Agreement, and all schedules, amendments, modifications, alterations, or supplements thereto, will be governed by the laws of the State of Texas, United States of America. If any provisions of the Agreement are unenforceable under applicable law, the remaining provisions shall continue in full force and effect.

Other Terms and Conditions: None

Appendix F

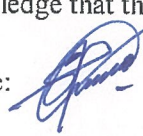**Attribution of Authorship of papers are attached.**

Attribution of Authorship:

Paper 1 (SPE-182240-MS): **"Numerical Modeling for the Prediction of Residual CO₂ Trapping in Water-Wet Geological Porous Media"**. SPE Asia Pacific Oil & Gas Conference and Exhibition, 25-27 October 2016 in Perth, Australia.

Authors and full affiliations: Farjana Jahan [a], Shakil Ahmed [b], Mofazzal Hossain [a], Stefan Iglauer, [a].

[a] Curtin University, Department of Petroleum Engineering, 26 Dick Perry Avenue Technology Park, Kensington WA-6151, Perth, Australia.
[b] CSIRO Energy Business Unit, 26 Dick Perry Avenue Technology Park, Kensington WA-6151, Perth, Australia.
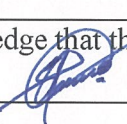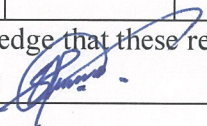
	Conception and design	Acquisition of data method	Data conditioning and manipulation	Analysis and statistical method	Interpretation and discussion	Final approval
Dr. Shakil Ahmed	X			X	X	X
I acknowledge that these represent to the contribution to the above research output. Signature: '11/12/2018						
Dr. Mofazzal Hossain	X			X	X	X
I acknowledge that these represent to the contribution to the above research output. Signature: 11/12/2018						
Dr Stefan Iglauer						X
I acknowledge that these represent to the contribution to the above research output. Signature:						

Paper 2 (SPE-185744-MS): **"Investigating Impact of Various Properties on Relative Permeability and Non-Wetting Phase Fractional Flow in Brine/Oil system in Water-Wet Reservoir Rock by Numerical Simulation".** SPE WRM, 23-27 April 2017, Bakersfield, California, USA.

Authors and full affiliations: Farjana Jahan [a], Mofazzal Hossain [a], Shakil Ahmed [b], Stefan Iglauer, [a].

[a] Curtin University, Department of Petroleum Engineering, 26 Dick Perry Avenue Technology Park, Kensington WA-6151, Perth, Australia.
[b] CSIRO Energy Business Unit, 26 Dick Perry Avenue Technology Park, Kensington WA-6151, Perth, Australia.
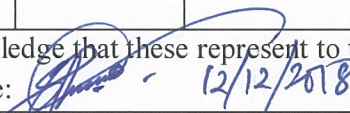
	Conception and design	Acquisition of data method	Data conditioning and manipulation	Analysis and statistical method	Interpretation and discussion	Final approval
Dr. Mofazzal Hossain	X			X	X	X
I acknowledge that these represent to the contribution to the above research output. Signature: _~SHBoo~ 12/12/2018_						
Dr. Shakil Ahmed	X			X	X	X
I acknowledge that these represent to the contribution to the above research output. Signature: _(signature) 12/12/2018_						
Dr Stefan Iglauer						X
I acknowledge that these represent to the contribution to the above research output. Signature:						

Paper 3: **"Application of Digital Rock Physics on Enhanced Oil Recovery (EOR) For Berea Sandstone in Brine/Oil System by Numerical Simulation".** Proceedings of One Curtin International Postgraduate Conference (OCPC), December 10 – 12, 2017, Miri, Sarawak, Malaysia.

Authors and full affiliations: Farjana Jahan [a], Mofazzal Hossain [a], Shakil Ahmed [b].

[a] Curtin University, Department of Petroleum Engineering, 26 Dick Perry Avenue Technology Park, Kensington WA-6151, Perth, Australia.
[b] CSIRO Energy Business Unit, 26 Dick Perry Avenue Technology Park, Kensington WA-6151, Perth, Australia.

	Conception and design	Acquisition of data method	Data conditioning and manipulation	Analysis and statistical method	Interpretation and discussion	Final approval
Dr. Mofazzal Hossain	X			X	X	X
I acknowledge that these represent to the contribution to the above research output. Signature: _____ 12/12/2018						
Dr. Shakil Ahmed	X			X	X	X
I acknowledge that these represent to the contribution to the above research output. Signature: _____ 12/12/2018						

Paper 4 (SPE-192105-MS): **"Investigating the Influence of wettability and direction on Supercritical CO_2 trapping for Supercritical CO_2-Brine imbibition process at pore scale for Bentheimer Sandstone."** SPE Asia Pacific Oil & Gas Conference and Exhibition (APOGCE), 23 – 25 October 2018, Brisbane, Australia.

Authors and full affiliations: Farjana Jahan [a], Shakil Ahmed [b] , Mofazzal Hossain [a].

[a] Curtin University, Department of Petroleum Engineering, 26 Dick Perry Avenue Technology Park, Kensington WA-6151, Perth, Australia.
[b] CSIRO Energy Business Unit, 26 Dick Perry Avenue Technology Park, Kensington WA-6151, Perth, Australia.

	Conception and design	Acquisition of data method	Data conditioning and manipulation	Analysis and statistical method	Interpretation and discussion	Final approval
Dr. Shakil Ahmed	X			X	X	X
I acknowledge that these represent to the contribution to the above research output. Signature: *12/12/2018*						
Dr. Mofazzal Hossain	X			X	X	X
I acknowledge that these represent to the contribution to the above research output. Signature:						

Hi Mofazzal,

I approve it, I can only send you the form on Thursday though.

Best Regards,
Stefan

-----Original Message-----
From: Mofazzal Hossain [mailto:md.hossain@curtin.edu.au]
Sent: Tuesday, 11 December 2018 3:25 PM
To: Stefan IGLAUER <s.iglauer@ecu.edu.au>
Subject: RE: Scanned Document

Dear Stefan,

Hope you are doing fine. Would you please kindly sign the attribution of authorship for 2nd paper as attached and send back to me.

Farjana will be submitting tomorrow. She needs this paper. I would appreciate if you can please consider this as an urgent matter.

Many thanks in advance for your support and cooperation.

Kind regards

Mofazzal

-----Original Message-----
From: Stefan IGLAUER <s.iglauer@ecu.edu.au>
Sent: Thursday, 18 October 2018 5:01 PM
To: Mofazzal Hossain <md.hossain@curtin.edu.au>
Subject: FW: Scanned Document

Hi Mofazzal,

Good to hear from you, hope you are doing very well.

Please find the signed form attached.

Best Regards,
Stefan

-----Original Message-----
From: siglauer [mailto:s.iglauer@ecu.edu.au]
Sent: Thursday, 18 October 2018 4:55 PM
To: Stefan IGLAUER <s.iglauer@ecu.edu.au>
Subject: Scanned Document

Sent by: siglauer [s.iglauer@ecu.edu.au] Number of Images: 1 Attachment File Type: PDF

Device Name: PRN194514
Device Location: